



저작자표시-비영리-변경금지 2.0 대한민국

이용자는 아래의 조건을 따르는 경우에 한하여 자유롭게

- 이 저작물을 복제, 배포, 전송, 전시, 공연 및 방송할 수 있습니다.

다음과 같은 조건을 따라야 합니다:



저작자표시. 귀하는 원저작자를 표시하여야 합니다.



비영리. 귀하는 이 저작물을 영리 목적으로 이용할 수 없습니다.



변경금지. 귀하는 이 저작물을 개작, 변형 또는 가공할 수 없습니다.

- 귀하는, 이 저작물의 재이용이나 배포의 경우, 이 저작물에 적용된 이용허락조건을 명확하게 나타내어야 합니다.
- 저작권자로부터 별도의 허가를 받으면 이러한 조건들은 적용되지 않습니다.

저작권법에 따른 이용자의 권리는 위의 내용에 의하여 영향을 받지 않습니다.

이것은 [이용허락규약\(Legal Code\)](#)을 이해하기 쉽게 요약한 것입니다.

[Disclaimer](#)

Ph.D's Thesis

Direct Numerical Simulations of Ignition  
Effects on Low Temperature Combustion  
(LTC) Systems

Seungook Kim

Department of Mechanical Engineering

Graduate School of UNIST

2019

Direct Numerical Simulations of Ignition  
Effects on Low Temperature Combustion  
(LTC) Systems

Seungook Kim

Department of Mechanical Engineering

Graduate School of UNIST

# Direct Numerical Simulations of Ignition Effects on Low Temperature Combustion (LTC) systems

A thesis/dissertation  
submitted to the Graduate School of UNIST  
in partial fulfillment of the  
requirements for the degree of  
Doctor of Philosophy of Science

Seung Ook Kim

05. 21. 2019  
Approved by



Advisor  
Chun Sang Yoo



# Direct Numerical Simulations of Ignition Effects on Low Temperature Combustion (LTC) systems

Seung Ook Kim

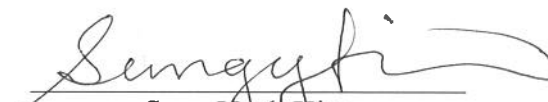
This certifies that the thesis/dissertation of Seung Ook Kim is  
approved.

05. 21. 2019



---

Advisor: Chun Sang Yoo



---

Sung Yeub Kim



---

Taesung Kim



---

Jaesung Jang



---

Pilwon Kim

## Abstract

In this thesis, several low temperature combustion (LTC) simulations were performed with various combustion system configurations. First, two-dimensional direct numerical simulations (DNSs) of ignition of lean primary reference fuel (PRF)/air mixtures at high pressure and intermediate temperature near the negative temperature coefficient (NTC) regime were performed with a 116 species-reduced mechanism to elucidate the effects of fuel composition, thermal stratification, and turbulence on PRF homogeneous charge compression-ignition (HCCI) combustion. Second, the characteristics of autoignited laminar lifted methane/hydrogen jet flames in heated coflow air are numerically investigated with a 57-species detailed methane/air chemical kinetic mechanism. The autoignited laminar lifted jet flames can be categorized into three regimes of combustion mode: the tribrachial edge flame regime, the Moderate or Intense Low-oxygen Dilution (MILD) combustion regime, and the transition regime in between. In certain condition, an unusual decreasing liftoff height behavior with increasing  $U_0$  is observed. Additional simulations with modified hydrogen mass diffusivity were performed to deeply understand unusual decreasing liftoff height behaviors. Third, similar to methane/hydrogen jet flame, *n*-heptane diluted with  $N_2$  lifted laminar lifted jet flames are simulated with the 68-species skeletal mechanism. Near autoignition condition, *n*-heptane laminar lifted flame exhibits a stiff increase in its liftoff height at a certain  $U_0$ . Schmidt number analysis is used to elucidate this abnormal phenomenon. At the end of the thesis, turbulent lifted hydrogen jet flames with different coflow temperatures (i.e.  $T_c = 750, 850, \text{ and } 950 \text{ K}$ ) near the autoignition limit of hydrogen/air mixture are investigated using 3-D DNSs with a detailed hydrogen/air chemical mechanism. The DNSs are performed at a jet Reynolds number of 8,000 with over 1.28 billion grid points. Overall combustion characteristics and stabilization mechanisms of lifted flames were studied with comparing previous high-temperature coflow. Several physical parameters and chemical explosive mode analysis (CEMA) used to identify the fundamentals of LTC in various combustion system configurations.



# Contents

<b>I</b>	<b>Introduction</b>	<b>1</b>
1.1	Clean Combustion . . . . .	1
1.2	Combustion of HCCI Engine . . . . .	2
1.3	Combustion of Lifted Flames . . . . .	3
1.3.1	MILD Combustion . . . . .	4
1.4	Objectives . . . . .	6
<b>II</b>	<b>Homogeneous Charge Compression-Ignition with PRF fuel</b>	<b>8</b>
2.1	Introduction . . . . .	8
2.2	Numerical Methods and Initial Conditions . . . . .	11
2.3	Effect of Fuel Composition and Temperature . . . . .	14
2.3.1	Overall Ignition Characteristics . . . . .	14
2.3.2	Chemical Explosive Mode Analysis . . . . .	19
2.4	Effect of Turbulence . . . . .	21
2.4.1	Ignition Damköhler Number . . . . .	23
2.5	Discussion . . . . .	26

2.6	Conclusions . . . . .	28
-----	-----------------------	----

### **III Autoignited Laminar Lifted Methane/Hydrogen Jet Flames in Heated**

	<b>Coflow Air</b>	<b>29</b>
--	-------------------	-----------

3.1	Introduction . . . . .	29
-----	------------------------	----

3.2	Numerical Methods . . . . .	32
-----	-----------------------------	----

3.3	Overall Characteristics of The Lifted Flames . . . . .	34
-----	--	----

3.4	Chemical Kinetic Mechanisms . . . . .	36
-----	---------------------------------------	----

3.5	Lifted Jet Flames under HTLH Condition . . . . .	39
-----	--	----

3.6	Lifted Jet Flames under LTHH Condition . . . . .	41
-----	--	----

3.7	Effect of Hydrogen on The Liftoff Characteristics . . . . .	46
-----	---	----

3.8	Effect of Hydrogen Mass Diffusivity on $H_L$ . . . . .	46
-----	--	----

3.9	Effect of Hydrogen on The Lifted Flame Stabilization . . . . .	51
-----	--	----

3.10	Ignition Characteristics: CEMA . . . . .	58
------	--	----

3.11	Conclusions . . . . .	64
------	-----------------------	----

### **IV Autoignited Laminar Lifted *n*-Heptane Jet Flames in Heated Coflow**

	<b>Air</b>	<b>66</b>
--	------------	-----------

4.1	Introduction . . . . .	66
-----	------------------------	----

4.2	Numerical Methods . . . . .	67
-----	-----------------------------	----

4.3	Lifted Jet Flame Combustion Characteristics . . . . .	69
-----	---	----

4.4	Effect of Schmidt Number on the Liftoff Characteristics . . . . .	71
4.5	Stabilization Mechanisms . . . . .	72
4.6	Liftoff Height Jump . . . . .	75
4.7	Conclusions . . . . .	80
<b>V</b>	<b>Turbulent Lifted Hydrogen Jet Flames in Heated Coflow Air</b>	<b>82</b>
5.1	Introduction . . . . .	82
5.2	Numerical Method and Initial Conditions . . . . .	84
5.3	Flame Structure and Dynamics . . . . .	85
5.3.1	Chemical Explosive Mode Analysis . . . . .	89
5.4	Conclusions . . . . .	97
<b>VI</b>	<b>Conclusion</b>	<b>100</b>
6.1	Future Work . . . . .	102
	References . . . . .	104
	Acknowledgements . . . . .	119

## List of Figures

1.1	Schematic of spark ignition (SI) gasoline, compression ignition (CI) diesel, and homogeneous charge compression ignition (HCCI) engine combustion concepts, adapted from [1]. . . . .	3
1.2	Autoignited methane/hydrogen lifted flames at various jet velocities for (Initial temperature, hydrogen ratio, initial fuel mole fraction) = (900 K, 0.14, 0.20) (a), and (860 K, 0.30, 0.20) (b)., adopted from [2] . . . . .	5
2.1	0-D ignition delays as a function of initial temperature for different PRF/air mixtures at $p_0 = 40$ atm and of $\phi_0 = 0.4$ . . . . .	10
2.2	Initial temperature (top) and vorticity (bottom) fields of Case 2. . . . .	12
2.3	Temporal evolutions of the mean pressure and mean HRR (left) and the PRR (right) for Cases 1–3 (PRF50; a & c) and Cases 4–6 (PRF80; b & d). . . . .	15
2.4	Temporal evolutions of the mean mass fractions of important species and mean HRR for (a) 0-D case of PRF50/air mixture, (b) Case 1, (c) Case 3, (d) 0-D case of PRF80/air mixture, (e) Case 4, and (f) Case 6. . . . .	17
2.5	Isocontours of the normalized heat release rate for Cases 1–3 (from left to right) at $t/\tau_{ig}^0 = 1.0, 0.94,$ and $0.61,$ respectively. . . . .	18

2.6	Isocontours of (a) the timescale of the chemical explosive mode, (b) $Da_c$ , (c) temperature, and (d) $\chi$ for Case 1 (top) at $t/\tau_{ig}^0 = 1.0$ and Case 3 (bottom) at $t/\tau_{ig}^0 = 0.61$ . The solid line denotes the reaction front ( $Da_c = 1$ ). . . . .	20
2.7	Temporal evolutions of the mean pressure and mean HRR for (a) PRF50 and (b) PRF80. . . . .	22
2.8	Isocontours of the normalized heat release rate for Cases 3 (top) and 8 (bottom). From left to right, $t/\tau_{ig}^0 = 0.36$ and $0.52$ , respectively. . . . .	23
2.9	Temporal evolution of the mean front speed, $\overline{S_d^*}$ , for (a) Cases 2, 3, 7, and 8 (PRF50) and (b) Cases 5, 6, 9, and 10 (PRF80). . . . .	25
2.10	The locations of the cases with small $u'$ (Cases 3 and 6) and large $u'$ (Cases 8 and 10) in the regime diagram for turbulent premixed combustion. . . . .	26
3.1	Schematic of the computational domain for simulations of autoignited laminar lifted methane/hydrogen jet flames in heated coflow air. . . . .	33
3.2	Profiles of (a) axial velocity, (b) temperature, and mass fractions of (c) $\text{CH}_2\text{O}$ and (d) $\text{OH}$ of a lifted methane/hydrogen jet flame along the stoichiometric mixture fraction, $\xi_{\text{st}}$ , isoline for three different grid resolutions. The inlet temperature and velocity of the fuel jet are 940 K and 15 m/s, respectively, and the hydrogen volume fraction of the fuel jet is 0.35. . . . .	35
3.3	Variations of (a) laminar burning velocity, $S_L$ , and (b) 0-D ignition delay, $\tau_{\text{ig}}^0$ , of a stoichiometric methane/hydrogen/air mixture with $X_{\text{F},0} = 0.2$ and $R_{\text{H}} = 0.35$ as a function of the inlet or initial temperature for several different chemical kinetic mechanisms including GRI-3.0 [3], San Diego [4], USC-II [5], Galway [6], and Konnov [7] mechanisms. . . . .	37



3.4	Variation of the liftoff height, $H_L$ , of autoignited laminar lifted methane/hydrogen jet flames with $X_{F,0} = 0.2$ and $R_H = 0.35$ as a function of the inlet velocity, $U_0$ , for several different chemical kinetic mechanisms and $T_0$ . . . . .	38
3.5	Isocontours of (a) $Y_{OH}$ (left half) and $T$ (right half) and (b) $Y_{H_2O_2}$ (left half) and $Y_{CH_2O}$ (right half) for autoignited laminar lifted methane/hydrogen jet flames for various fuel jet velocities $U_0$ under the HTLH condition ( $T_0 = 1100$ K and $R_H = 0.05$ ). The dashed and dash-dotted lines in (a) represent the mixture fraction isoline passing through the flamebase, $\xi_{fb}$ , and the stoichiometric mixture fraction isoline, $\xi_{st}(= 0.325)$ , respectively. . . . .	40
3.6	Variations of $H_L$ (red) and $(T_{max} - T_0)/T_{ig}$ (blue) as a function of $U_0$ for autoignited laminar lifted methane/hydrogen jet flames under the HTLH condition ( $T_0 = 1100$ K and $R_H = 0.05$ ). The black dash-dotted line represents $H_L$ variation of the corresponding experiments [2]. . . . .	42
3.7	Isocontours of (a) $Y_{OH}$ (left half) and $T$ (right half) and (b) $Y_{H_2O_2}$ (left half) and $Y_{CH_2O}$ (right half) for autoignited laminar lifted methane/hydrogen jet flames for various fuel jet velocities $U_0$ under the LTHH condition ( $T_0 = 940$ K and $R_H = 0.35$ ). The dashed and dash-dotted lines in (a) represent the mixture fraction isoline passing through the flamebase, $\xi_{fb}$ , and the stoichiometric mixture fraction isoline, $\xi_{st}(= 0.378)$ , respectively. . . . .	43
3.8	Variations of $H_L$ (red) and $(T_{max} - T_0)/T_{ig}$ (blue) as a function of $U_0$ for autoignited lifted flames under the LTHH condition ( $T_0 = 940$ K and $R_H = 0.35$ ). The black dash-dotted line represents $H_L$ variation of the corresponding experiments [2] . . . . .	44

3.9	Isocontour of heat release rate ( $\text{J}/\text{mm}^3\text{s}$ ) for autoignited laminar lifted methane/hydrogen jet flames with $U_0 = 4$ (left) and 15 m/s (right) under the LTHH condition. The dash-dotted line represents the stoichiometric mixture fraction isoline, $\xi_{\text{st}}$ . . . . .	45
3.10	Isocontours of (a) $Y_{\text{OH}}$ (left half) and $T$ (right half) and (b) $Y_{\text{H}_2\text{O}_2}$ (left half) and $Y_{\text{CH}_2\text{O}}$ (right half) for autoignited laminar lifted methane/hydrogen jet flames with modified $D_{\text{H}_2}$ for various fuel jet velocities $U_0$ under the LTHH condition ( $T_0 = 940$ K and $R_{\text{H}} = 0.35$ ). The dashed and dash-dotted lines in (a) represent the mixture fraction isoline passing through the flamebase, $\xi_{\text{fb}}$ , and the stoichiometric mixture fraction isoline, $\xi_{\text{st}} (= 0.378)$ , respectively. 47	47
3.11	The variation of (a) $H_{\text{L}}$ and (b) $(T_{\text{max}} - T_0)/T_{\text{ig}}$ for various fuel jet velocities with normal (solid line) and modified $H_2$ diffusivity (dashed line) under the LTHH condition ( $T_0 = 940$ K and $R_{\text{H}} = 0.35$ ). . . . .	48
3.12	The profiles of $R_{\text{H}}$ (left) and $T$ (right) along the mixture fraction isoline passing through the flamebase, $\xi_{\text{fb}}$ , for various fuel jet velocities with normal (top) and modified (bottom) $H_2$ diffusivities under the LTHH condition ( $T_0 = 940$ K and $R_{\text{H}} = 0.35$ ). . . . .	49
3.13	Schematic for the stabilization of autoignited laminar methane/hydrogen lifted flames with (a) normal and (b) modified $H_2$ diffusivity. . . . .	50
3.14	Profiles of convection (blue), diffusion in parallel (pink) and normal (red) direction, and chemical reaction (green) terms along the mixture fraction isoline passing through the flamebase, $\xi_{\text{fb}}$ , for (a) $U_0 = 4$ , (b) 10, and (c) 30 m/s. . . . .	53

3.15 Profiles of R14–15 (black) and R10 (red) with autoignition index (green) along the mixture fraction isoline passing through the flamebase, $\xi_{fb}$ , for (a) $U_0 = 4$ , (b) 10, and (c) 30 m/s. The vertical dashed lines represent the flamebase location. . . . .	54
3.16 Variation of (a) $S_L$ and (b) $S_e/S_L$ at 2, 3, 4, and 5 mm upstream of the flamebase along the mixture fraction isoline passing through the flamebase, $\xi_{fb}$ , for $U_0 = 4$ , 10, and 30 m/s cases. . . . .	57
3.17 Isocontours of EI of (a) $T$ , (b) $CH_4$ , (c) $CH_2O$ , (d) $H_2O_2$ , and (e) $H_2$ , and (f) heat release rate ( $J/mm^3s$ ) for autoignited laminar lifted methane/hydrogen jet flames with $U_0 = 4$ , 10, and 30 m/s under the LTHH condition. The dashed line represents an isoline of $Re(\lambda_e) = 0$ and the dash-dotted in (f) denotes the stoichiometric mixture fraction isoline, $\xi_{st}$ . . . . .	60
3.18 Isocontours of PI of (a) reactions of $CH_3$ conversion to $CH_2O$ and $CH_3O$ , (b) $CH_2O$ conversion to $HCO$ , (c) $H_2O_2 + M \rightarrow OH + OH + M$ (–R16), (d) $H + O_2 + M \rightarrow HO_2 + M$ (R9), (e) $H + O_2 \rightarrow O + OH$ (R1), and (f) $H_2 + OH \rightarrow H + H_2O$ (R3) for autoignited laminar lifted methane/hydrogen jet flames for cases with $U_0 = 4$ , 10, and 30 m/s. The dashed line represents an isoline of $Re(\lambda_e) = 0$ . . . . .	62
3.19 PIs of selected reactions at the sampled point, Point A. Location of Point A is specified in Fig. 3.17a . . . . .	63
4.1 Schematic of the computational domain for simulations of autoignited laminar lifted $n$ -heptane jet flames in heated coflow air. . . . .	68

4.2	Isocontours of (a) $T$ (left half) and $Y_{\text{OH}}$ (right half) and (b) $Y_{\text{CH}_2\text{O}}$ (left half) and heat release rate (HRR) (right half) for autoignited laminar lifted $n$ -heptane jet flames for various fuel jet velocities $U_0$ ( $T_0 = 1025$ K). The dashed and dash-dotted lines in (a) represent the mixture fraction isoline passing through the flamebase, $\xi_{\text{fb}}$ , and the stoichiometric mixture fraction isoline, $\xi_{\text{st}}$ ( $= 0.494$ ), respectively. . . . .	70
4.3	Experimental and simulation results of autoignited $n$ -heptane fuel liftoff height in relation to jet velocity . . . . .	71
4.4	Simplified flame shape of highly diluted $n$ -heptane laminar lifted flame in autoignition condition; red solid and black dashed lines indicate a flamebase and stoichiometric mixture fraction line respectively. The jet velocity goes up from the left to the right . . . . .	72
4.5	Isocontours of temperature and $Y_{\text{OH}}$ for selective $U_0$ . . . . .	73
4.6	$S_e/S_L$ in relation to jet velocity . . . . .	75
4.7	Radial distribution of $U_z$ and $\xi$ at selective $\tau_{\text{flow}}$ for all $U_0$ . . . . .	76
4.8	Radial distribution of $U_z$ and $\xi$ at selective $\tau_{\text{flow}}$ for $U_0 = 6.7$ m/s . . . . .	77
4.9	Isocontours of $Y_{\text{OH}}$ with $\tau_{\text{flow}}$ for $U_0 = 6.7$ m/s, dash dot line indicates stoichiometric mixture fraction isoline . . . . .	77
4.10	Variation of temperature and $\xi$ along center of $z$ axis and $S_L$ along center of $z$ axis for case $U_0 = 6.7$ m/s (a),(c) and 8.0 m/s (b), (d). . . . .	78
4.11	Schematic of $U_z$ and $S_e$ along $\tau_{\text{flow}}$ far upstream of the flamebase . . . . .	78
4.12	Simplified schematics of $U_z$ and $S_e$ along $\tau_{\text{flow}}$ at near the upstream of flamebase . . . . .	79

5.1	3-D volume rendering of the mass fraction of OH and HO <sub>2</sub> for Cases L, M, and H (from left to right). . . . .	86
5.2	Axial variation of conditional Favre mean of $\dot{q}$ (a) Case L, (b) Case M, (c) Case H and (d) Case Ig. . . . .	87
5.3	Axial variation of conditional Favre mean of $Da$ (a) Case L, (b) Case M, (c) Case H and (d) Case Ig. . . . .	88
5.4	Temporal evolution of $S_d^R$ and $S_d^D$ at the flamebase in $z = 0$ plane (a) Case L, (b) Case M, (c) Case H and (d) Case Ig. . . . .	90
5.5	Temporal evolution of $S_{d,avg}$ at the flamebase (a) Case L, (b) Case M, (c) Case H and (d) Case Ig. . . . .	91
5.6	Ignition kernel at the upstream of flamebase in Case Ig white solid line indicates $Y_{OH} = 0.001$ . . . . .	92
5.7	$\text{sign}(\lambda_e) \times \log_{10} (\max(1,  Da_c ))$ of each case (a) Case L, (b) Case M, (c) Case H and (d) Case Ig. . . . .	94
5.8	Combustion mode indicator $\alpha$ of each case (a) Case L, (b) Case M, (c) Case H and (d) Case Ig. . . . .	95
5.9	Combustion mode indicator $\alpha$ and PI 1 of Case Ig black solid line indicates $Y_{OH} = 0.001$ . . . . .	96
5.10	EI of H for Case H (left) and Ig (right) at the upstream of flamebase, black solid line indicates $Y_{OH} = 0.001$ . . . . .	97
5.11	$S_d^R$ for Case H (left) and Ig (right) at the upstream of flamebase, black solid line indicates $Y_{OH} = 0.001$ . . . . .	98

# Chapter I

## Introduction

### 1.1 Clean Combustion

Since the industrial revolution, the emission of greenhouse gases and air pollutants has increased significantly and is expected to keep growing in the foreseeable future, which is primarily attributed to the continuously increasing demand for fossil fuel in the area of transportation and power generation. In addition to the emission problem, the fossil fuel shortage will become eminent in the near future and as such, the demand for renewable energy development and highly-efficient clean combustion engines has grown significantly.

However, renewable energy only cannot support the whole amount of energy needs even in near future, suggesting that fossil fuel should be used in a smarter way by developing high-efficient engines which can operate even with low grade oil such as oil shale and sand oil. As the efficiency of power engines based on fossil fuels increases, the effect of energy saving becomes huge. In the conventional internal combustion (IC) engines, air pollutants such as soot and nitrogen oxide (NO<sub>x</sub>) are generated under high flame temperature and high equivalence ratio conditions. Therefore, the next-generation combustion systems are supposed to avoid such conditions and operate at low flame temperature and low equivalence ratio conditions, which is often called low temperature combustion (LTC). In general, LTC under lean, dilute, high-pressure, and low-temperature conditions has the potential to provide high diesel-like efficiency with very low NO<sub>x</sub> and particulate emissions. At these conditions, however, the characteristics of LTC are quite different

from that in the conventional combustion systems which are usually controlled by turbulent mixing and diffusion of molecules. In other words, LTC is thought to occur primarily through volumetric auto-ignition, largely in the absence of flames, and hence, is primarily controlled by chemical kinetics of the fuel–air mixture. In this study, several LTC system configurations are treated to elucidate LTC characteristics and stabilization mechanisms for each configuration.

## 1.2 Combustion of HCCI Engine

Homogeneous charge compression ignition (HCCI) is one of the variations of internal combustion in which homogeneously mixed fuel and oxidizer are compressed to the point of auto-ignition. The exothermic reactions in the HCCI engine can be converted into the work and heat. The concept of HCCI is mixed of the Otto engine and Diesel engine. The idea of HCCI engine is not up to date. In early twentieth century, hot bulb engines used an HCCI-like combustion system which used a hot vaporization chamber. Conventional compression ignition (CI) diesel engines have high efficiency with high compression ratio. CI engines, however, generates large amount of soot and nitric oxides  $\text{NO}_x$  [8–11]. Spark ignition (SI) engines generate low soot, however, it operates on high temperature which leads to producing a lot of  $\text{NO}_x$ . Overcoming the shortcomings of these CI and SI engines is the HCCI engine. HCCI engine system has high efficiency as CI engines and generates ultra low  $\text{NO}_x$  and soot. The HCCI engine has a compression ratio equivalent to the compression ratio of the CI engine. The operating condition of HCCI is low temperature and diluted fuel condition. The low temperature combustion (LTC) leads to low emission of  $\text{NO}_x$  and lean fuel condition make complete combustion and it reduces soot emission. HCCI engine is one of the LTC engines [11–18].

Despite these advantages, there are several issues to be solved to use the HCCI engines. Figure 1.1 shows the schematic of SI, CI and HCCI engines. HCCI engines have no mechanical combustion timing controllers such as a spark plug in SI engines and a fuel injector which controls the injection time fuel in CI engines. The ignition time of HCCI engines is controlled by totally in chemical kinetics. In addition, there is excessive heat

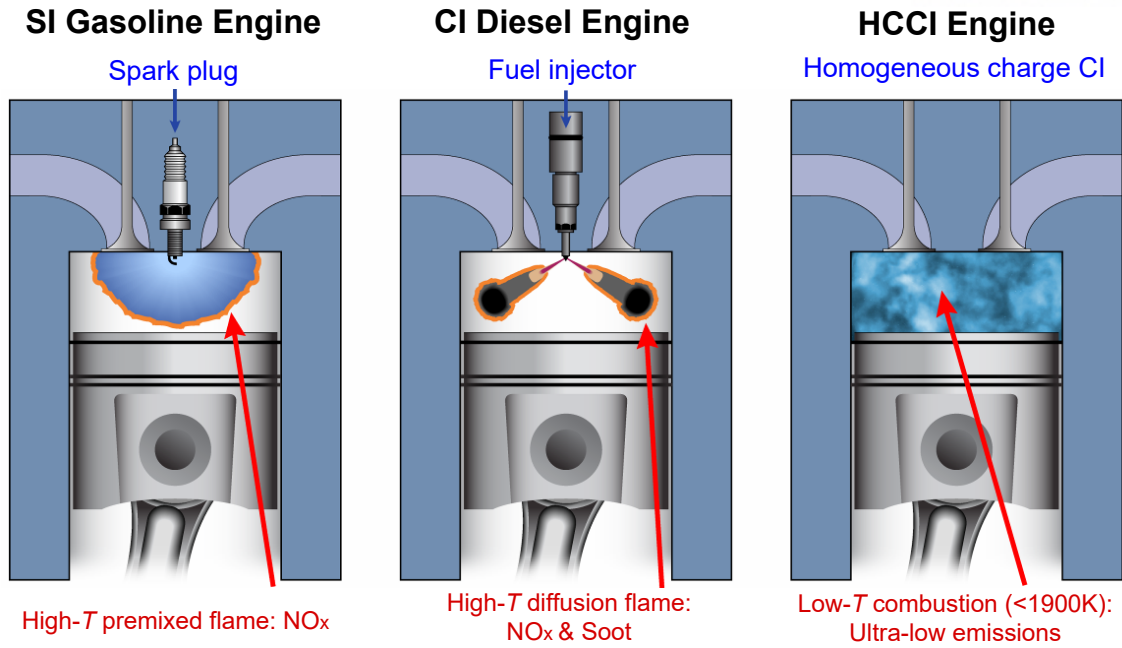


Figure 1.1: Schematic of spark ignition (SI) gasoline, compression ignition (CI) diesel, and homogeneous charge compression ignition (HCCI) engine combustion concepts, adapted from [1].

and pressure rise rate. Therefore, the exact amount of fuel and injection time that can operate properly while meeting environmental regulations in a precise modern IC engine becomes critical design elements. To solve these issues, studies on ignition characteristics and turbulence effect in the HCCI condition is essentially necessary. Identifying combustion characteristics and turbulence effect of ignition timing in HCCI engine cylinder will be treated in later part of this thesis.

### 1.3 Combustion of Lifted Flames

The lifted jet flames have been widely studied because of critical roles in their practical applications such as direct-injection stratified spark ignition engines, diesel engines and as a building-block configuration for elucidating auto-ignition. The stabilization mechanisms of a lifted flamebase have attracted attention because overall combustion characteristics of combustion system will be determined by its lifted flamebase [19]. For example, chemiluminescence measurements have shown the contribution of low tempera-



ture ignition kinetics in stabilizing a lifted jet flame [8, 20]. The laminar lifted jet flames are good reference to understand complex turbulent lifted flames. The laminar flamelet models in non-premixed turbulent combustion suggest that a turbulent flame is ensemble of laminar diffusion flamelets [21]. It is important to understand the fundamentals of laminar lifted flames in the LTC condition. Based on the knowledge of laminar lifted flames, applications of turbulent lifted flames in many modern LTC systems will be possible.

### 1.3.1 MILD Combustion

The moderate or intense low-oxygen dilution (MILD) combustion occurs when fuel is highly diluted and pre-heated up to temperatures higher than the auto ignition condition [22]. The MILD combustion systems have high efficiency and ultra low emissions in  $\text{CO}_2$ ,  $\text{CO}$  and  $\text{NO}_x$  with a energy saving. MILD combustion is considered as a reliable technology for clean and efficient combustion systems. A fundamental analysis of fuel oxidation under MILD combustion conditions is necessary to tune and control the real combustion systems. Many experimental and numerical studies were carried out to understand MILD combustion in laminar lifted flames [23–26]. The high dilution of fuel and pre-heating of reactants lead to an unusual combustion behaviors in laminar lifted flames [23, 24]. In normal non-premixed lifted jet flames, lift-off height increases as the jet velocity increases and eventually flames blow out at the jet velocity above a certain level. In MILD combustion, the lift-off height decreases as a jet velocity increases (see Fig.1.2).

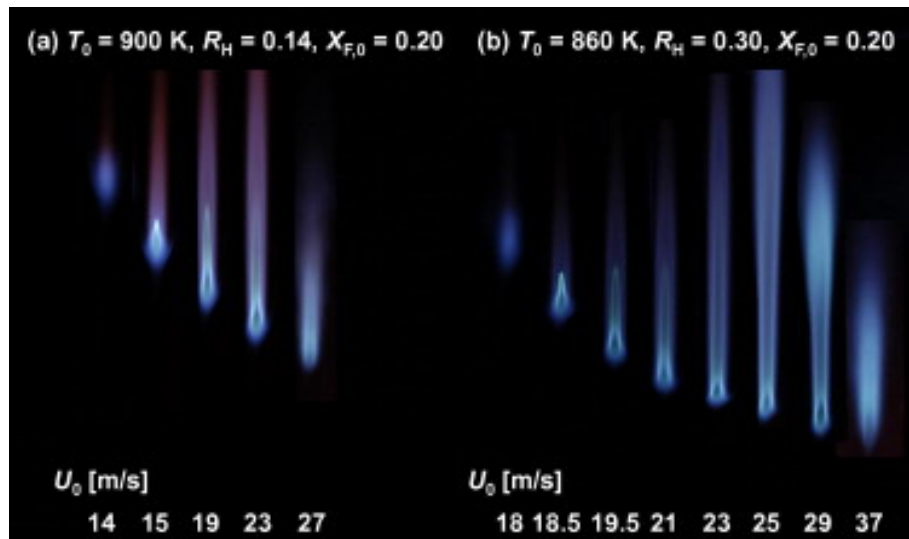


Figure 1.2: Autoignited methane/hydrogen lifted flames at various jet velocities for (Initial temperature, hydrogen ratio, initial fuel mole fraction) = (900 K, 0.14, 0.20) (a), and (860 K, 0.30, 0.20) (b)., adopted from [2]

## 1.4 Objectives

The objective of first part of thesis is to understand the ignition characteristics of different PRF/air mixtures at high pressure and intermediate temperature near the negative temperature coefficient (NTC) regime in HCCI engine combustion. For this purpose, we perform 2-D DNSs by varying three key parameters: 1) the fuel composition, 2) the initial temperature fluctuation, and 3) the initial turbulence intensity. Note that both of the initial temperature and composition fluctuations play an important role in HCCI combustion [27, 28]; in general, the equivalence ratio fluctuations enhance HCCI combustion together with temperature fluctuations when they are uncorrelated and retard it when negatively correlated. In section 2, however, we focus only on the effects of temperature fluctuations and turbulence rather than that of equivalence ratio fluctuations because large equivalence ratio fluctuations may be equivalent to large temperature fluctuations if the initial temperature of mixture is near or above the NTC regime. Note that PRF is a fuel mixture of pure *n*-heptane and *iso*-octane; for instance, PRF80 is comprised of 80% *iso*-octane and 20% *n*-heptane by liquid volume. The objective of the second and third part of this thesis are followed: (1) to understand the liftoff characteristics of autoignited laminar lifted jet flames, especially the reason of the occurrence of the decreasing behavior of  $H_L$  with  $U_0$  and sudden jump of  $H_L$ , and (2) to understand the flame stabilization and structure characteristics of the autoignited laminar lifted jet flames by performing 2-D detailed numerical simulations. The MILD combustion featured by very faint blue flame has many advantages in reducing soot and NO<sub>x</sub> due to its low flame temperature, and in achieving high thermal efficiency through its high reactant temperature [22, 29]. In the context of utilizing low flame temperature, the MILD combustion is quite similar to low temperature combustion (LTC) adopted in advanced IC engines. In the present study, therefore, the characteristics of autoignited laminar lifted flames with MILD combustion will also be investigated in section 3. In the last part of this study, 3-D DNSs of turbulent lifted hydrogen jet flames with different coflow temperatures near the auto-ignition limit are performed to elucidate their stabilization mechanisms and structure characteristics by examining instantaneous and time-averaged flame/flow characteristics near the flame-

base. The role of important species and reactions on the stabilization of turbulent lifted flames is investigated by adopting chemical explosive mode analysis (CEMA) [30–32].

# Chapter II

## Homogeneous Charge

## Compression-Ignition with PRF fuel

### 2.1 Introduction

The fundamental ignition characteristics of various fuel/air mixtures under lean, dilute, elevated pressure, and relatively low temperature have been widely investigated due to their practical relevance to homogeneous charge compression-ignition (HCCI) engine combustion [11,14–16,27,33–41]. An HCCI engine and its many variants have been considered as one of the most probable alternatives to the conventional internal combustion engines due to its potential to provide high diesel-like efficiency with very low pollutant emissions [11,14–16,27,33–41]. However, the development of prototype HCCI engines remains challenging because of their significant drawbacks in preventing an excessive pressure rise rate (PRR) under high-load conditions and controlling precise ignition timing of HCCI combustion. In general, the excessive PRR occurs due to volumetric auto-ignition throughout an HCCI engine cylinder. Moreover, HCCI engines have no explicit ignition method such that ignition timing in HCCI combustion is primarily governed by the chemical kinetics of fuel/air mixture, which depend highly on overall mixture composition, temperature, and pressure. Therefore, there have been many attempts to control the ignition timing and to alleviate the excessive PRR in HCCI combustion by applying different fuel injection strategies, fuel preparation, and thermal management including

exhaust gas recirculation (EGR) [11, 14–16, 27, 33–41].

Several computational studies of HCCI combustion using multi-dimensional direct numerical simulations (DNSs) have been conducted to elucidate the fundamental combustion characteristics of various fuel/air mixtures under HCCI conditions including hydrogen [42–46], dimethyl ether (DME) [47, 48], *n*-heptane [49], *iso*-octane [50], primary reference fuel (PRF) [51], ethanol [52], and biodiesel [28]. From these studies, the general characteristics of HCCI combustion have been elucidated; thermal stratification in an HCCI engine cylinder can spread out the PRR under high-load conditions by changing a combustion mode of spontaneous auto-ignition into a mixed combustion mode of spontaneous auto-ignition and deflagration [42–45, 49, 50]. In the presence of large temperature fluctuations, auto-ignition of hotter mixtures first occurs and evolves into deflagration waves, which spread to the unburnt mixtures sequentially until the remaining charge auto-ignites simultaneously. In general, the speed of the deflagration waves is much less than that of the spontaneous auto-ignition fronts and hence, the overall combustion is temporally spread out, resulting in a reduction of peak PRR.

In many previous DNS studies [42–46], the ignition characteristics of hydrogen/air mixtures exhibiting only one-stage ignition were investigated and as such, the effect of the negative-temperature coefficient (NTC) regime on HCCI combustion was not appreciated. The NTC regime usually appears as a result of the low-temperature oxidation of large hydrocarbon fuels exhibiting two-stage ignition. The effect of the NTC regime on HCCI combustion was first investigated by Yoo et al. [49] using 2-D DNSs of the ignition of a lean *n*-heptane/air mixture with different means and root-mean-squares (RMSs) of temperature. Recently, El-Asrag and Ju [47, 48] investigated the effects of EGR and temperature/mixture stratification on the ignition of synthetic DME by adding H<sub>2</sub>O<sub>2</sub> and NO to the initial mixtures. Bansal and Im [45], and Bhagatwala et al. [52] also investigated the effect of the equivalence ratio fluctuations on HCCI combustion and found that the equivalence ratio fluctuations enhance HCCI combustion together with temperature fluctuations when they are uncorrelated and retard it when negatively correlated.

It is of interest to note that in a previous DNS study of the ignition of PRF/air mixtures at elevated pressure and high temperature [51], it was found that the effect of

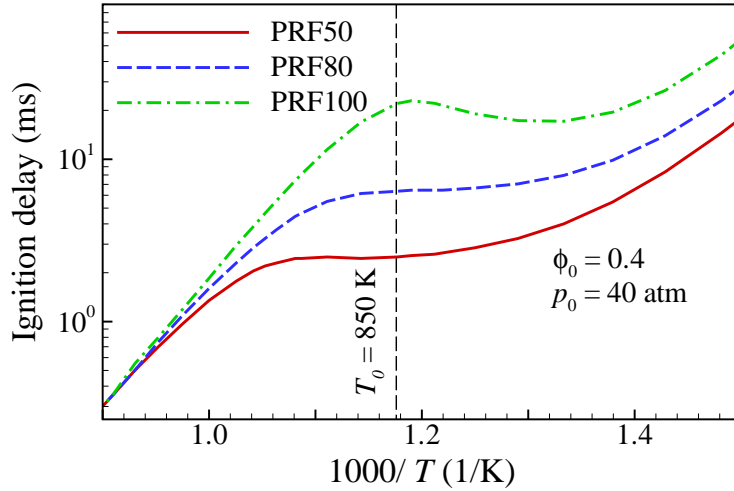


Figure 2.1: 0-D ignition delays as a function of initial temperature for different PRF/air mixtures at  $p_0 = 40$  atm and of  $\phi_0 = 0.4$ .

different fuel composition on the overall combustion vanishes with increasing temperature inhomogeneities. This is primarily attributed to the predominant deflagration mode of combustion at the reaction fronts and the nearly-identical propagation characteristics of different PRF/air deflagrations. It was also found that turbulence with large intensity and short timescale can effectively homogenize the initial mixtures, rendering the overall combustion to occur by spontaneous auto-ignition.

However, the homogeneous ignition delays of different PRF/air mixtures under high pressure and intermediate temperature conditions, which are more relevant to practical HCCI combustion, show a big disparity among the mixtures (see Fig. 2.1) and hence, it may be expected that the effect of fuel composition may not vanish even with large temperature fluctuations. Moreover, the early phase of ignition of a fuel/air mixture with very large temperature fluctuation may not be affected by turbulence [50]. In many previous studies [43, 44, 46, 49–51], it was found that turbulence is likely to homogenize the initial mixtures in HCCI combustion and hence, retard its overall combustion. On the contrary, it was also found [50, 52] that turbulence may enhance the overall spark-assisted compression ignition (SACI) combustion. These DNS results imply that the effect of turbulence on HCCI/SACI combustion may be inconclusive. The following sections will explain the the ignition characteristics of different PRF/air mixtures at high pressure

and intermediate temperature near the NTC regime.

## 2.2 Numerical Methods and Initial Conditions

For the present DNSs, the Sandia DNS code, S3D [53, 54], is used with a 116-species PRF/air reduced chemistry [51]. S3D solves compressible Navier-Stokes, continuity, total energy, and species continuity equations using a fourth-order, low storage, explicit Runge-Kutta method for time integration [55] and an eighth-order central differencing scheme for spatial discretization [56] with a tenth-order filter. CHEMKIN and TRANSPORT software libraries are linked with S3D to calculate reaction rates and thermodynamic and mixture-averaged transport properties. Details of the numerical algorithm and its implementation are provided in [53]. As in previous DNS studies of HCCI combustion [28, 49–51], periodic boundary conditions are applied in all directions and as such, ignition of PRF/air mixtures occurs at constant volume.

The skeletal and reduced mechanisms for PRF oxidation were developed for a previous DNS study of ignition of PRF/air mixtures under HCCI condition [51] based on the detailed LLNL mechanism [57, 58], using a strategy combining directed relation graph (DRG)-based methods, isomer lumping, and timescale analysis [51, 59–62]. The skeletal and reduced mechanisms were validated under various PRF composition, pressure, and temperature conditions. Readers are referred to [51] for details of the reduced mechanism.

For all DNSs, we adopted the initial uniform equivalence ratio,  $\phi_0$ , of 0.4, pressure,  $p_0$ , of 40 atm, and mean temperature,  $T_0$ , of 850 K, respectively.  $p_0$  of 40 atm and  $T_0$  of 850 K represent high pressure and intermediate temperature near the NTC regime to approximate the conditions in a hydrocarbon-fueled HCCI engine at the top dead center. Under the present initial conditions, the homogeneous ignition delays,  $\tau_{ig}^0$ , of PRF50 and PRF80 are found to be 2.5 and 6.3 ms, respectively. Henceforth,  $\tau_{ig}$  represents the time at which the maximum mean heat release rate (HRR) occurs for all simulations. The superscript 0 denotes the 0-D simulation. A total of ten different DNSs were performed in two dimensions by changing the initial physical conditions: different fuel compositions; temperature fluctuation RMS,  $T'$ ; and turbulence velocity fluctuation,  $u'$ .



Table II.1: Physical and numerical parameters of the DNSs.

Case	Fuel	$T'$ (K)	$l_e$ (mm)	$u'$ (m/s)	$\tau_t$ (ms)	$\tau_{ig}^0$ (ms)	$N$
1	PRF50	15	1.25	0.5	2.5	2.5	640
2	PRF50	60	1.25	0.5	2.5	2.5	640
3	PRF50	120	1.25	0.5	2.5	2.5	1280
4	PRF80	15	1.25	0.5	2.5	6.3	640
5	PRF80	60	1.25	0.5	2.5	6.3	640
6	PRF80	120	1.25	0.5	2.5	6.3	1280
7	PRF50	60	1.25	2.5	0.5	2.5	640
8	PRF50	120	1.25	2.5	0.5	2.5	1280
9	PRF80	60	1.25	2.5	0.5	6.3	640
10	PRF80	120	1.25	2.5	0.5	6.3	1280

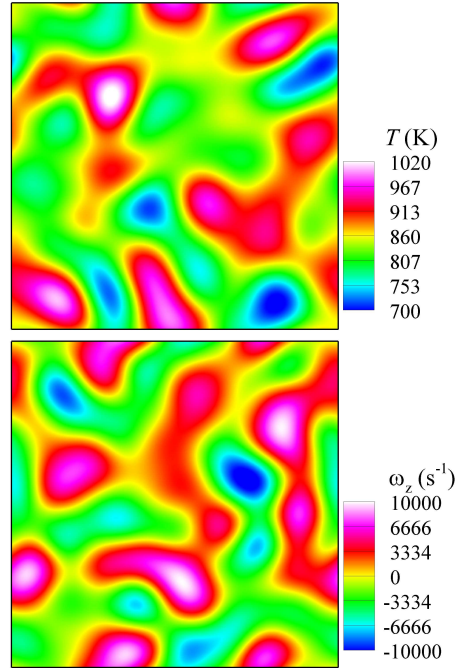


Figure 2.2: Initial temperature (top) and vorticity (bottom) fields of Case 2.

The initial turbulent flow field is prescribed by an isotropic kinetic energy spectrum function as in [42–44, 63–65]. The most energetic length scale of turbulence,  $l_e$ , is 1.25 mm. Note that the largest velocity fluctuations in real engines are about 5 m/s such that  $u'$  of 0.5 and 2.5 m/s adopted in the present study is quite comparable to that in real engines. Note also that the turbulence timescale in real HCCI engines is  $\sim O(1 \text{ ms})$  such that the turbulence timescale in this study, defined as  $\tau_t = l_e/u'$ , is representative of HCCI combustion. Similar to the initial turbulence field, the initial temperature fluctuation is generated by a temperature spectrum function. For all cases, the most energetic length scale of the temperature fluctuation,  $l_{Te}$ , of 1.25 mm is selected such that identical  $l_e$  and  $l_{Te}$  can produce the most effective turbulent mixing as found in [50]. Table II.1 shows the details of the physical and numerical parameters. Note that temperature and turbulence fields in the present study are uncorrelated as shown in Fig. 2.2.

From experiments of HCCI engine [66], it was found that  $T'$  is approximately 15  $\sim$  20 K without thermal management of initial mixture. Therefore,  $T' = 60$  or 120 K considered in the present study is somewhat large compared to that in real engines. However, these large  $T'$  can be achieved through direct injection or delayed-fuel injection in HCCI combustion. Furthermore, the spark ignition in SACI combustion [50] and the injection of highly-reactive fuel into an engine cylinder in reactivity controlled compression ignition (RCCI) combustion [67] can significantly reduce the ignition timing as large  $T'$  in the present study, and hence, it is also important to understand the characteristics of HCCI combustion with large  $T'$ .

It is of interest to note that 2-D turbulence without vortex stretching and tilting is different from 3-D turbulence. However, it is nearly impossible to do a parametric 3-D DNS study due to its great computational expense and hence, it is still valuable to investigate HCCI combustion using 2-D turbulence with a wide range of spectrum of time- and length-scales by systematically varying important parameters such as temperature and equivalence ratio fluctuations. Moreover, it was found from previous studies [42–45, 49–51] that turbulent mixing plays a secondary role in HCCI combustion compared to temperature stratifications. In addition, it was found from [46, 52] that 3-D turbulence may retard/enhance the overall HCCI/SACI combustion slightly more than 2-D turbulence

by homogenizing the initial mixtures/increasing turbulent flame area but its effect on overall HCCI/SACI combustion is not significant.

As in previous studies [49–51], a square box of  $3.2 \times 3.2 \text{ mm}^2$  is chosen for the computational domain, which is discretized with 640 or 1280 grid points,  $N$ , for the cases in Table II.1. In 2-D DNSs, the turbulent Reynolds numbers based on  $u'$  and the integral length scale for cases with  $u' = 0.5$  and  $2.5 \text{ m/s}$  are 69 and 347, respectively. The corresponding Kolmogorov length scales,  $\eta_K$ , are approximately  $17.5$  and  $5.3 \text{ }\mu\text{m}$ , respectively. For all DNS cases, therefore, the Kolmogorov length scale is resolved with at least a grid point [68]. In addition, the thinnest reaction layers in 2-D DNSs are resolved with at least  $12 \sim 18$  grid points and as such, turbulence and scalar fields are well resolved in the DNSs. All of the DNSs were performed either on the Cray XC30 at National Energy Research Scientific Computing Center or on the Cray XK7 at Oak Ridge National Laboratory.

## 2.3 Effect of Fuel Composition and Temperature

In the first parametric study, six different DNS cases (Cases 1–6) are simulated (see Table II.1 for detailed parameters of the DNSs) to elucidate the combined effect of the initial fuel composition and temperature fluctuation on the ignition of lean PRF/air mixtures. Different degrees of temperature fluctuation for different PRF/air mixtures are chosen: i.e.,  $T' = 15, 60, \text{ and } 120 \text{ K}$ .

### 2.3.1 Overall Ignition Characteristics

Figure 2.3 shows the temporal evolution of mean pressure,  $\bar{p}$ , mean HRR,  $\bar{q}$ , and mean PRR,  $\bar{p}$ , with different levels of temperature fluctuations for different PRFs (Cases 1–6), where “mean” represents the spatial average over the whole simulation domain. Note that the 0-D ignition delay of the PRF50/air mixture ( $\tau_{ig}^0 = 2.5 \text{ ms}$ ) is chosen as the reference time;  $\bar{q}$  for the cases with  $T' = 15 \text{ K}$  and 0-D cases are divided by 5. Several ignition characteristics of the PRF/air mixtures are to be noted. First,  $\bar{p}$  increases more slowly and  $\bar{q}$  is more distributed over time with increasing  $T'$  for all fuel compositions, similar

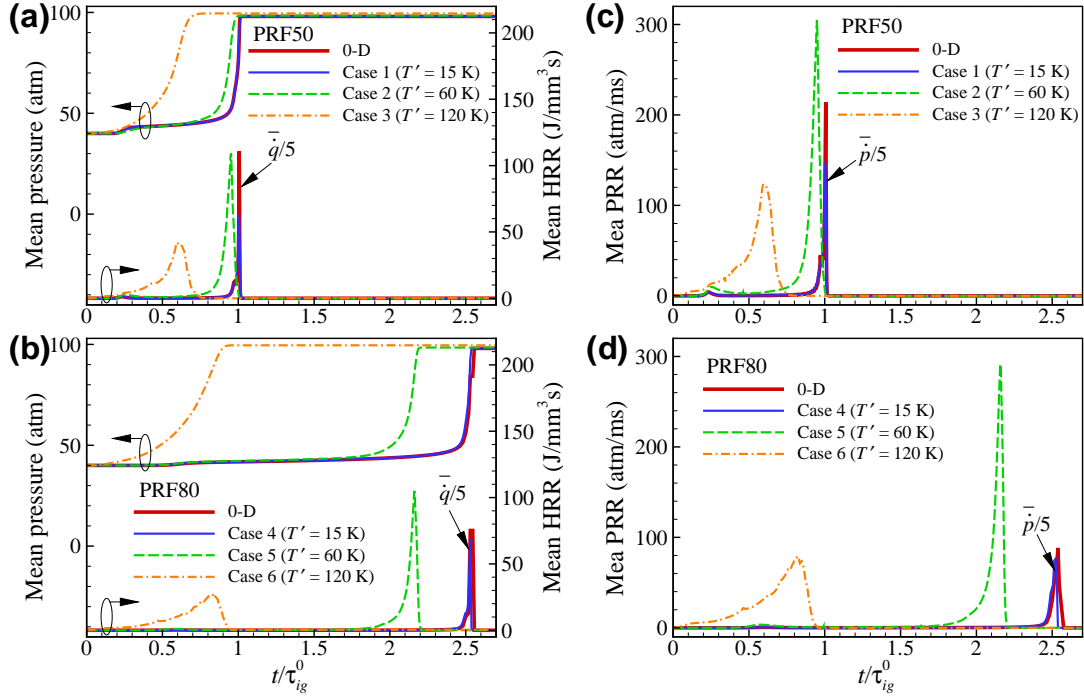


Figure 2.3: Temporal evolutions of the mean pressure and mean HRR (left) and the PRR (right) for Cases 1–3 (PRF50; a & c) and Cases 4–6 (PRF80; b & d).

to the results in previous studies [42–44, 49–51]. Moreover, the shapes of the overall combustion for Cases 1 and 4 with small  $T'$  are nearly identical to the corresponding 0-D ignitions. This is because the PRF50/air and PRF80/air mixtures exhibit nearly constant ignition delays at intermediate temperatures around 850 K as shown in Fig. 2.1, implying that mixtures with small  $T'$  are not able to take any advantage of temperature fluctuations to advance the overall combustion [49, 51].

Second, overall combustion occurs rapidly and the peak  $\bar{q}$  is reduced with increasing  $T'$  for the same PRF/air mixture, which results in prolonging the vigorous combustion phase. Similar results were also observed from the DNSs of hydrogen, *n*-heptane, *iso*-octane, and PRF HCCI combustion [43, 44, 49–51]. This is primarily attributed to the occurrence of deflagrations by the large degree of  $T'$ , leading to smoothing of  $\bar{q}$  and fast occurrence of overall combustion. As discussed earlier, large  $T'$  generally induces a mixed mode of deflagration and spontaneous auto-ignition, while small  $T'$  leads to spontaneous auto-ignition throughout the entire domain.

Third, for cases with the same  $T'$ , the effect of fuel composition is significantly reduced

with increasing  $T'$ . For cases with small  $T'$  (Cases 1 and 4),  $\tau_{ig}$  increases significantly with increasing *iso*-octane volume percentage in the PRF as can be expected from their  $\tau_{ig}^0$ ; i.e.,  $\tau_{ig}^0 = 2.5$  and  $6.3$  ms for PRF50 and 80, respectively. However, for cases with large  $T'$  (Cases 3 and 6), the difference between  $\tau_{ig}$  of the PRF/air mixtures is significantly decreased; i.e.,  $\tau_{ig}/\tau_{ig}^0 = 0.6$  and  $0.8$  for PRF50 and 80, respectively. This result implies that even at intermediate  $T_0$ , the effect of different fuel compositions of PRFs on HCCI combustion may vanish with increasing  $T'$ , similar to the PRF HCCI combustion at high  $T_0$  [51].

To further identify the overall combustion characteristics of the 2-D DNS cases, the temporal evolutions of the mean mass fractions of important species and the mean HRR are shown in Fig. 2.4 for four representative cases (Cases 1, 3, 4, and 6) together with their corresponding 0-D ignitions. At the first stage ignition, reaction is initiated by the abstraction of H from a fuel molecule (RH) by  $O_2$  ( $RH + O_2 \rightarrow R + HO_2$ ), forming a cycle with  $R + O_2 + M \rightleftharpoons RO_2 + M$  to produce  $H_2O$  and alkylperoxide,  $O=ROOH$  [57, 58, 69, 70]. As such,  $HO_2$  increases significantly while *iso*-octane and *n*-heptane decreases rapidly during the first stage ignition of the 0-D ignitions as shown in Figs. 2.4a and d. This low-temperature reaction cycle comes to an end when temperature exceeds a certain value at which the competing reaction,  $R + O_2 \rightarrow \text{olefin} + HO_2$ , terminates the first stage ignition. Subsequent exothermic reactions start to generate olefin and  $H_2O_2$ , increasing temperature slowly until the chain branching reaction,  $H_2O_2 + M \rightarrow OH + OH + M$ , becomes important [57, 58, 69, 70]. This reaction sequence proceeds rapidly until the increase of temperature becomes enough to initiate the high-temperature chain branching reactions, controlled by  $H + O_2 \rightarrow O + OH$ . This overall description of the HCCI combustion can be readily found from the 0-D ignitions (see Figs. 2.4a and d):  $H_2O_2$  is first accumulated from the first stage ignition, and then vanishes with a rapid increase of OH during the second stage ignition, which indicates the importance of  $H_2O_2$  in determining the second stage ignition delays.

It is also readily observed from Fig. 2.4 that the temporal evolutions of the important species in Cases 1 and 4 with small  $T'$  are nearly identical to those of the corresponding 0-D ignitions, which verifies the predominance of the spontaneous auto-ignition mode

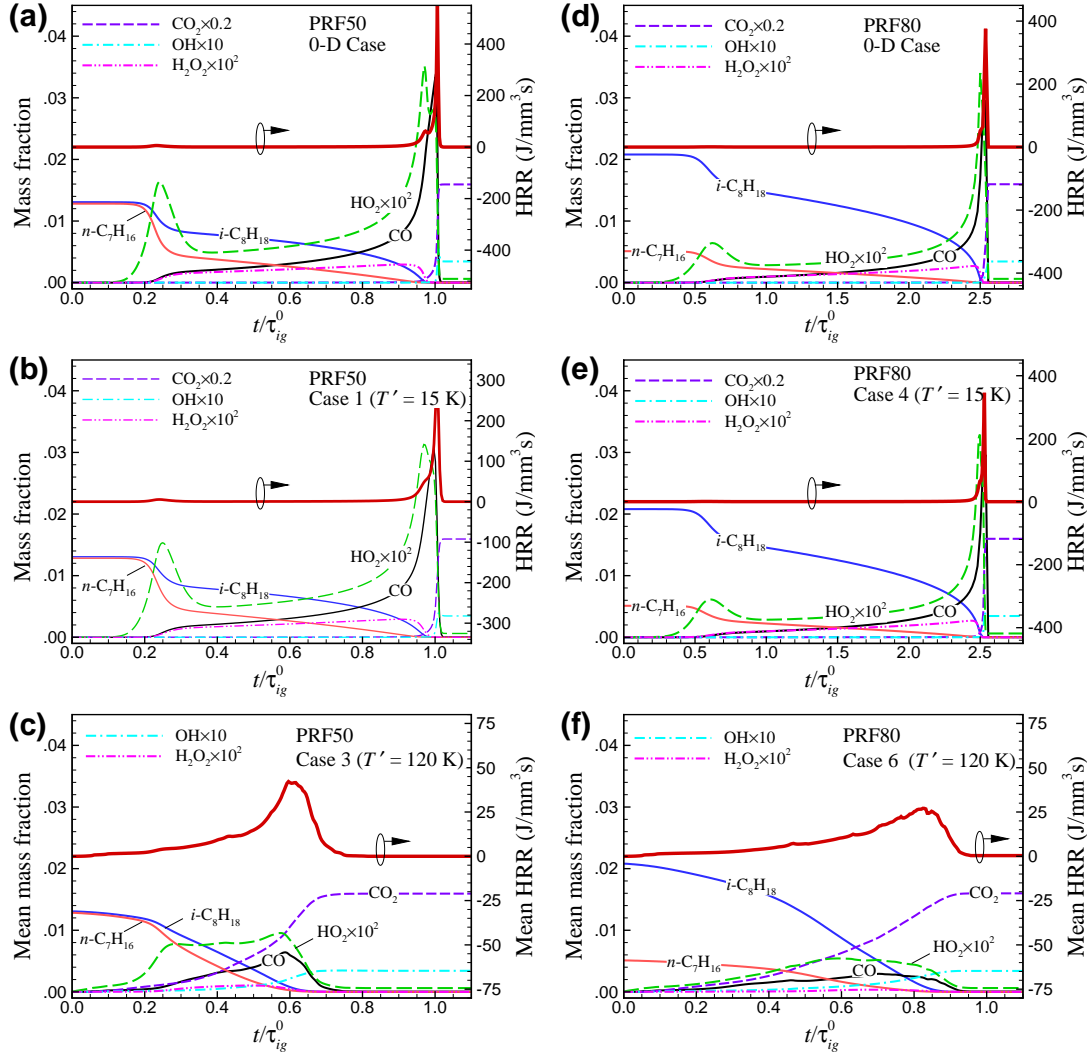


Figure 2.4: Temporal evolutions of the mean mass fractions of important species and mean HRR for (a) 0-D case of PRF50/air mixture, (b) Case 1, (c) Case 3, (d) 0-D case of PRF80/air mixture, (e) Case 4, and (f) Case 6.

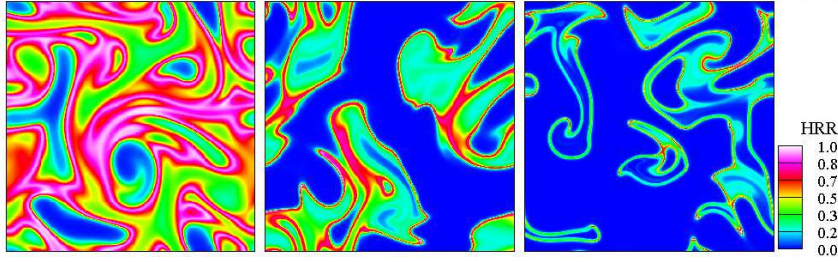


Figure 2.5: Isocontours of the normalized heat release rate for Cases 1–3 (from left to right) at  $t/\tau_{ig}^0 = 1.0, 0.94,$  and  $0.61,$  respectively.

of combustion during the whole combustion. Unlike the cases with small  $T'$ , however, the overall combustion of Cases 3 and 6 with large  $T'$  proceeds gradually without two-stage ignition characteristics; *iso*-octane and *n*-heptane are consumed more gradually; the production of CO and CO<sub>2</sub> are more distributed over time compared with those of the 0-D ignitions; CO<sub>2</sub> and OH do not have any peaks. These results imply that, rather than the spontaneous auto-ignition like the 0-D ignitions, deflagrations with a slow propagation speed can play a critical role in consuming the fuels and generating the products. Local high-temperature mixtures by large  $T'$  ignite very rapidly and develop into deflagrations such that the deflagration mode of combustion prevails over the entire domain, thereby leading to the temporal spread of HRR. The detailed analysis of localized physicochemical characteristics of HCCI combustion is an ongoing research topic.

As found in previous studies [42–44, 49–51], the deflagration mode of combustion can be dominant for cases with large  $T'$ , and hence, the propagation characteristics of each PRF/air deflagration wave become more important than the chemical kinetics associated with initiating nascent ignition kernels. Moreover, it is found from 1-D simulations that the laminar flame speeds of PRF/air mixtures with different octane numbers are nearly identical ( $S_L \approx 0.2$  m/s at  $p_0 = 40$  atm and  $T_0 = 850$  K). Therefore, it is reasonable to expect that overall combustion is not very different for different PRF/air mixtures, even though  $\tau_{ig}^0$  are widely different, particularly if  $T'$  is large enough to induce a sufficient amount of deflagration.

The ignition characteristics of PRF/air mixtures can be further identified by investigating the instantaneous isocontours of HRR for Cases 1–3 approximately at each  $\tau_{ig}$  as



shown in Fig. 2.5. The HRR,  $\dot{q}$ , is normalized by the maximum  $\dot{q}$  of the corresponding 0-D ignition of the PRF50/air mixture,  $\dot{q}_m^0 = 553.7 \text{ J/mm}^3\text{s}$ . It is readily observed that for small  $T'$  (Case 1),  $\dot{q}$  occurs nearly simultaneously over the entire domain as spontaneous ignition. For large  $T'$  (Case 3), however, high  $\dot{q}$  occurs in thin sheets while low levels of heat release exist in between. This suggests that the mixed mode of spontaneous auto-ignition and deflagration occurs in Case 3, which results in the advancement of the overall combustion, the temporal spread of  $\bar{\dot{q}}$ , and the reduction of peak  $\bar{\dot{q}}$ .

### 2.3.2 Chemical Explosive Mode Analysis

The ignition characteristics of PRF/air mixtures are further identified using the chemical explosive mode analysis (CEMA). CEMA has been developed for systematically detecting critical flame features such as ignition, extinction, and flame fronts and applied to DNSs of lifted flames in heated coflows [31, 71–73], reacting jets in cross-flows [74, 75], and ignition of hydrocarbon fuel/air mixtures under HCCI conditions [32, 49, 51].

CEMA is briefly summarized here and readers are referred to [72] for more details. In general, the local chemical characteristics in chemically reacting flows can thoroughly be accounted for by the Jacobian of the chemical source term,  $\mathbf{J}_\omega (\equiv \partial\omega/\partial\mathbf{y})$ , in the governing equations, where  $\mathbf{y}$  is the solution vector of species concentration and temperature, and  $\omega$  is the chemical source term. Chemical explosive mode (CEM) is then defined as an eigenmode of  $\mathbf{J}_\omega$  where the real part of the eigenvalue,  $\lambda_e$ , is positive [72]. By definition, CEM represents the reciprocal chemical timescale of a local mixture such that a mixture with CEM is destined to explode if it is isolated from any significant loss in heat or radicals. Therefore, CEM can be considered as an intrinsic chemical feature of ignitable mixtures.

To measure the competition between CEMs and the losses, a Damköhler number,  $Da_c$ , is adopted, which is defined as:

$$Da_c = \lambda_e \cdot \chi^{-1}, \quad (2.1)$$

where scalar dissipation rate,  $\chi (= 2D|\nabla c|^2)$ , represents a reciprocal characteristic timescale of the diffusion or loss term [31, 32, 51, 72, 73]. Note that  $c$  and  $D$  are the progress variable



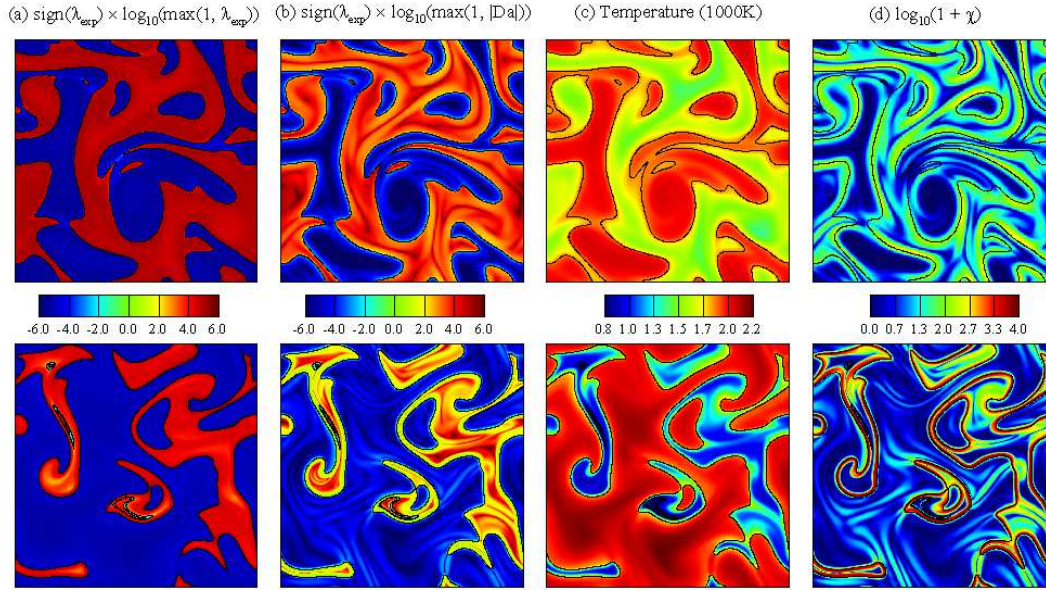


Figure 2.6: Isocontours of (a) the timescale of the chemical explosive mode, (b)  $Da_c$ , (c) temperature, and (d)  $\chi$  for Case 1 (top) at  $t/\tau_{ig}^0 = 1.0$  and Case 3 (bottom) at  $t/\tau_{ig}^0 = 0.61$ . The solid line denotes the reaction front ( $Da_c = 1$ ).

and the thermal diffusivity of local mixture, respectively.  $c$  is defined as  $c \equiv Y_c/Y_c^{Eq}$ , where  $Y_c = Y_{CO_2} + Y_{CO}$ , and  $Y_c^{Eq}$  is the corresponding equilibrium value of  $Y_c$ . A mixture with large positive  $Da_c$  will likely lead to actual ignition. However, a mixture with large negative  $Da_c$  represents strongly burning flames. Note that  $Da_c = 1$  indicates ignition or extinction states of steady state combustion.

Figure 2.6 shows isocontours of  $\lambda_e$ ,  $Da_c$ ,  $\chi$ , and temperature for Cases 1 and 3 at each  $\tau_{ig}$ . To clearly show the reaction fronts,  $\lambda_e$  and  $Da_c$  are shown on a logarithmic scale together with the sign of  $\lambda_e$  such that large positive values in Figs. 2.6a and b represent unburned mixtures while large negative values denote burned mixtures. For both cases, the reaction fronts represented by the thick black lines ( $Da_c = 1$ ) separate the burned and unburned mixtures and correspond to either spontaneous ignition or deflagration. It is readily observed from the figures of  $Da_c$  that for Case 1, the reaction fronts delineate the auto-igniting (red) region with large positive  $Da_c$  from the post-ignition (blue) region with large negative  $Da_c$ . It is also of interest to note that  $Da_c \gg O(1)$  upstream of the reaction fronts indicates that the reaction fronts are spontaneous ignition.

For Case 3, however, there exist three distinct regions: an auto-igniting region (red), a post-ignition region (blue), and a deflagration region (green). The green region represents reaction fronts upstream of the auto-igniting region which coincide with strips where  $\chi$  balances  $\lambda_e$ , a feature of deflagration waves propagating through unburned mixtures prior to the occurrence of auto-ignition. These results also indicate that the reaction fronts of Case 3 are deflagration waves rather than spontaneous ignition fronts.

## 2.4 Effect of Turbulence

In most previous DNS studies of HCCI combustion [43, 44, 49–51], it was found that turbulence with short  $\tau_t$  and large  $u'$  is more effective at dissipating initial temperature inhomogeneities than that with long  $\tau_t$  and small  $u'$ . Therefore, overall combustion is retarded while occurring by spontaneous ignition. However, it was also found from [50] that turbulence with short  $\tau_t$  and large  $u'$  can advance overall SACI combustion by increasing turbulent flame area. In this section, therefore, the effect of turbulence on the ignition of PRF/air mixtures is elucidated. Four DNSs (Cases 7–10) were performed with greater  $u'$  for different PRF/air mixtures (see Table II.1 for details of the parameters).

Figure 2.7 shows the temporal evolution of  $\bar{p}$  and  $\bar{q}$  for the additional cases with  $u' = 2.5$  m/s and the corresponding cases with  $u' = 0.5$  m/s for PRF50 and PRF80. Several points are to be noted from the figure. For cases with  $T'$  of 60 K, which is relatively small considering that it induces a small range of ignition delays of the initial mixture, turbulence with short  $\tau_t$  and large  $u'$  can effectively homogenize the mixtures. Therefore, both  $\tau_{ig}$  and the peak of  $\bar{q}$  are increased and overall, combustion is more apt to occur by spontaneous ignition for both PRF/air mixtures. For cases with a larger  $T'$  of 120 K, however,  $\tau_{ig}$  is reduced and the peak value of  $\bar{q}$  is increased with increasing  $u'$ . This is opposite to the cases with small  $T'$  and what was found in previous studies [43, 44, 49–51]. This result is more similar to the ignition characteristics of SACI combustion [50].

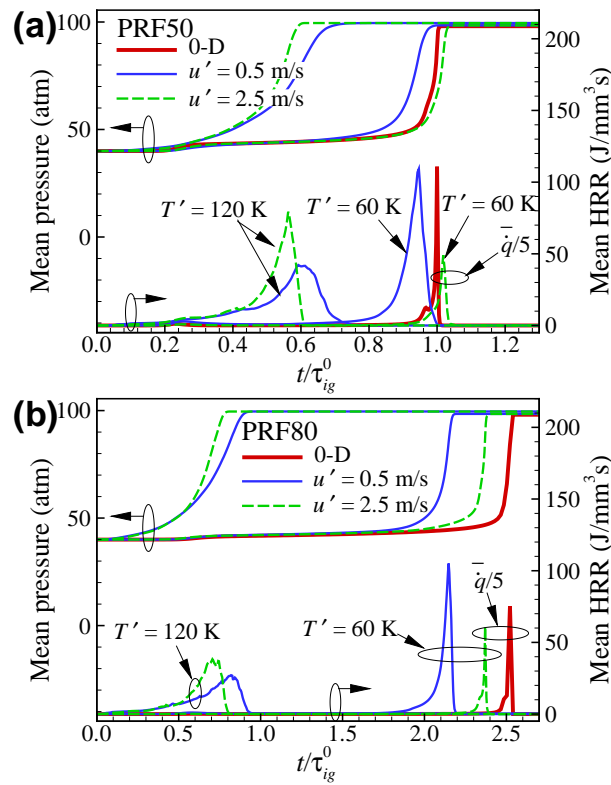


Figure 2.7: Temporal evolutions of the mean pressure and mean HRR for (a) PRF50 and (b) PRF80.

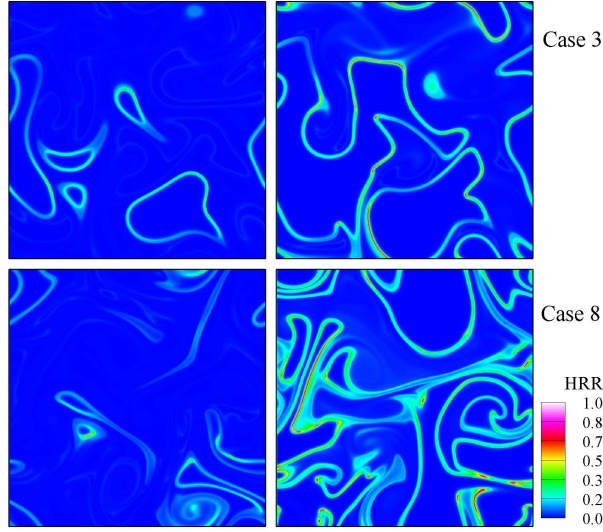


Figure 2.8: Isocontours of the normalized heat release rate for Cases 3 (top) and 8 (bottom). From left to right,  $t/\tau_{ig}^0 = 0.36$  and  $0.52$ , respectively.

### 2.4.1 Ignition Damköhler Number

To quantify the effect of turbulence on the early ignition characteristics, we introduce an ignition Damöhler number,  $Da_{ig}$ , which evaluates the overall competition between ignition and turbulence dissipation during the early phase of HCCI combustion:

$$Da_{ig} = \tau_t / \tau_{ig,10\%}, \quad (2.2)$$

where  $\tau_t$  is the turbulence timescale of the initial turbulence and  $\tau_{ig,10\%}$  is the lowest 10% ignition delay of the initial mixture, which represents the shortest ignition timescale of the initial mixtures. If  $Da_{ig} \gg O(1)$ , the occurrence of nascent ignition kernels and their evolution to deflagrations are nearly independent of turbulence. On the contrary, if  $Da_{ig} \lesssim O(1)$ , ignition is significantly affected by turbulence. Note that if  $Da_{ig} \ll O(1)$ , the homogenization of the initial mixture by turbulence is finished much earlier than the corresponding 0-D ignition delay and, as such, overall combustion becomes similar to homogeneous 0-D ignition.

For Cases 2 and 7 ( $T' = 60$  K),  $Da_{ig} = 1.85$  and  $0.37$  ( $\tau_{ig,10\%} \approx 1.35$  ms), respectively and hence, the development of nascent ignition kernels is more disturbed by turbulence in Case 7; the initial mixture is more homogenized by large  $u'$  with short  $\tau_t$ ; consequently, the overall combustion of Case 7 is retarded as shown in Fig 2.7. For Cases 3 and 8 ( $T'$

= 120 K), however,  $Da_{ig} = 14.5$  and  $2.9$  ( $\tau_{ig,10\%} \approx 0.17$  ms), respectively such that the early phase of ignition becomes nearly independent of turbulence. Once deflagrations are developed from the ignition kernels, their evolutions can be highly affected by local turbulence. For these cases, the turbulent flames exist within the corrugated flamelet and thin reaction zone regimes [19, 76] such that large  $u'$  of Case 8 advances the overall combustion by increasing turbulent flame area compared to Case 3. The turbulent flame regime will further be discussed in the next section. Figure 2.8 shows the instantaneous isocontours of HRR for Cases 3 ( $u' = 0.5$  m/s) and Case 8 ( $u' = 2.5$  m/s), which readily identify the increase of turbulent flame area by large  $u'$  of Case 8. Note that the above  $Da_{ig}$  analysis holds for Cases 7–10 within the range of  $0 \sim 20\%$  of  $\tau_{ig}$  in  $Da_{ig}$ .

It is of interest to note that even for the SACI cases of which mean temperature is above the NTC regime (see Cases 4 and 10 in [50]), the ignition Damköhler number analysis can directly be applied. From the results of the two SACI cases, it is readily observed that the corresponding  $Da_{ig}$  of the two cases are  $\sim O(10)$ . As such, large  $u'$  of Case 10 results in the advancement of the overall combustion compare to that of Case 4. Note that the high temperature source can be regarded as large  $T'$  in the present study.

The occurrence of the early deflagration can be identified by the density-weighted displacement speed,  $S_d^*$ , which also shows the propagation characteristics of the combustion waves.  $S_d^*$  is defined by [71, 77, 78]:

$$S_d^* = \frac{1}{\rho_u |\nabla Y_k|} \left( \dot{\omega}_k - \frac{\partial}{\partial x_j} (\rho Y_k V_{j,k}) \right), \quad (2.3)$$

where  $Y_k$ ,  $V_{j,k}$ , and  $\dot{\omega}_k$  denote the species mass fraction, the species diffusion velocity in the  $j$ -direction, and the net production rate of species  $k$ , respectively.  $\rho_u$  is the density of the unburnt mixture calculated from the local enthalpy and fresh mixture conditions [43, 44, 49–51]. The isocontour of  $Y_c = 0.065$  is chosen to evaluate the displacement speed for all cases as in previous studies [49–51]. This particular isocontour coincides approximately with the location of maximum  $\dot{q}$  of PRF/air mixtures.

Figure 2.9 shows the temporal evolutions of the mean front speed,  $\overline{S_d^*}$ , for the DNS cases, all of which are normalized by the corresponding laminar flame speed,  $S_L$ . As in previous studies [49, 50],  $S_L$  was estimated from a transient 1-D reactive simulation.

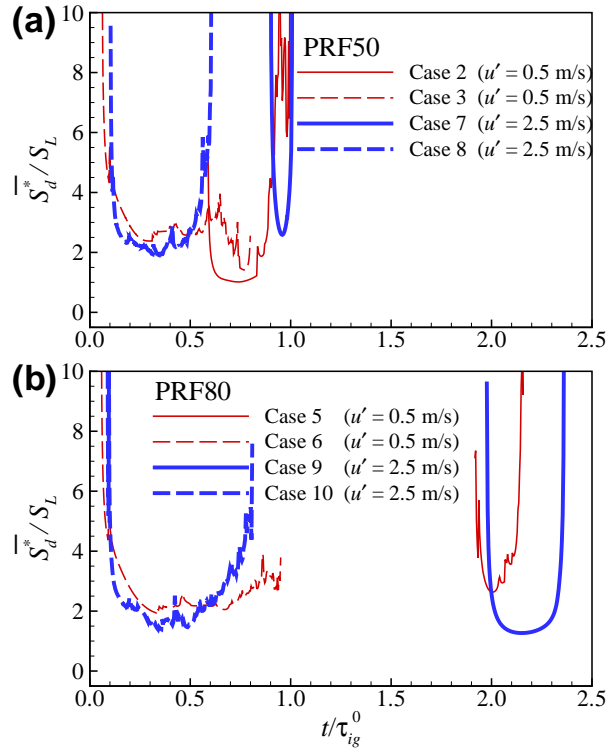


Figure 2.9: Temporal evolution of the mean front speed,  $\overline{S}_d^*$ , for (a) Cases 2, 3, 7, and 8 (PRF50) and (b) Cases 5, 6, 9, and 10 (PRF80).

The initial species composition, pressure, and temperature for the 1-D simulations were specified the same as those of the mean values in 2-D DNSs without any fluctuations. A high-temperature ignition source was then added on the initial constant temperature field to generate a combustion wave, which emanates from the source, propagating into the reactive mixture ahead of it. Auto-ignition in the reactive mixture does not occur prior to  $\tau_{ig}^0$  such that the measured displacement speed,  $S_d^*$ , of the combustion wave can be considered as the laminar flame speed,  $S_L$ , at the corresponding pressure.  $S_L$  is found to be approximately 0.2 m/s for all PRF/air mixtures and remain nearly identical during the combustion wave propagation.

As found in previous studies [43,44,49–51], the mean front speeds show a characteristic ‘U’ shape of HCCI combustion. The initial thermal run-away in the nascent ignition kernel results in large  $\overline{S}_d^*$  during the early phase of combustion. In the same way, the simultaneous auto-ignition of the unburned end-gas leads to the sudden increase of  $\overline{S}_d^*$  during the final phase of combustion [49–51,78].



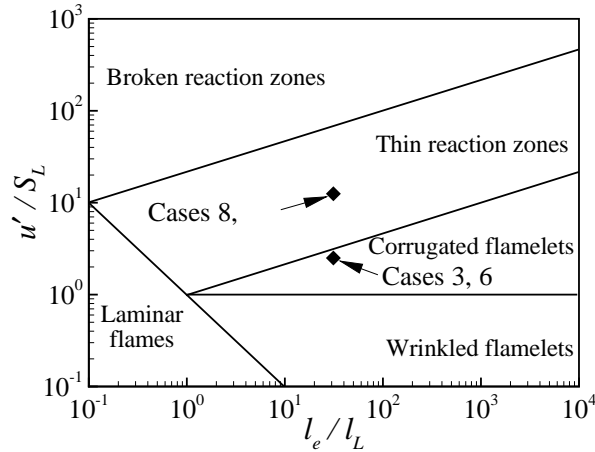


Figure 2.10: The locations of the cases with small  $u'$  (Cases 3 and 6) and large  $u'$  (Cases 8 and 10) in the regime diagram for turbulent premixed combustion.

It is also observed that after the initial thermal run-away,  $\overline{S_d^*}$  similar to  $S_L$  develops earlier with increasing  $T'$  and the duration of the region with a constant front speed at the bottom of the ‘U’ shape also increases with increasing  $T'$ . Note that the start of a relatively-constant front speed implies the occurrence of deflagrations. For the cases with large  $T'$ , the start of deflagration mode of combustion coincides regardless of fuel composition and  $u'$ , verifying that for cases with  $Da_{ig} \gg O(1)$ , the role of turbulent mixing on the development of nascent ignition kernels and their evolution into deflagrations is negligible.

## 2.5 Discussion

After the successful development of deflagrations from ignition kernels by large  $Da_{ig}$ , the temporal evolutions of deflagrations depend highly on their propagation characteristics and local turbulence conditions [19]. It is found from the present DNSs that the laminar flame thickness,  $l_L$ , and speed,  $S_L$ , are approximately 0.04 mm and 0.2 m/s, respectively. Therefore, for Cases 3 and 6,  $l_e/l_L \sim O(10)$  and  $u'/S_L \sim O(1)$ . For Cases 8 and 10, however,  $l_e/l_L \sim O(10)$  and  $u'/S_L \sim O(10)$ . As such, all turbulent flames with large  $T'$  exist within the corrugated flamelet and thin reaction zone regimes in the regime diagram for premixed turbulent combustion [19,76] as shown in Fig. 2.10. This implies that large  $u'$

induces more corrugated flame structures and thus, enhances the turbulent burning rate by increasing turbulent flame area as shown in Fig. 2.8. Note that for the cases considered in Fig. 2.10, the occurrence of the ignition kernels and subsequent development of the deflagrations are finished much earlier than one eddy turnover time of turbulence, and hence,  $u'$  and  $l_e$  are found to be nearly identical to those of the initial conditions such that the locations of the cases on the turbulent combustion regime remain the same.

In summary, two key parameters should be considered to understand the effect of turbulence on the characteristics of hydrocarbon-fueled HCCI combustion:  $Da_{ig}$  and  $u'/S_L$ . If  $Da_{ig}$  is large enough to successfully develop deflagrations in HCCI combustion, overall combustion can be advanced with large  $u'/S_L$  since the corresponding turbulent flames exist within the corrugated flamelet and thin reaction zone regimes. On the contrary, if  $Da_{ig}$  is small enough to disturb the early development of ignition kernels, the overall combustion is retarded because turbulence with short  $\tau_t$  and large  $u'$  can effectively homogenize the initial mixture fluctuations. It is of great importance to note that 2-D turbulence is qualitatively different from 3-D turbulence such that the findings from the present 2-D DNSs need to be verified and generalized by a parametric 3-D DNS study, which is a future research topic.

The analysis of  $Da_{ig}$  together with turbulent flame regime can be applied to SACI combustion; turbulence with large  $u'$  can advance the overall SACI combustion exhibiting very large  $Da_{ig}$  ( $\gg 1$ ) by spark ignition as in [50]. In the same way, it may be conjectured that 3-D turbulence in SACI combustion may also advance the overall combustion more than 2-D turbulence, which was observed in [52], because the effect of vortex stretching in 3-D turbulence can locally strengthen  $u'$  more than 2-D turbulence, resulting in the increase of turbulent flame area. Due to the same vortex stretching effect, 3-D turbulence with small  $Da_{ig}$  may retard the overall HCCI combustion more than 2-D turbulence by homogenizing the initial mixture inhomogeneities [46].

It is worth mentioning that in addition to the DNS studies of HCCI combustion, there have been many attempts to develop and validate turbulent combustion models for large eddy simulations (LES) and Reynolds averaged Navier-Stokes simulations (RANS) based on DNS data. Several models including flamelet-based models [79], probability



density function (PDF) based models [80], and conditional moment closure (CMC) based model [81] for HCCI combustion have been proposed. These combustion models show good agreements with DNS results especially for small temperature and composition stratifications. As such, the present DNS database can be further utilized to develop turbulent combustion models for HCCI combustion with large thermal stratifications.

## 2.6 Conclusions

The effects of PRF composition,  $T'$ , and  $u'$  on the ignition of lean PRF/air mixtures at high pressure and intermediate temperature are investigated by 2-D DNSs with a 116-species reduced mechanism. The chemical explosive mode and displacement speed analyses verify that larger  $T'$  induces greater temporal spreading of the mean HRR regardless of PRF composition because the deflagration mode is predominant at the reaction fronts for large  $T'$ . However, spontaneous ignition prevails for small  $T'$  and, hence, simultaneous auto-ignition occurs throughout the whole domain, resulting in an excessive HRR. The effect of fuel composition on the ignition of PRF/air mixtures is found to be significantly reduced with increasing  $T'$  because the deflagration mode prevails at the reaction fronts and the propagation characteristics of these deflagrations are nearly identical.

The ignition Damköhler number,  $Da_{ig}$ , defined by the ratio of turbulence timescale to the shortest ignition delay of initial mixtures, was proposed to evaluate the effects of turbulence on the early evolution of deflagrations from ignition kernels. For cases with  $Da_{ig} \lesssim O(1)$ , turbulence with large  $u'$  can effectively homogenize the mixtures and disturb the evolution of deflagrations from ignition kernels due to the short turbulence timescale compared to the ignition timescale. Therefore, the overall combustion is retarded and more apt to occur by spontaneous ignition. For cases with  $Da_{ig} \gg O(1)$ , however, the occurrence of nascent ignition kernels and their evolution to deflagrations are not affected by turbulence and the subsequent development of deflagrations occur only within the corrugated flamelet and thin reaction zone regimes of turbulent combustion. As such, turbulence with large  $u'$  can advance the overall combustion by increasing turbulent flame area.

## Chapter III

# Autoignited Laminar Lifted Methane/Hydrogen Jet Flames in Heated Coflow Air

### 3.1 Introduction

Numerous experimental and numerical studies of autoignition of various fuel/air mixtures have been conducted not only because it is one of the most important combustion phenomena [19, 70], but also because it appears in many practical combustion devices such as diesel engines, homogeneous charge compression ignition (HCCI) engine, and its variants [11, 16, 49, 50, 82]. In general, autoignition in an ideal HCCI engine occurs under adiabatic condition due to its homogeneities in both temperature and composition. However, autoignition in variants of HCCI combustion including stratified charge compression ignition (SCCI) [83, 84] and reactivity controlled compression ignition (RCCI) [82, 85, 86] combustion occurs non-adiabatically due to their mixture stratification and/or direct-fuel injection to control overall ignition timing and mitigate excessive pressure rise rate (PRR) in an engine cylinder. Similarly, autoignition in the diesel combustion occurs non-adiabatically due to its inherent mixture stratification. Therefore, the liftoff characteristics and stabilization mechanisms of turbulent lifted jet flames at high pressures and temperatures have been a long-time research topic to understand the fundamentals

of the diesel combustion [11, 19, 20, 71, 73].

The characteristics of autoignited laminar lifted jet flames in heated coflow air have also been investigated due to their distinct features from those of non-autoignited lifted jet flames and their potential as a building-block configuration for understanding turbulent lifted jet flames at high pressures and temperatures. For instance, stabilization mechanisms found from autoignited laminar lifted flames under various conditions can be used to understand those of turbulent lifted jet flames featured by complicated and transient nature. Chung and coworkers [2, 25, 87] found that an autoignition kernel in a laminar nonpremixed fuel jet in heated coflow air can develop into a stationary lifted flame or a nozzle-attached flame depending on the inlet conditions of the fuel jet and coflow air. They also elucidated that a stationary autoignited laminar lifted jet flame can exist regardless of the Schmidt number of the fuel jet, which implies that ignition delay can play a critical role in stabilizing laminar lifted jet flame under autoignitive conditions [25]. A tribrachial edge flame, or Moderate or Intense Low-oxygen Dilution (MILD) combustion features in the autoignited laminar lifted jet flames. The leading edge of the autoignited laminar lifted jet flames with tribrachial edge consists of lean/rich premixed flame wings and a trailing nonpremixed flame [88]. However, when the fuel jet is excessively diluted with an inert gas such as nitrogen, the conventional tribrachial edge flame does not exist and its flame structure changes to that of a MILD combustion with faint blue color without exhibiting a clear tribrachial structure [2, 23–26, 87, 88].

From previous studies of autoignited laminar lifted jet flames [25, 87], their liftoff height variation has been intensively investigated together with their flame structure characteristics. The liftoff height,  $H_L$ , of autoignited laminar lifted jet flames is found to be functions of the fuel jet velocity,  $U_0$ , and the 0-D adiabatic ignition delay of the stoichiometric fuel/air mixture based on the inlet condition,  $\tau_{ig,st}$ : i.e.,  $H_L \sim U_0 \tau_{ig,st}^2$ . This correlation was originally devised by Choi et al. [87] considering thermal balance between heat release from autoignition and heat loss by diffusion in a jet mixing layer. As such,  $H_L$  increases with increasing  $U_0$  for the same fuel and oxidizer jet conditions. This correlation is in good agreement with experimental data for autoignited lifted flames with tribrachial edge structure of various single component fuel jets [25]. For an autoignited

lifted jet flame with a MILD combustion, the  $H_L$  correlation was modified incorporating the ignition strength of the fuel jet [25]:  $H_L \sim U_0 \tau_{\text{ig,st}}^2 Y_{\text{F},0}$ , where  $Y_{\text{F},0}$  is the fuel mass fraction at the inlet [25]. For both  $H_L$  correlations of tribrachial edge flames and MILD combustion, we can readily observe a quadratic dependence of  $H_L$  on  $\tau_{\text{ig,st}}$ , which implies that the adiabatic 0-D ignition delay can play a critical role in stabilizing autoignited laminar lifted jet flames.

In a previous experimental study of autoignited laminar lifted methane/hydrogen jet flames [2], however, an unusual liftoff height variation with  $U_0$  was observed;  $H_L$  decreases with increasing  $U_0$  at relatively-low inlet temperatures and relatively-high hydrogen content. As such, the decreasing  $H_L$  with  $U_0$  does not follow the conventional autoignited laminar liftoff height behavior of  $H_L \sim U_0$ . It was conjectured that the unusual  $H_L$  behavior might be attributed to differential diffusion between methane and hydrogen molecules in the fuel jet. Moreover, due to the unusual characteristics of the autoignited laminar lifted methane/hydrogen jet flames, another unique feature of the flames was identified that the flame structure changes from a lifted flame with tribrachial edge to a MILD combustion with decreasing  $U_0$  although the fuel jet is not excessively diluted with an inert gas. According to previous studies of autoignited laminar lifted flames with a single component fuel such as methane and propane, the transition from a tribrachial edge flame to a MILD combustion was typically observed when the inlet fuel mole fraction is significantly low, or  $X_{\text{F},0} \sim O(0.01)$  [87, 88]. In the autoignition of methane/hydrogen jets in heated coflow air, however, a gradual transition from a tribrachial flame to a MILD combustion was observed with decreasing  $U_0$  even though the fuel jet is not highly diluted with nitrogen ( $X_{\text{F},0} \sim O(0.1)$ ).

The following sections will show (1) the liftoff characteristics of autoignited laminar lifted methane/hydrogen, especially the reason of the occurrence of the decreasing behavior of  $H_L$  with  $U_0$ , and (2) their flame stabilization and structure characteristics.

## 3.2 Numerical Methods

Detailed numerical simulations of autoignited laminar lifted methane/hydrogen non-premixed jet flames in heated coflow air are performed in an axisymmetric coflow burner configuration, which has been adopted in several previous experimental and numerical studies [2, 25, 26, 87, 88]. The steady compressible Navier-Stokes, species continuity, and energy equations are solved using laminarSMOKE [89, 90], which is an open-source code based on OpenFOAM [91] for simulations of multi-dimensional compressible laminar reacting flows with skeletal/detailed chemical mechanisms. For the detailed description of laminarSMOKE, readers are referred to [89, 90].

Figure 3.1 shows a schematic of the computational domain adopted in this study. The domain size is 6.65 cm  $\times$  50 cm in the radial  $r$ - and the axial  $z$ -directions. The inner diameter and thickness of the fuel nozzle are 3.76 mm and 0.5 mm, respectively. To take into account the effect of the finite thickness of the fuel jet nozzle on the flow, 3 cm long fuel nozzle is added to the main computational domain, which protrudes 1 cm above the coflow air inlet as shown in Fig. 3.1. Note that the configuration of the computational domain is identical to those of previous experiments and simulations [2, 25, 26, 87, 88].

No-slip and adiabatic boundary conditions are used for all the solid boundaries and symmetric boundary conditions are used for  $r = 0$ . For the inlets, the fuel inlet velocity is specified as that of a fully-developed pipe flow for which the mean velocity is  $U_0$ , and the coflow air velocity,  $U_C$ , is set to be 1.1 m/s. For both fuel and air inlets, constant inlet temperature,  $T_0$ , is specified. For the outlet, zero-gradient outflow boundary conditions are used. For all simulations, the pressure is atmospheric and the methane/hydrogen fuel jet is diluted with nitrogen such that the fuel mole fraction at the inlet,  $X_{F,0}$ , is 0.2. In the  $r$ -direction, a uniform grid space of 100  $\mu\text{m}$  is used for  $0 \leq r \leq 1.5$  cm to resolve the flame structure and a stretched grid is applied to the remaining domain. In the  $z$ -direction, the same uniform grid of 100  $\mu\text{m}$  is used. Figure 3.2 shows profiles of axial velocity, temperature, and mass fractions of  $\text{CH}_2\text{O}$  and  $\text{OH}$  of a lifted methane/hydrogen jet flame along the stoichiometric mixture fraction,  $\xi_{\text{st}}$ , isoline for three different grid resolutions, which verifies that the current grid size of 100  $\mu\text{m}$  can reasonably resolve the profiles compared

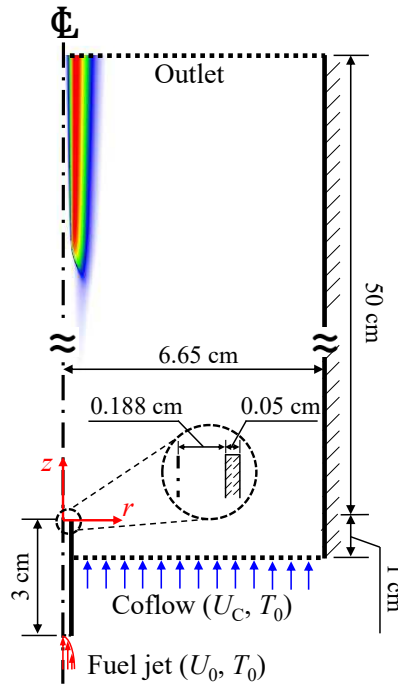


Figure 3.1: Schematic of the computational domain for simulations of autoignited laminar lifted methane/hydrogen jet flames in heated coflow air.

to a fine grid size of  $50 \mu\text{m}$ . The flame thickness,  $\delta_f \equiv (T_{\max} - T_{\min})/\max(dT/dx)$ , along the stoichiometric mixture fraction,  $\xi_{\text{st}}$ , isoline is found to be approximately 2 mm. Thus, the current grid space of  $100 \mu\text{m}$  can resolve the flame thickness with approximately 20 grids, which is sufficient to capture the flame structure and liftoff characteristics of autoignited laminar lifted methane/hydrogen flames. Even though the lifted flames are very thick under the present conditions, their rich premixed flame regions may not be sufficiently resolved by the current  $100 \mu\text{m}$  grids, which may influence the molecular diffusion and/or other processes. However, we found that the overall flame structure and stabilization characteristics of the current grid resolution are nearly identical to those of the fine grid resolution of  $50 \mu\text{m}$ , and as such, we believe that the effect of the unresolved part of the rich premixed flame region on the molecular diffusion is minimal if it exists. Note that the San Diego mechanism with 57 species [4] was used for the simulations. Also note that from a series of 0-D simulations of methane/hydrogen/nitrogen mixtures under the present simulation conditions using CHEMKIN [92], it is found that the decomposition of  $\text{CH}_4$  and  $\text{H}_2$  in the fuel nozzle rarely occurs and hence, does not affect the present

simulation results.

We initialize a lifted flame with high  $U_0$  without applying any external ignition source (i.e., literally autoignition). Then, we adjust  $U_0$  to obtain the liftoff height for other cases. In experiments, the autoignited liftoff height is repeatable. This implies that a liftoff height of an autoignited lifted flame is identical to that of a lifted flame obtained from another autoignited steady liftoff flame by changing the fuel jet velocity, which can be considered as a forced ignition. Otherwise, the liftoff height would not be repeatable. To further clarify whether final stabilization location and its stabilization mechanism depend on the initialization or not, we performed several transient numerical simulations of methane/hydrogen jet flames (not shown here). The flames locally autoignite and are soon stabilized at the same locations of the corresponding steady cases, which verifies that the lifted flames in the present simulation are autoignitable and the liftoff heights are also repeatable.

### 3.3 Overall Characteristics of The Lifted Flames

In previous experiments [2], the decreasing behavior of  $H_L$  with increasing  $U_0$  occurs under relatively-low  $T_0$  conditions ( $860 < T_0 < 920$  K) together with relatively-high hydrogen ratio in the fuel ( $R_H > 0.12$ ). The hydrogen ratio,  $R_H$ , is defined as  $R_H = X_{H_2}/(X_{CH_4} + X_{H_2})$ , where  $X_{H_2}$  and  $X_{CH_4}$  represent the mole fractions of hydrogen and methane in the fuel jet, respectively. Under relatively-high  $T_0$  and low  $R_H$  conditions, however, the opposite trend of the liftoff height can be observed (i.e.,  $H_L \sim U_0$ ). To numerically simulate the two different trends of the liftoff height variation, we chose two simulation conditions through several simulation tests: (1) relatively-high  $T_0 = 1100$  K and low  $R_H = 0.05$ ; henceforth, it is denoted as the high temperature low hydrogen (HTLH) condition, and (2) relatively-low  $T_0 = 940$  K and high  $R_H = 0.35$ , which is denoted as the low temperature high hydrogen (LTHH) condition. Note that  $T_0$  for both conditions are higher than those of previous experiments, which will be discussed in the following section.

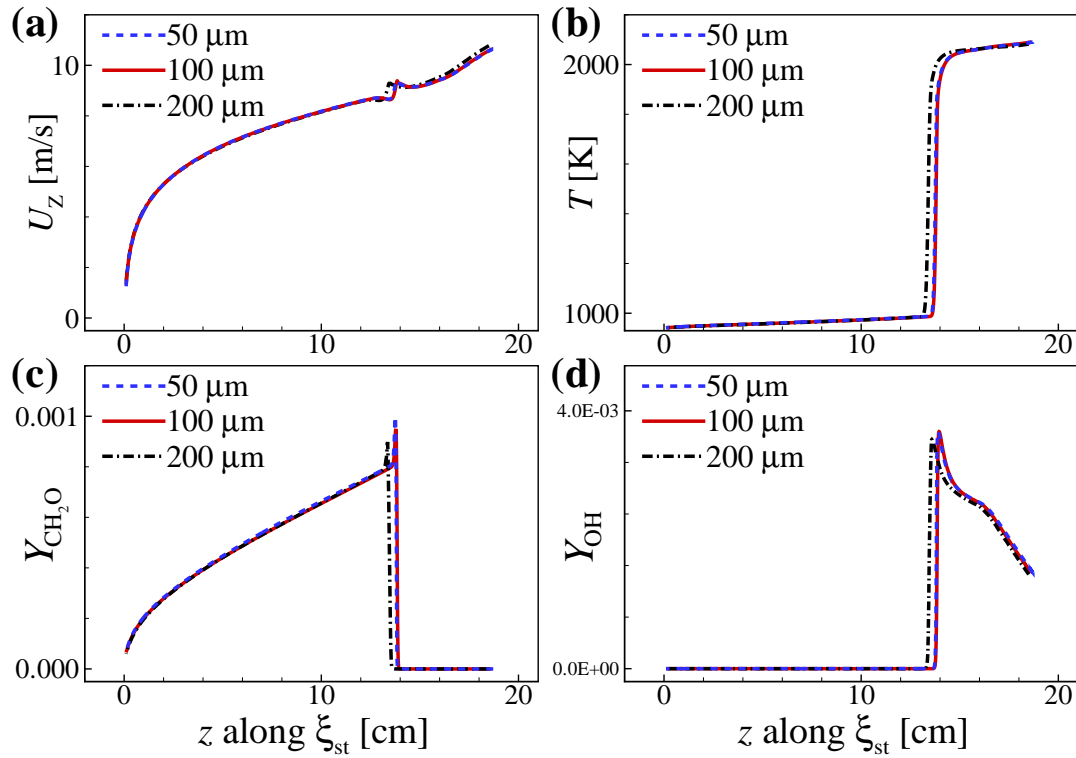


Figure 3.2: Profiles of (a) axial velocity, (b) temperature, and mass fractions of (c)  $\text{CH}_2\text{O}$  and (d)  $\text{OH}$  of a lifted methane/hydrogen jet flame along the stoichiometric mixture fraction,  $\xi_{st}$ , isoline for three different grid resolutions. The inlet temperature and velocity of the fuel jet are 940 K and 15 m/s, respectively, and the hydrogen volume fraction of the fuel jet is 0.35.



### 3.4 Chemical Kinetic Mechanisms

From previous numerical studies of autoignited laminar lifted jet flames [88, 93], it was reported that  $T_0$  of numerical simulations needs to be raised by approximately 100 K compared to that of experiments to obtain comparable  $H_L$  behavior. It was conjectured that this temperature discrepancy might be attributed to the inaccuracy of the chemical kinetic mechanism/transport data and/or experimental measurements. To select a proper chemical mechanism for the present study, therefore, we first tested several different methane oxidation mechanisms [3–7] by evaluating their stoichiometric laminar burning velocity,  $S_L$ , and 0-D ignition delays,  $\tau_{ig}^0$ .

Figure 3.3 shows  $S_L$  and  $\tau_{ig}^0$  of a stoichiometric methane/hydrogen/air mixture with  $X_{F,0} = 0.2$  and  $R_H = 0.35$  as a function of the inlet or initial temperature. It is readily observed that  $S_L$  increases and  $\tau_{ig}^0$  decreases with increasing temperature as expected. However,  $\tau_{ig}^0$  exhibits nearly an order of magnitude difference among the mechanisms for given temperature while  $S_L$  shows reasonable agreement, say, less than 10% difference at high temperatures relevant to the present simulation conditions.

These results can be attributed to inherent issues in developing a kinetic mechanism. A kinetic mechanism is typically validated for laminar burning velocities under atmospheric or mildly high pressures while it is done for ignition delays at high pressures due to the time limit of shock tube experiments ( $\sim O(1 \text{ ms})$ ). Thus, at the present atmospheric pressure condition, the mechanisms may not be accurate enough to predict ignition delays of  $\sim O(1 \text{ s})$ . The characteristics of  $\tau_{ig}^0$  at atmospheric and high pressures for different chemical kinetics mechanisms are further examined and the results are reported in the supplementary material, which shows that the variation of  $\tau_{ig}^0$  among the kinetic mechanisms becomes significant under the atmospheric pressure condition.

Since the characteristics of autoignited laminar lifted flames are significantly affected by both  $S_L$  and  $\tau_{ig}^0$ , we can expect that their numerical  $H_L$  values will appreciably vary depending on the chemical kinetic mechanisms. To evaluate the dependence of  $H_L$  on the choice of chemical kinetic mechanism, we performed 2-D numerical simulations of autoignited laminar lifted methane/hydrogen jet flames under the LTHH condition using

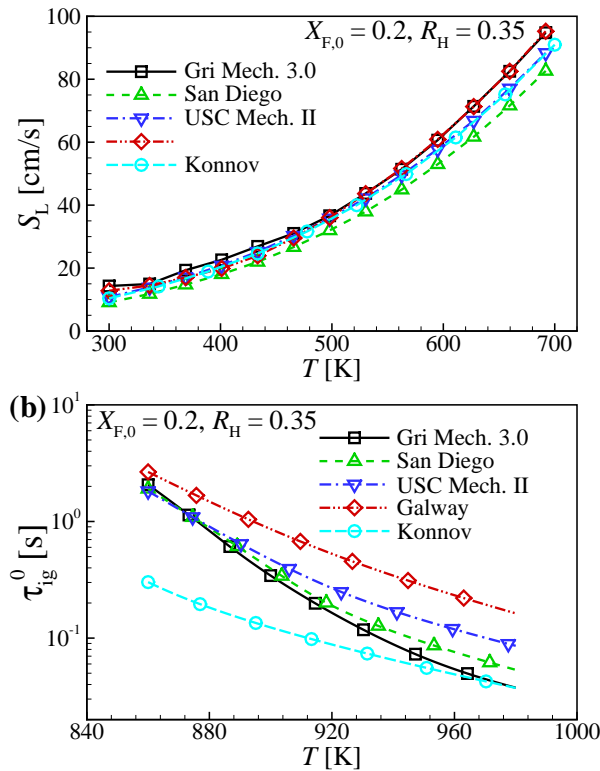


Figure 3.3: Variations of (a) laminar burning velocity,  $S_L$ , and (b) 0-D ignition delay,  $\tau_{ig}^0$ , of a stoichiometric methane/hydrogen/air mixture with  $X_{F,0} = 0.2$  and  $R_H = 0.35$  as a function of the inlet or initial temperature for several different chemical kinetic mechanisms including GRI-3.0 [3], San Diego [4], USC-II [5], Galway [6], and Konnov [7] mechanisms.

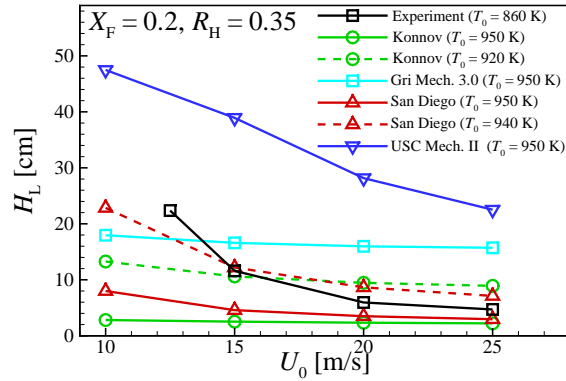


Figure 3.4: Variation of the liftoff height,  $H_L$ , of autoignited laminar lifted methane/hydrogen jet flames with  $X_{F,0} = 0.2$  and  $R_H = 0.35$  as a function of the inlet velocity,  $U_0$ , for several different chemical kinetic mechanisms and  $T_0$ .

four different chemical kinetic mechanisms and determined their  $H_L$  values as a function of  $U_0$  as shown in Fig. 3.4. Note that we first tested the four different chemical mechanisms at  $T_0 = 950$  K that is larger than the corresponding temperature of 860 K in the previous experiments [2]. This is because we could capture autoignited lifted jet flames within the computational domain with  $T_0 = 950$  K. Among the four mechanisms, we selected the Konnov [7] and San Diego [4] mechanisms because their  $H_L$  were expected to show a better agreement with the experimental data for lower  $T_0$ . Then, we carried out additional simulations by decreasing  $T_0$  for the two mechanisms to quantitatively match  $H_L$  to the experimental data as much as possible. Finally, we adopted the San Diego mechanism [4] for the following simulations.

It is readily observed from the result that even if there exists significant difference in  $H_L$  values, the decreasing tendency of  $H_L$  with  $U_0$  under the LTHH condition remains the same for all the chemical kinetic mechanisms with different  $T_0$ . Since the characteristics of autoignited lifted laminar methane/hydrogen jet flames are found to be qualitatively consistent with those of experiments for all the chemical mechanisms, we believe that the present simulations can properly elucidate the physico-chemical mechanism behind the decreasing  $H_L$  behavior observed from the experiments.

### 3.5 Lifted Jet Flames under HTLH Condition

Figure 3.5 shows the isocontours of temperature and mass fractions of OH, CH<sub>2</sub>O, and H<sub>2</sub>O<sub>2</sub> of autoignited laminar lifted methane/hydrogen jet flames for various fuel jet velocities under the HTLH condition (i.e.  $T_0 = 1100$  K and  $R_H = 0.05$ ). The dashed and dash-dotted lines represent the mixture fraction isoline passing through the flamebase,  $\xi_{fb}$ , and the stoichiometric mixture fraction isoline,  $\xi_{st}(= 0.325)$ , respectively. In the present study,  $\xi$  is calculated based on Bilger's mixture fraction formula [94] and the flamebase is defined as the most upstream point of  $Y_{OH} = 2.9 \times 10^{-4}$  isoline. The corresponding liftoff height is determined as the axial length from the fuel nozzle to the flamebase. Note that  $Y_{OH} = 2.9 \times 10^{-4}$  isoline represents approximately 5% of its maximum increase in the domain, which is consistent with definitions used in previous studies [71, 73]. It is readily observed that the flame is attached to the fuel nozzle up to, say,  $U_0 = 25$  m/s and becomes lifted for higher  $U_0$ . Once the flame is lifted, the liftoff height increases with increasing  $U_0$ . These are in qualitative agreement with previous experimental results [2].

Under this condition, the flamebase lies at a fuel-lean mixture as observed in previous studies of laminar/turbulent lifted flames in heated coflows [71, 73, 88, 95]. The shifting of the flamebase to the fuel-lean mixture implies that the stabilization mechanism of autoignited laminar lifted flames would be different from that of non-autoignited laminar lifted flames in which the flamebase coincides with a point of the stoichiometric mixture line where the edge flame propagation speed balances local flow velocity [96, 97]. Although the lifted flame is stabilized at the fuel-lean mixture, the maximum temperature and mass fraction of OH occur following the stoichiometric mixture line downstream of the flamebase, similar to previous numerical results [71, 73, 88, 93].

The isocontours of mass fraction of CH<sub>2</sub>O and H<sub>2</sub>O<sub>2</sub> are also shown in Fig. 3.5b to further identify the role of autoignition on the lifted flames. CH<sub>2</sub>O, HO<sub>2</sub>, and H<sub>2</sub>O<sub>2</sub> are important intermediate species during the early stage of hydrocarbon/air autoignition process, featuring that their concentrations attain their own peaks prior to the thermal ignition [73, 98, 99]. As such, they are regarded as precursors of autoignition. It is readily observed from the figure that CH<sub>2</sub>O and H<sub>2</sub>O<sub>2</sub> are predominant upstream of the

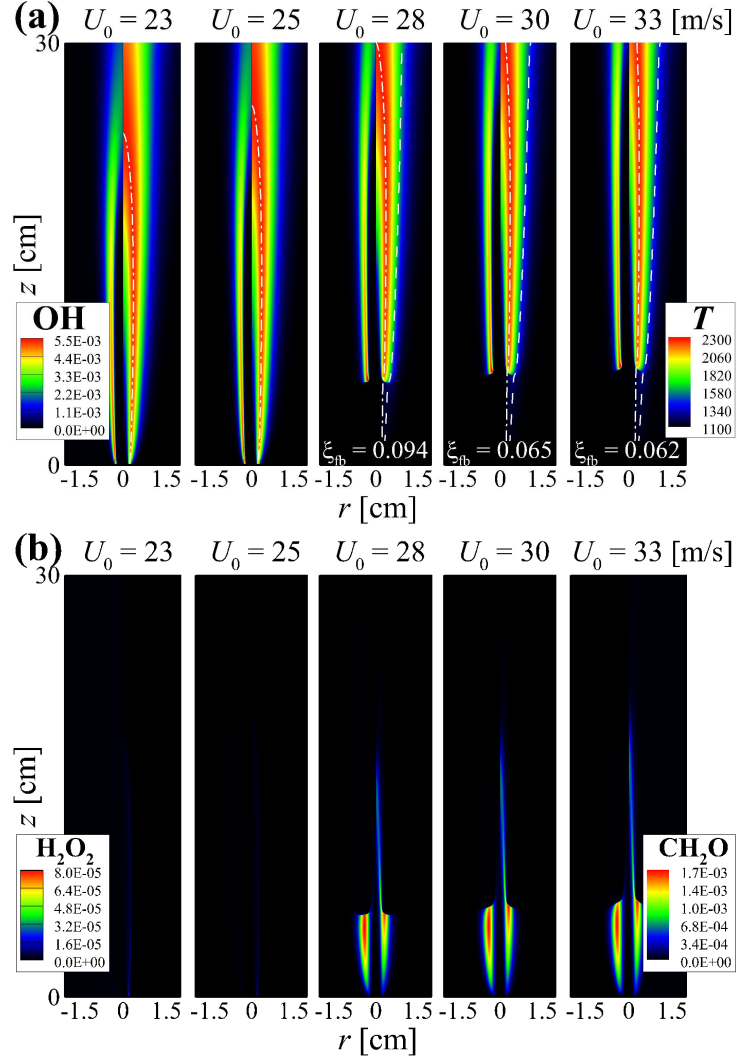


Figure 3.5: Isocontours of (a)  $Y_{OH}$  (left half) and  $T$  (right half) and (b)  $Y_{H_2O_2}$  (left half) and  $Y_{CH_2O}$  (right half) for autoignited laminar lifted methane/hydrogen jet flames for various fuel jet velocities  $U_0$  under the HTLH condition ( $T_0 = 1100$  K and  $R_H = 0.05$ ). The dashed and dash-dotted lines in (a) represent the mixture fraction isoline passing through the flamebase,  $\xi_{fb}$ , and the stoichiometric mixture fraction isoline,  $\xi_{st} (= 0.325)$ , respectively.

flamebase, which indicates that autoignition plays an important role in stabilizing the lifted flames [71, 73, 88]. Although not shown in here,  $\text{HO}_2$  behaves similarly to  $\text{H}_2\text{O}_2$ . Note that for non-autoignited lifted flames with low ambient temperature,  $\text{CH}_2\text{O}$  only exists near the premixed flame wing when a flame is stabilized by the balance of the propagation speed of edge flame and local flow velocity [24].

To summarize the overall characteristics of the lifted flames under the HTLH condition, the variations of  $H_L$  and  $(T_{\max} - T_0)/T_{\text{ig}}$  as a function of  $U_0$  are shown in Fig. 3.6. For comparison purpose,  $H_L$  variations from experiments [2] are also shown in the figure.  $T_{\max}$  is the maximum flame temperature in the domain and  $T_{\text{ig}}$  is the minimum temperature for autoignition of the stoichiometric mixture based on the inlet conditions. We determine that autoignition occurs within the computational domain if the ignition delay at  $T_0 = T_{\text{ig}}$  is less than one-jet flow-through time of the coflow air. Under the HTLH condition,  $T_{\text{ig}}$  is approximately 990 K from 0-D ignition tests using CHEMKIN [92].

In general, a combustion process can be defined as a MILD combustion when the following conditions are satisfied [22, 100]: (1) the inlet temperature of a reactant mixture is higher than its autoignition temperature,  $T_0 > T_{\text{ig}}$ , and (2) the maximum allowable temperature increase with respect to the inlet temperature is lower than its autoignition temperature,  $(T_{\max} - T_0)/T_{\text{ig}} < 1$ . For the present simulation cases,  $T_0$  is greater than  $T_{\text{ig}}$ , and as such, we adopt  $(T_{\max} - T_0)/T_{\text{ig}}$  to identify the combustion mode of the lifted flames: a lifted flame with tribrachial edge occurs when  $(T_{\max} - T_0)/T_{\text{ig}} > 1$  while a lifted flame with MILD combustion appears when  $(T_{\max} - T_0)/T_{\text{ig}} < 1$  is satisfied [22, 87, 100, 101]. As shown in Fig. 3.6,  $(T_{\max} - T_0)/T_{\text{ig}}$  is well above unity and  $T_0$  is great than  $T_{\text{ig}}$ , which indicates that only lifted flames with tribrachial edge appear under the HTLH condition.

### 3.6 Lifted Jet Flames under LTHH Condition

To capture the overall features of autoignited laminar lifted methane/hydrogen jet flames under the LTHH condition (i.e.  $T_0 = 940$  K and  $R_{\text{H}} = 0.35$ ), their temperature and the mass fraction of OH,  $\text{CH}_2\text{O}$ , and  $\text{H}_2\text{O}_2$  isocontours for various fuel jet velocities ( $U_0 = 4 \sim 30$  m/s) are shown in Fig. 3.7. Contrary to the cases under the HTLH condition, it is

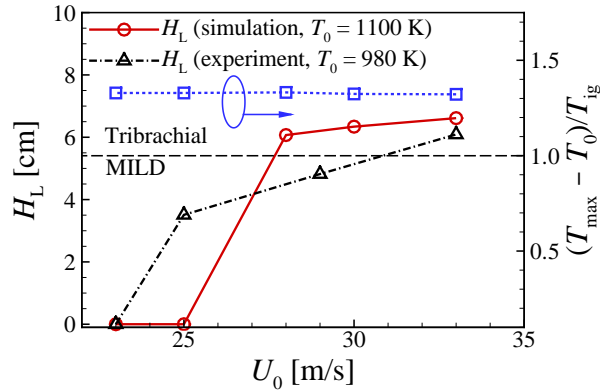


Figure 3.6: Variations of  $H_L$  (red) and  $(T_{\max} - T_0)/T_{\text{ig}}$  (blue) as a function of  $U_0$  for autoignited laminar lifted methane/hydrogen jet flames under the HTLH condition ( $T_0 = 1100$  K and  $R_H = 0.05$ ). The black dash-dotted line represents  $H_L$  variation of the corresponding experiments [2].

readily observed that  $H_L$  decreases with increasing  $U_0$ . Moreover, we cannot observe any nozzle-attached flames within the test range of  $U_0$ . As mentioned above, this unusual decreasing  $H_L$  behavior has been experimentally observed in [2].

To understand the lifted flame characteristics under the LTHH condition, the variations of  $H_L$  and  $(T_{\max} - T_0)/T_{\text{ig}}$  as a function of  $U_0$  are shown in Fig. 3.8, where  $T_{\text{ig}}$  is approximately 895 K under the LTHH condition. For comparison purpose, the corresponding experimental  $H_L$  variation [2] is also shown in the figure. Several points are noted from Figs. 3.7 and 3.8. First, the maximum temperature represented by  $(T_{\max} - T_0)/T_{\text{ig}}$  varies significantly for cases with  $U_0 \leq 10$  m/s, in which the stoichiometric contour height is lower than the flamebase where autoignition is governed by fuel-lean mixtures. Moreover,  $(T_{\max} - T_0)/T_{\text{ig}}$  first falls below unity at  $U_0 = 10$  m/s as  $U_0$  decreases and the overall flame structure changes from a lifted flame with tribrachial edge to a lifted flame with MILD combustion.

Based on the flame structure characteristics such as the location of the flamebase relative to the centerline and  $(T_{\max} - T_0)/T_{\text{ig}}$  values, we can classify the lifted flames under the LTHH condition into three different regimes as a function of  $U_0$ : (1) the lifted flame with tribrachial edge for  $(T_{\max} - T_0)/T_{\text{ig}} > 1$  (henceforth, denoted by the tribrachial edge flame regime;  $U_0 = 15 \sim 30$  m/s), (2) the lifted flame with MILD combustion

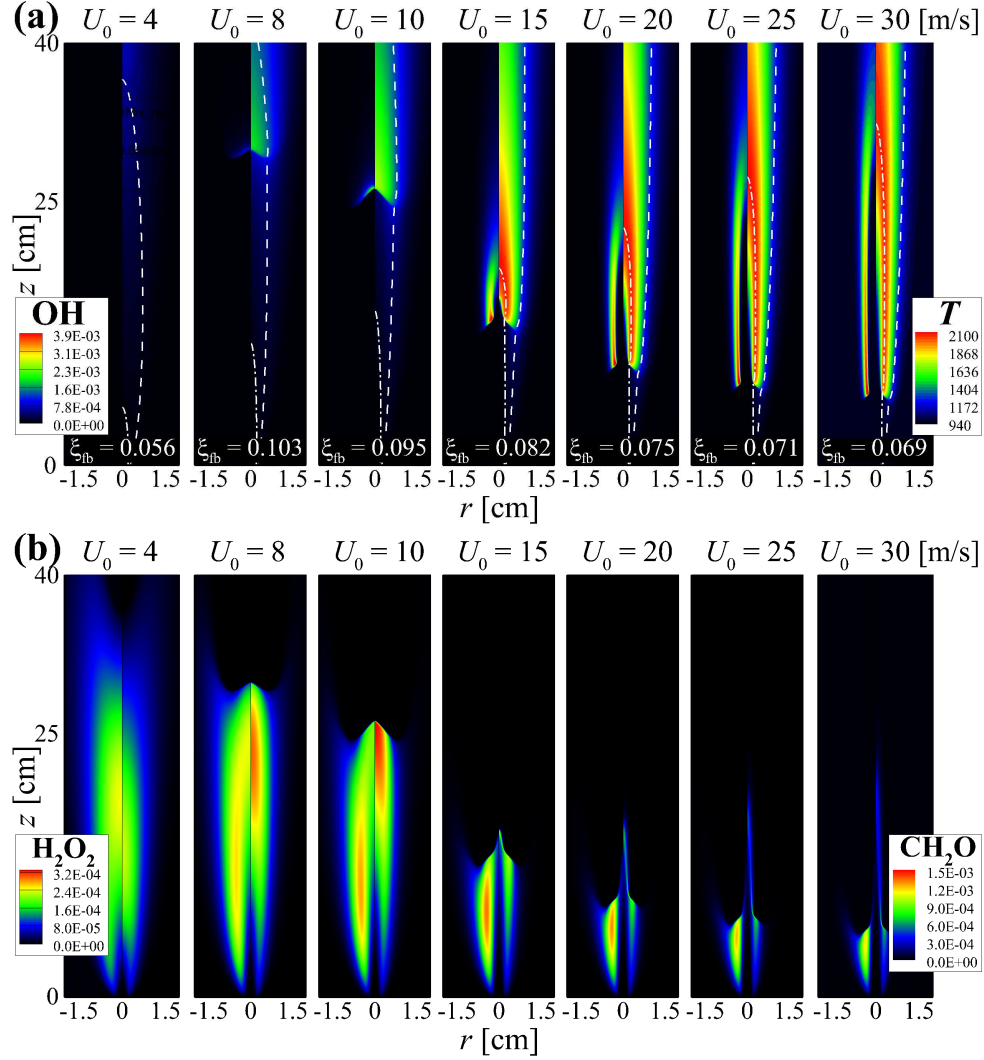


Figure 3.7: Isocontours of (a)  $Y_{OH}$  (left half) and  $T$  (right half) and (b)  $Y_{H_2O_2}$  (left half) and  $Y_{CH_2O}$  (right half) for autoignited laminar lifted methane/hydrogen jet flames for various fuel jet velocities  $U_0$  under the LTHH condition ( $T_0 = 940$  K and  $R_H = 0.35$ ). The dashed and dash-dotted lines in (a) represent the mixture fraction isoline passing through the flamebase,  $\xi_{fb}$ , and the stoichiometric mixture fraction isoline,  $\xi_{st} (= 0.378)$ , respectively.



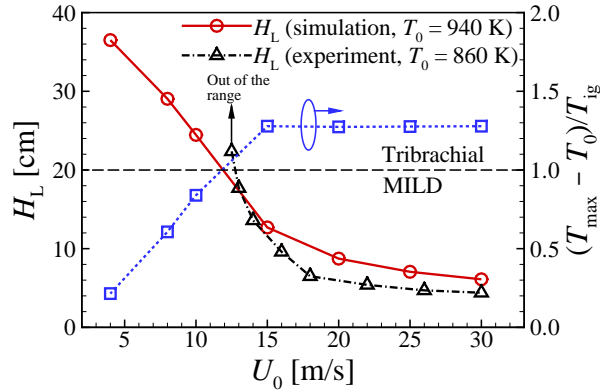


Figure 3.8: Variations of  $H_L$  (red) and  $(T_{\max} - T_0)/T_{\text{ig}}$  (blue) as a function of  $U_0$  for autoignited lifted flames under the LTHH condition ( $T_0 = 940$  K and  $R_H = 0.35$ ). The black dash-dotted line represents  $H_L$  variation of the corresponding experiments [2]

for  $(T_{\max} - T_0)/T_{\text{ig}} < 1$  with the flamebase being located at the centerline (the MILD combustion regime;  $U_0 = 4$  m/s), and (3) the transition regime between the tribrachial edge flame and MILD combustion regimes for  $(T_{\max} - T_0)/T_{\text{ig}} < 1$  with the flamebase being located radially outside the centerline (the transition regime;  $U_0 = 8 \sim 10$  m/s). Figure 3.9 shows the isocontours of heat release rate for  $U_0 = 4$  and  $15$  m/s under the LTHH condition, which represent the MILD combustion and tribrachial edge flame regimes, respectively. We can readily observe two different flame structures for different  $U_0$ ; in the MILD combustion regime ( $U_0 = 4$  m/s), the flame is relatively weak and blunt and the stoichiometric mixture fraction,  $\xi_{\text{st}}$ , isoline does not cross the flame region since it is overall very lean; while in the tribrachial edge flame regime ( $U_0 = 15$  m/s), it exhibits rich/lean premixed wings and a trailing nonpremixed flame which is along the  $\xi_{\text{st}}$  isoline.

Second, for all the lifted jet flames, important intermediate species including  $\text{CH}_2\text{O}$ ,  $\text{HO}_2$ , and  $\text{H}_2\text{O}_2$  are predominant in the upstream region from the flamebase, which indicates that autoignition affects the stabilization of the lifted flames. Moreover,  $H_L$  decreases significantly with increasing  $U_0$  in the MILD combustion/transition regimes, whereas the decreasing tendency of  $H_L$  is mitigated in the tribrachial edge flame regime. From these results, it can be hypothesized that the unusual decreasing behavior of  $H_L$  under the LTHH condition would be attributed to the characteristics of autoignition and flame structure depending on the hydrogen content in the fuel jet, which will be further

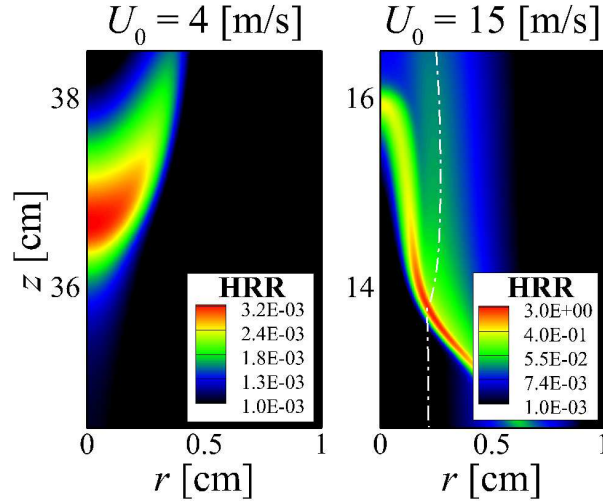


Figure 3.9: Isocontour of heat release rate ( $\text{J}/\text{mm}^3\text{s}$ ) for autoignited laminar lifted methane/hydrogen jet flames with  $U_0 = 4$  (left) and 15 m/s (right) under the LTHH condition. The dash-dotted line represents the stoichiometric mixture fraction isoline,  $\xi_{st}$ .

discussed later.

Note that under the LTHH condition, the flamebase is defined as the most upstream point of  $Y_{\text{OH}} = 2.3 \times 10^{-4}$  isoline. For the MILD combustion regime, however, we cannot define the flamebase using such definition because the lifted flames with MILD combustion would not exhibit the conventional flame structure and  $Y_{\text{OH}}$  values remain below  $2.3 \times 10^{-4}$ . To avoid ambiguity in the flamebase definition, therefore, we adopt the chemical explosive mode analysis (CEMA) and define the flamebase as the most upstream point of  $\text{Re}(\lambda_e) = 0$  isoline, where  $\lambda_e$  is an eigenvalue of the Jacobian of the chemical source term in the discretized governing equations [30–32, 102]. In other words, a mixture with  $\text{Re}(\lambda_e) > 0$  is more apt to ignite while a mixture with  $\text{Re}(\lambda_e) < 0$  is already burned or fails to ignite. Therefore,  $\text{Re}(\lambda_e) = 0$  isoline can be used to discern between the burned and unburned mixtures in autoignition and delineate the flame front especially for the lean premixed fronts. For the tribrachial edge flame regime, the flamebase defined by  $Y_{\text{OH}} = 2.3 \times 10^{-4}$  is nearly identical to that by the CEMA. The chemical features of the lifted jet flames under the LTHH condition using CEMA will be addressed in Section 3.10.

### 3.7 Effect of Hydrogen on The Liftoff Characteristics

As mentioned above, Choi et al. [2] conjectured that the unusual decreasing behavior of  $H_L$  with increasing  $U_0$  might be attributed to the disparity in mass diffusivities between methane and hydrogen. This hypothesis was based on observation that  $H_L$  varies significantly at relatively-low jet velocities that provide enough flow time to amplify the differential diffusion effect on the stabilization of the laminar lifted jet flames. To test whether or not the high diffusive nature of hydrogen molecules induces the unusual decreasing  $H_L$  tendency, we performed additional numerical simulations by artificially changing the mass diffusivity of hydrogen molecule,  $D_{H_2}$ , to that of methane.

### 3.8 Effect of Hydrogen Mass Diffusivity on $H_L$

Figure 3.10 shows the isocontours of temperature and mass fractions of OH, CH<sub>2</sub>O, and H<sub>2</sub>O<sub>2</sub> of autoignited laminar lifted methane/hydrogen jet flames with the modified  $D_{H_2}$ . Contrary to the cases with the normal  $D_{H_2}$ ,  $H_L$  increases with increasing  $U_0$ , which clearly shows the effect of  $D_{H_2}$  on the liftoff characteristics of the lifted methane/hydrogen jet flames. Thus, it should be emphasized that the decreasing behavior of  $H_L$  is not due to chemical kinetics (or choice of kinetic mechanism as shown in Fig. 3.4) but due to physical aspects of differential diffusion.

To quantitatively compare the characteristics of the lifted jet flames with the normal and modified  $D_{H_2}$  under the LTHH condition,  $(T_{\max} - T_0)/T_{ig}$  together with  $H_L$  is shown in Fig. 3.11. While  $H_L$  show the opposite trends with increasing  $U_0$  for the normal and modified  $D_{H_2}$  cases, both  $(T_{\max} - T_0)/T_{ig}$  values increase monotonically from the MILD combustion regime to the transition regime. Since the tribrachial edge flame regime is not observed for cases with the modified  $D_{H_2}$  due to the limitation of the present computational domain, we performed additional simulations with higher  $U_0$  by extending the burner length to 100 cm. From the results (not shown here), we found that both  $H_L$  and  $(T_{\max} - T_0)/T_{ig}$  values increase monotonically with  $U_0$  and three different combustion regimes also exist for the modified  $D_{H_2}$  cases.

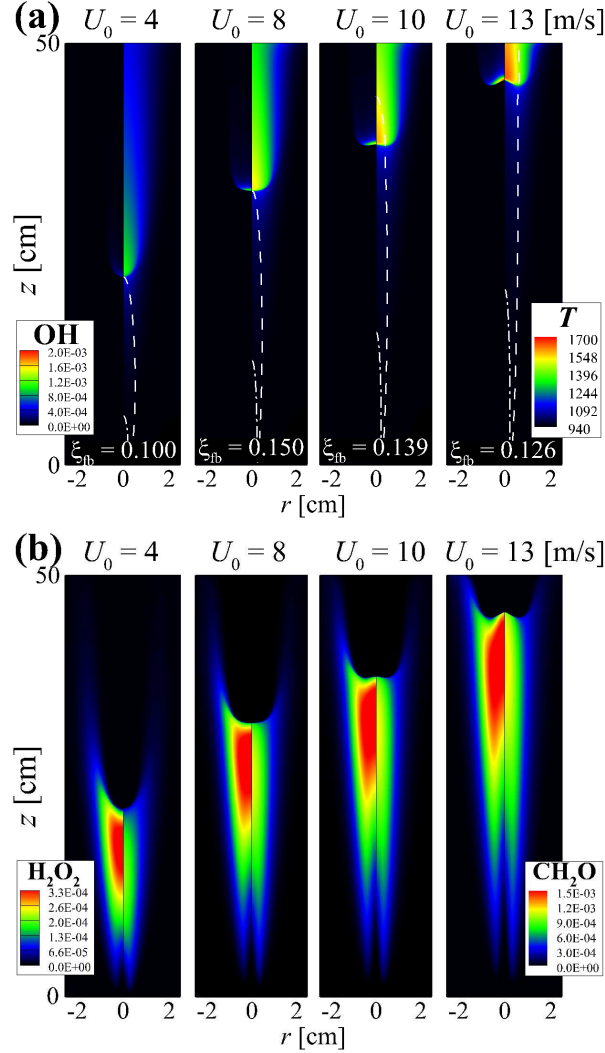


Figure 3.10: Isocontours of (a)  $Y_{OH}$  (left half) and  $T$  (right half) and (b)  $Y_{H_2O_2}$  (left half) and  $Y_{CH_2O}$  (right half) for autoignited laminar lifted methane/hydrogen jet flames with modified  $D_{H_2}$  for various fuel jet velocities  $U_0$  under the LTHH condition ( $T_0 = 940$  K and  $R_H = 0.35$ ). The dashed and dash-dotted lines in (a) represent the mixture fraction isoline passing through the flamebase,  $\xi_{fb}$ , and the stoichiometric mixture fraction isoline,  $\xi_{st} (= 0.378)$ , respectively.

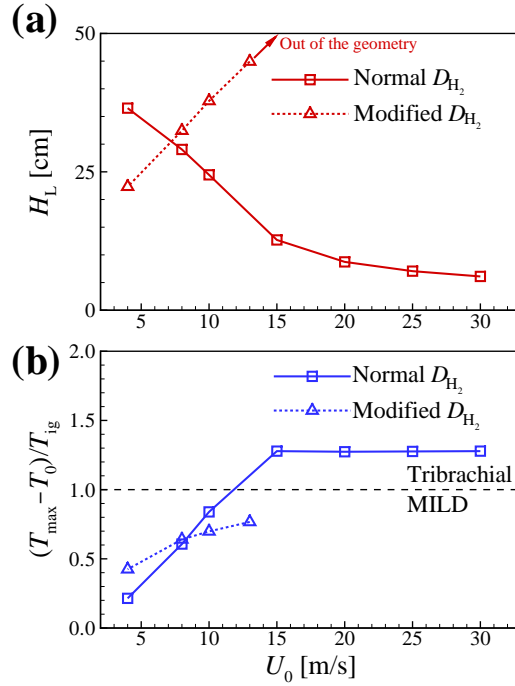


Figure 3.11: The variation of (a)  $H_L$  and (b)  $(T_{\max} - T_0)/T_{\text{ig}}$  for various fuel jet velocities with normal (solid line) and modified  $H_2$  diffusivity (dashed line) under the LTHH condition ( $T_0 = 940$  K and  $R_H = 0.35$ ).

To further identify how large  $D_{H_2}$  affects the mixture conditions upstream of the flamebase and resultant ignition characteristics, we evaluate local hydrogen ratio,  $R_H$ , along  $\xi_{\text{fb}}$  isoline for both normal and modified  $D_{H_2}$  cases. Here,  $R_H$  is evaluated based on the species information along  $\xi_{\text{fb}}$  isoline, for which all species are converted to the original reactants (i.e.  $\text{CH}_4$ ,  $\text{H}_2$ ,  $\text{O}_2$ , and  $\text{N}_2$ ) by applying the element conservation law. Therefore, we can effectively estimate the differential diffusion effect through  $R_H$ .

Figure 3.12 shows the profiles of  $R_H$  and  $T$  along the  $\xi_{\text{fb}}$  isoline for cases with the normal and modified  $D_{H_2}$  at different  $U_0$ . It is readily observed that for normal  $D_{H_2}$ , overall  $R_H$  increases with increasing  $U_0$ ; it exhibits a much greater value than the original  $R_H$  value ( $= 0.35$ ) of the fuel jet for relatively-large  $U_0$  while it decreases and even vanishes near the flamebase for relatively-small  $U_0$  cases. For modified  $D_{H_2}$ , however,  $R_H$  value remains nearly the same regardless of  $U_0$ . In general, a hydrocarbon/air mixture with high  $R_H$  autoignites faster than that with low  $R_H$  [103, 104], and as such,  $R_H$  profiles upstream of the flamebase for different  $D_{H_2}$  imply that for normal  $D_{H_2}$ , the ignition of

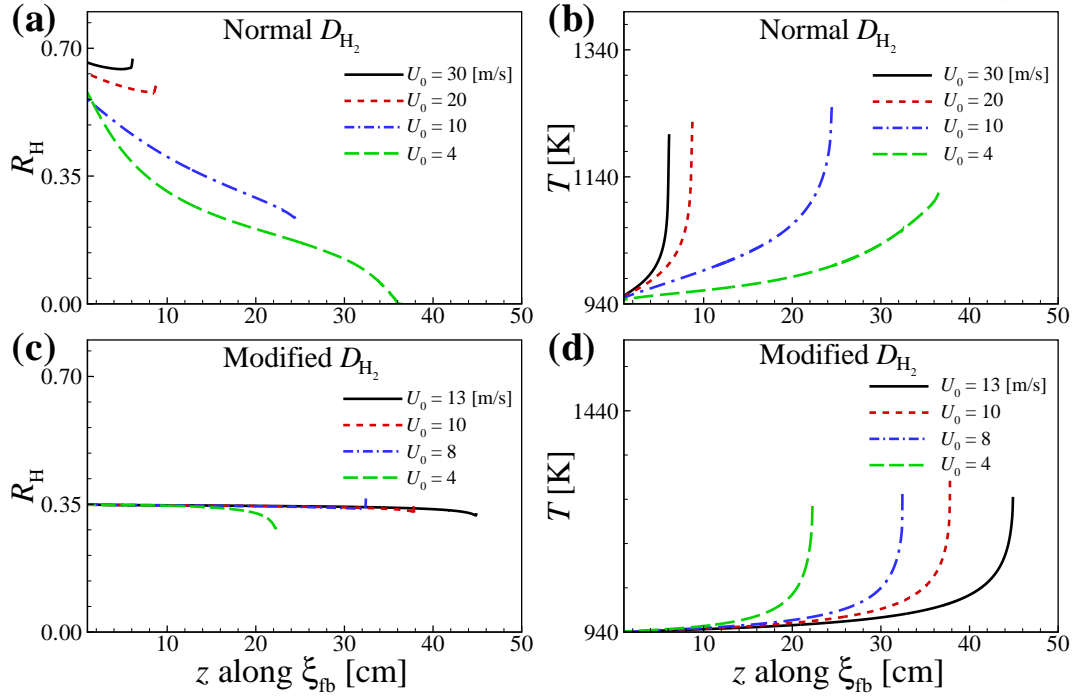


Figure 3.12: The profiles of  $R_H$  (left) and  $T$  (right) along the mixture fraction isline passing through the flamebase,  $\xi_{fb}$ , for various fuel jet velocities with normal (top) and modified (bottom)  $H_2$  diffusivities under the LTHH condition ( $T_0 = 940$  K and  $R_H = 0.35$ ).

fuel jet can be enhanced with increasing  $U_0$  while the effect of  $U_0$  on the ignition of the fuel jet becomes negligible for modified  $D_{H_2}$ . Consequently, the increase of local  $T$  by ignition is enhanced with increasing  $U_0$  for normal  $D_{H_2}$  (see Fig. 3.12b), whereas the profile of  $T$  is just spatially elongated downstream with increasing  $U_0$  for modified  $D_{H_2}$  (see Fig. 3.12d).

For heuristic argument purposes, a schematic of the  $H_L$  variation depending on  $D_{H_2}$  is shown in Fig. 3.13. For a given  $U_0$  represented by the dash-dotted line, the axial velocity along  $\xi_{fb}$  isline,  $U$ , is found to slightly increase due to local temperature increase by autoignition and/or the momentum diffusion of the fuel jet. However, the propagation speed of the leading edge of the lifted flame,  $S_e$ , can significantly increase along  $\xi_{fb}$  isline due to local temperature increase by ongoing autoignition. As such, the lifted flame is stabilized at the flamebase where  $S_e$  balances local flow velocity represented by  $U$  as illustrated in Fig. 3.13, which holds for both normal and modified  $D_{H_2}$  cases. However,

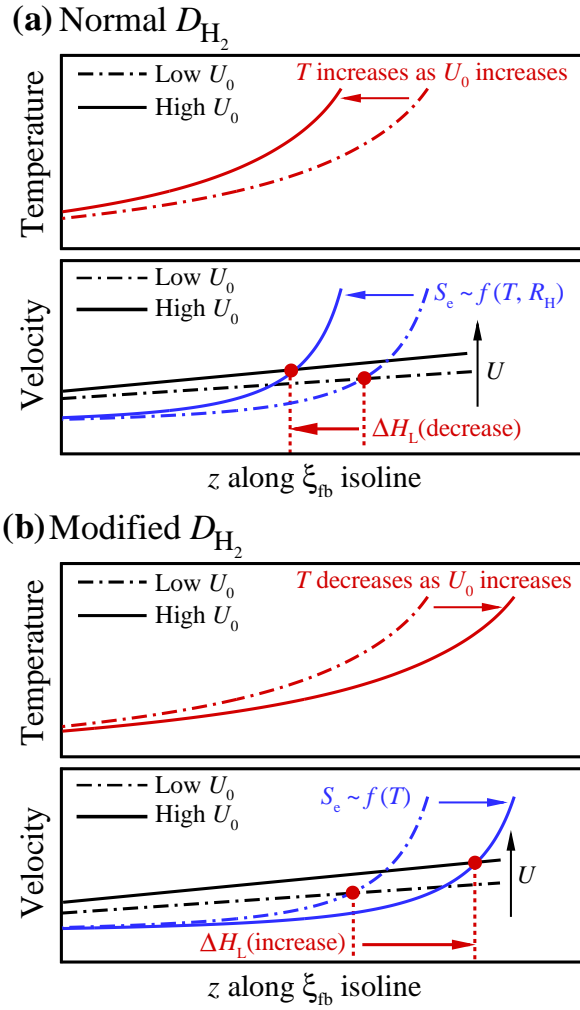


Figure 3.13: Schematic for the stabilization of autoignited laminar methane/hydrogen lifted flames with (a) normal and (b) modified  $H_2$  diffusivity.

$H_L$  can exhibit different behaviors depending on  $D_{H_2}$  when  $U_0$  is increased.

For high  $U_0$  with normal  $D_{H_2}$  represented by the solid line in Fig. 3.13a, even though overall  $U$  along  $\xi_{fb}$  isoline increases compared to that of low  $U_0$ , overall temperature profile and resultant  $S_e$  move towards upstream compared to those of low  $U_0$  due to spatially-enhanced ignition process. Moreover, higher  $R_H$  contributes to further increase of  $S_e$  for high  $U_0$ . As such, the lifted flame with high  $U_0$  is stabilized more upstream than that with low  $U_0$  as described in Fig. 3.13a.

For modified  $D_{H_2}$  cases, however, the ignition characteristics do not change much for high  $U_0$  such that the profiles of local temperature and resultant  $S_e$  are spatially elongated as shown in Figs. 3.12 and 3.13b. Therefore, the lifted flame with high  $U_0$

is stabilized more downstream than that with low  $U_0$  as illustrated in Fig. 3.13b. In summary, the increasing/decreasing  $H_L$  tendency for autoignited laminar lifted flames is primarily attributed to the ignition characteristics that affect local temperature and resultant  $S_e$  along the  $\xi_{fb}$  isoline.

### 3.9 Effect of Hydrogen on The Lifted Flame Stabilization

In this section, we elucidate how the high diffusive nature of hydrogen molecules affects the stabilization of the autoignited laminar lifted methane/hydrogen flames. First, we perform the transport budget analysis along the mixture fraction isoline passing through the flamebase,  $\xi_{fb}$ , as in previous studies [43, 105, 106]. In the present study, hydroxyl (OH) is adopted for the budget analysis since it is often used as a flame marker [71, 73, 107]. In a steady state, the convection (**C**), diffusion (**D**), and chemical reaction (**R**) terms in the transport equation of a species balance one another. To take into account the two-dimensional diffusion process of the present simulations, **D** is decomposed into parallel **D<sub>x</sub>** and perpendicular **D<sub>y</sub>** to the  $\xi_{fb}$  isoline, which are due to flame back diffusion and transverse stratification, respectively [106, 108]. In the reaction zone of a typical premixed flame, **R** mainly balances **D<sub>x</sub>** while **C** is negligible. In an inhomogeneous autoignition process, however, **R** balances **C** and **D<sub>y</sub>** with negligible **D<sub>x</sub>**.

Figure 3.14 shows the profiles of **C**, **D<sub>x</sub>**, **D<sub>y</sub>**, and **R** along the  $\xi_{fb}$  isoline for  $U_0 = 4, 10,$  and  $30$  m/s under the LTHH condition, each of which represents the MILD combustion, transition, and tribrachial edge flame regimes, respectively. For  $U_0 = 4$  m/s case, **R** mainly balances **C** and **D<sub>y</sub>** while **D<sub>x</sub>** is negligible, which indicates that the lifted flame with  $U_0 = 4$  m/s in the MILD combustion regime is primarily stabilized by inhomogeneous autoignition. For  $U_0 = 10$  and  $30$  m/s cases, the contribution of **D<sub>x</sub>** to the transport budget increases compared to that of  $U_0 = 4$  m/s, suggesting that the effect of flame propagation on the flame stabilization is no longer negligible. These results imply that the lifted flames with high  $U_0$  would be stabilized by the effects of



both autoignition and flame propagation, or autoignition-assisted flame propagation as discussed in [106, 109–111].

In addition to the species transport budget analysis, we also perform autoignition index,  $AI$ , analysis to further identify the stabilization mechanism of the autoignited laminar lifted methane/hydrogen jet flames. Schulz et al. [112] proposed  $AI$  as a criterion to distinguish autoignition and flame propagation of a lifted methane/air jet flame.  $AI$  was derived based on observation that the dominant  $\text{HO}_2$  consumption reaction changes depending on the stabilization mechanism;  $\text{HO}_2 + \text{H} \rightarrow \text{OH} + \text{OH}$  (R10) becomes predominant for the flame propagation mode and  $\text{HO}_2 + \text{OH} \rightarrow \text{H}_2\text{O} + \text{O}_2$  (R14–15) overwhelms R10 for the autoignition mode.  $AI$  is, therefore, defined as:

$$AI = \left| \frac{\dot{\omega}_{\text{HO}_2}^{(\text{R14-15})}}{\dot{\omega}_{\text{HO}_2}^{(\text{R14-15})} + \dot{\omega}_{\text{HO}_2}^{(\text{R10})}} \right|, \quad (3.1)$$

where  $\dot{\omega}_{\text{HO}_2}$  represent  $\text{HO}_2$  consumption rate. As such, a higher/lower  $AI$  value implies that a lifted jet flame is primarily stabilized by autoignition/flame propagation. Figure 3.15 shows the profiles of  $AI$  along the  $\xi_{\text{fb}}$  isoline for cases with  $U_0 = 4, 10,$  and  $30$  m/s under the LTHH condition. For  $U_0 = 30$  m/s case that represents a tribrachial edge flame, R10 and R14–15 balance each other at the flamebase and thus  $AI \approx 0.5$ . As  $U_0$  decreases, the relative contribution of R14–15 to the overall  $\dot{\omega}_{\text{HO}_2}$  increases, leading to the increase of  $AI$ . These results also verify that autoignition-assisted flame propagation (or transition from flame propagation to autoignition) is the main stabilization mechanism for the lifted jet flames and the effect of autoignition increases with decreasing  $U_0$ .

Both the transport budget and autoignition index analyses can identify flame propagation or autoignition mode of a lifted jet flame but they may not be suitable for distinguishing autoignition-assisted flame propagation and autoignition. For instance, although  $AI \approx 0.5$  and **C-D-R** balance imply the autoignition-assisted flame propagation, there still exists uncertainty about a threshold value to discern autoignition and autoignition-assisted flame propagation modes. When a lifted jet flame is stabilized either by autoignition or autoignition-assisted flame propagation, the degree of temperature increase and intermediate species build-up upstream of its flamebase can significantly vary depending on the flow condition as shown Fig. 3.7. This implies that the propa-

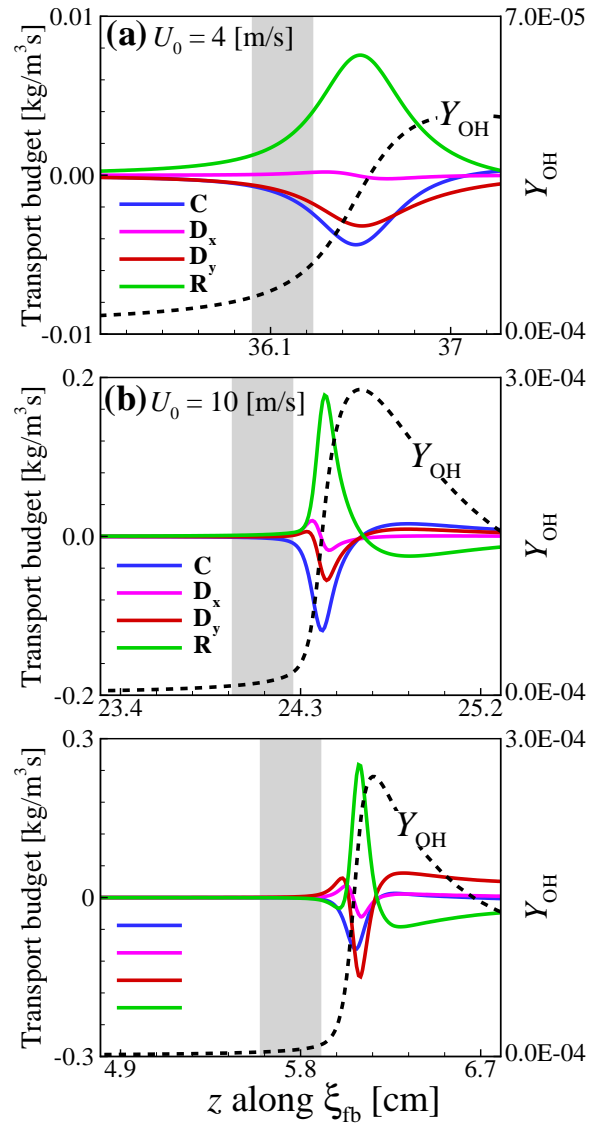


Figure 3.14: Profiles of convection (blue), diffusion in parallel (pink) and normal (red) direction, and chemical reaction (green) terms along the mixture fraction isoline passing through the flamebase,  $\xi_{fb}$ , for (a)  $U_0 = 4$ , (b) 10, and (c) 30 m/s.

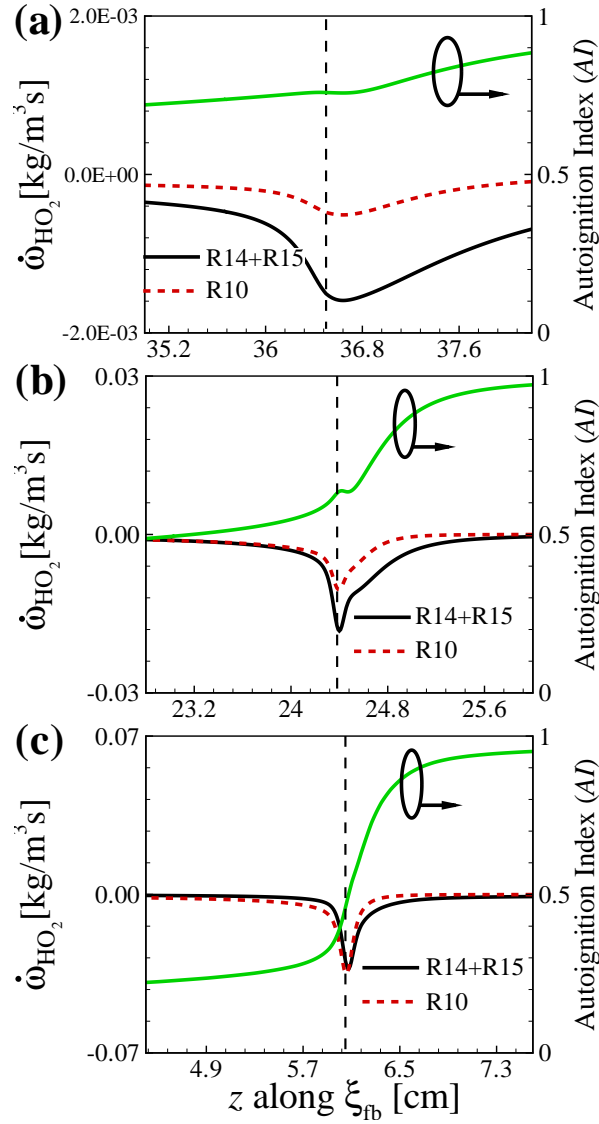


Figure 3.15: Profiles of R14–15 (black) and R10 (red) with autoignition index (green) along the mixture fraction iseline passing through the flamebase,  $\xi_{\text{fb}}$ , for (a)  $U_0 = 4$ , (b) 10, and (c) 30 m/s. The vertical dashed lines represent the flamebase location.

gation speed of the flamebase of a lifted flame,  $S_e$ , becomes comparable to/significantly greater than corresponding laminar flame speed,  $S_L$ , if the lifted flame is stabilized by autoignition-assisted flame propagation/autoignition mode [109, 111, 113].

To further identify the stabilization mechanism of the lifted flames, therefore, we evaluate  $S_e$  for various  $U_0$  under the LTHH condition and then compare  $S_e$  with corresponding  $S_L$ . Here,  $S_L$  is evaluated based on temperature and species information upstream of the flamebase to incorporate the effect of autoignition. For this purpose,  $S_e$  is obtained through the density-weight displacement speed,  $S_d^*$ , which has been used to evaluate the propagation speed of reaction fronts in many previous studies [71, 73, 114–120].  $S_d^*$  is defined by:

$$S_d^* = \frac{1}{\rho_u |\nabla Y_k|} (\omega_k - \frac{\partial}{\partial x_j} (\rho Y_k V_{j,k})), \quad (3.2)$$

where  $Y_k$  is the mass fraction,  $V_{j,k}$  the diffusion velocity in the  $j$ -direction,  $\omega_k$  the net production rate of species  $k$ , and  $\rho_u$  is the density of the unburnt mixture.  $S_d^*$  is evaluated at the most upstream point of  $Y_{OH} = 2.3 \times 10^{-4}$  isoline defined as the flamebase.

In the present study,  $S_L$  upstream of the flamebase is estimated from transient 1-D reactive simulations as in [43, 49, 118]. The initial mixture conditions for the 1-D simulations were obtained from those at several locations upstream of the flamebase along the  $\xi_{fb}$  isoline as highlighted in grey in Fig. 3.14. The simulations were then initialized with a high-temperature ignition source such that a combustion wave develops from the source and propagates into the initial reactive mixture ahead of it. The reactive mixture upstream of the combustion wave does not autoignite until  $\tau_{ig}^0$ , and hence, the propagation speed of the combustion wave,  $S_d^*$ , can be considered as the laminar burning velocity,  $S_L$ , similar to the diffusive limit found in previous studies [43, 49, 118]. Note that in the present study, it is not straightforward to precisely determine  $S_L$  values because autoignition process is underway producing heat and radicals. To reasonably estimate  $S_L$ , therefore, we evaluate it based on the local mixture components and temperature upstream of the flamebase, for which species components are converted to the original reactants at the inlets (i.e.  $CH_4$ ,  $H_2$ ,  $O_2$ , and  $N_2$ ) as for  $R_H$  calculation. Then, we evaluate  $S_L$  of the unburned mixture at the local temperature. Although this method

cannot evaluate  $S_L$  perfectly, it can provide rough estimate of  $S_L$  values.

Figure 3.16 shows  $S_L$  and  $S_e/S_L$  at several locations along the  $\xi_{fb}$  isoline upstream of the flamebase for  $U_0 = 4, 10, \text{ and } 30$  m/s under the LTHH condition. Note that  $S_e$  at the flamebase is found to be 1.45, 1.81, and 1.25 m/s for  $U_0 = 4, 10, \text{ and } 30$  m/s, respectively. As mentioned above,  $U_0 = 4, 10, \text{ and } 30$  m/s cases represent the MILD combustion, transition, and tribrachial edge flame regimes, respectively. Two points are to be noted. First, it is readily observed that  $S_L$  increases as the  $S_L$  measuring point approaches the flamebase, which verifies that  $S_e$  can increase along the  $\xi_{fb}$  isoline upstream of the flamebase as illustrated in Fig. 3.13. Second, it is also observed that for  $U_0 = 10$  and 30 m/s cases,  $S_e/S_L$  is close to unity even though the former/latter is slightly larger/smaller than unity, which implies that the autoignited lifted jet flames of the transition and tribrachial edge flame regimes can be stabilized by the flame propagation mode. For these cases, however,  $S_e$  is considerably greater than the corresponding laminar burning velocity under non-autoignitive conditions or low-temperature conditions such that the lifted jet flames are stabilized by the autoignition-assisted flame propagation mode for which the edge flame speed of the lifted jet flames is significantly enhanced by temperature increase induced by autoignition upstream of the flamebase. For  $U_0 = 4$  m/s case, however,  $S_e/S_L$  is an order of magnitude greater than unity, which indicates that the lifted jet flames with relatively-low  $U_0$  are primarily stabilized by autoignition. These results are consistent with those of species transport budget and autoignition index analyses.

It is of interest to note that the stabilization mechanism of the present autoignited lifted methane/hydrogen jet flames seems to be contrary to those of previous studies [106,108,109]: the role of flame propagation on the flame stabilization enhances/mitigates with increasing  $U_0$  for the present/previous studies. As discussed above, we can determine the stabilization mechanism of a lifted flame based on the relative magnitude of the propagation speed of the flamebase,  $S_e$ , to the laminar burning velocity of a mixture upstream of the flamebase,  $S_L$ : i.e., a lifted flame is stabilized by flame propagation/autoignition when  $S_e$  is comparable to/significantly greater than  $S_L$ . In previous studies [106,108,109], single component fuels (i.e., DME, *n*-heptane, and ethanol) were used such that  $S_L$  of a

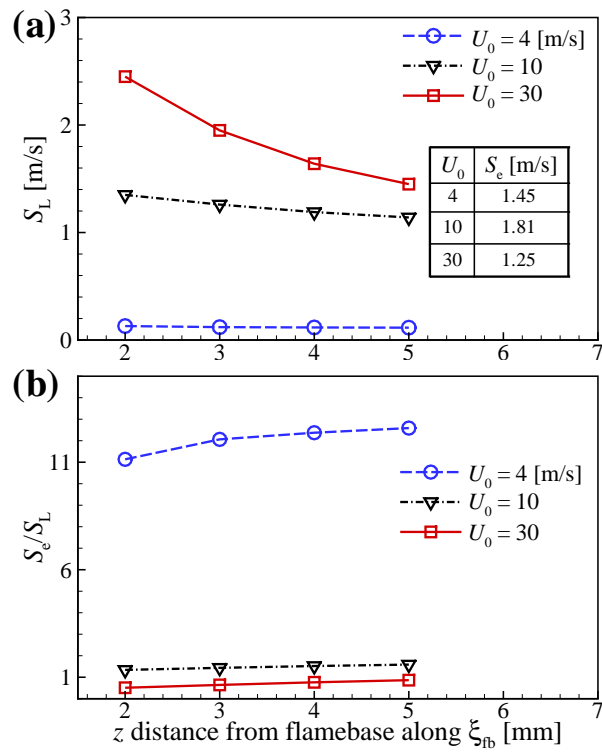


Figure 3.16: Variation of (a)  $S_L$  and (b)  $S_e/S_L$  at 2, 3, 4, and 5 mm upstream of the flamebase along the mixture fraction isoline passing through the flamebase,  $\xi_{fb}$ , for  $U_0 = 4, 10,$  and  $30$  m/s cases.

lifted flame does not change with  $U_0$ . At relatively-low  $U_0$ , therefore, a lifted flame can be stabilized by flame propagation because  $S_e$  ( $\sim S_L$ ) can balance relatively-low local flow velocity,  $U$ :  $S_L \sim S_e = U$ . However, a lifted flame can be stabilized by autoignition at relatively-high  $U_0$  where only high  $S_e$  induced by autoignition can balance local flow velocity that is way high compared to  $S_L$ :  $S_e = U \gg S_L$ .

However, in the present study we adopted a binary component fuel of  $\text{CH}_4$  and  $\text{H}_2$  highly diluted by  $\text{N}_2$  (i.e.,  $X_{\text{F},0} = 0.2$ ), for which the diffusion coefficients are significantly different between them. The laminar burning velocity and ignition delay of such binary fuel significantly vary depending on its compositions, and as such,  $S_L$  of a lifted flame changes significantly with  $U_0$  due to the differential diffusion effect (see Fig. 3.16a). At relatively-high  $U_0$ , large  $R_{\text{H}}$  at the flamebase enhances  $S_L$  such that a lifted flame can be stabilized by flame propagation, which is actually autoignition-assisted flame propagation as discussed above:  $S_L \sim S_e = U$ . At relatively-low  $U_0$ , however,  $R_{\text{H}}$  nearly vanishes and the entire jet becomes very lean near the flamebase such that  $S_L$  exhibits much lower value than local flow velocity:  $S_L \ll U$ . Then, a lifted flame with low  $U_0$  can be stabilized only by autoignition for which relatively-high  $S_e$  induced by autoignition can balance local flow velocity:  $S_e = U \gg S_L$ .

### 3.10 Ignition Characteristics: CEMA

To further elucidate the spatial ignition and flame stabilization characteristics of the lifted flames, we perform chemical explosive mode analysis (CEMA). CEMA has been successfully adopted to systematically identify key species and reactions for premixed/non-premixed flames and ignition/extinction processes in laminar/turbulent lifted jet flames in heated coflows [30, 31, 73, 108, 121], turbulent reacting jet flames in cross flows [74, 75], and ignition of hydrocarbon fuel/air mixtures under HCCI conditions [32, 51, 83, 102].

As mentioned above, the Jacobian of the chemical source term of the discretized conservation equations for a chemically-reacting system has the chemical information of local mixtures, and hence, we can determine their chemical characteristics using the Jacobian [30–32]. To identify the chemical feature in CEMA, a chemical mode is defined

as an eigenmode of the Jacobian, which is associated with an eigenvalue,  $\lambda_e$ , and a corresponding pair of the left and right eigenvectors,  $\mathbf{a}_e$  and  $\mathbf{b}_e$ . Chemical explosive mode (CEM) is a chemical mode for which the real part of eigenvalue is positive,  $\text{Re}(\lambda_e) > 0$ . From CEMA, the critical chemical kinetic processes occurring in the autoignited laminar lifted flames can be identified by evaluating explosive index (**EI**) and participation index (**PI**) of local mixtures. **EI** and **PI** are defined as [31, 32, 102]:

$$\mathbf{EI} = \frac{|\mathbf{a}_e \otimes \mathbf{b}_e^T|}{\sum |\mathbf{a}_e \otimes \mathbf{b}_e^T|}, \quad (3.3)$$

$$\mathbf{PI} = \frac{|(\mathbf{b}_e \cdot \mathbf{S}) \otimes \mathbf{R}|}{\sum |(\mathbf{b}_e \cdot \mathbf{S}) \otimes \mathbf{R}|}, \quad (3.4)$$

where  $\mathbf{S}$  and  $\mathbf{R}$  represent the stoichiometric coefficient matrix and the vector of the net rates for reactions, respectively. The symbol  $\otimes$  denotes the element-wise multiplication of two vectors. **EI** and **PI** indicate the normalized contribution of each variable and reaction to a CEM, respectively, and as such, key species and reactions to ignition near the flamebase can be elucidated by evaluating EI and PI values.

Figure 3.17 shows the EI isocontours of several important variables for the lifted flames in three different regimes (i.e.  $U_0 = 4, 10,$  and  $30$  m/s) under the LTHH condition. Heat release rate is also presented in the figure to show the flame location. Two points are to be noted from the figure. First, for all regimes the most important EI variable upstream of the flamebase is temperature while  $\text{CH}_4$ ,  $\text{CH}_2\text{O}$ ,  $\text{H}_2\text{O}_2$  and  $\text{H}_2$  also contribute to the CEM upstream of the flamebase, showing a general sequence of autoignition of methane/air or hydrogen/air mixture [70]. Second, for the MILD combustion regime ( $U_0 = 4$  m/s) the contribution of  $\text{CH}_4$  to the CEM becomes significant right upstream of the flamebase. For the tribrachial edge flame regime ( $U_0 = 30$  m/s), however, the contribution of  $\text{H}_2$  to the CEM becomes important. These results substantiate that hydrogen molecules with large mass diffusivity play a critical role in stabilizing the lifted flame in the tribrachial edge flame regime while the ignition of methane is critical to the MILD combustion.

To further identify the chemical characteristics of the lifted flames in different regimes, the contribution of each chemical reaction to the CEM, or the PI isocontours of important reactions are shown in Fig. 3.18. Although the chemical features of the lifted flames have been briefly investigated through the EI analysis, we can further examine which reaction



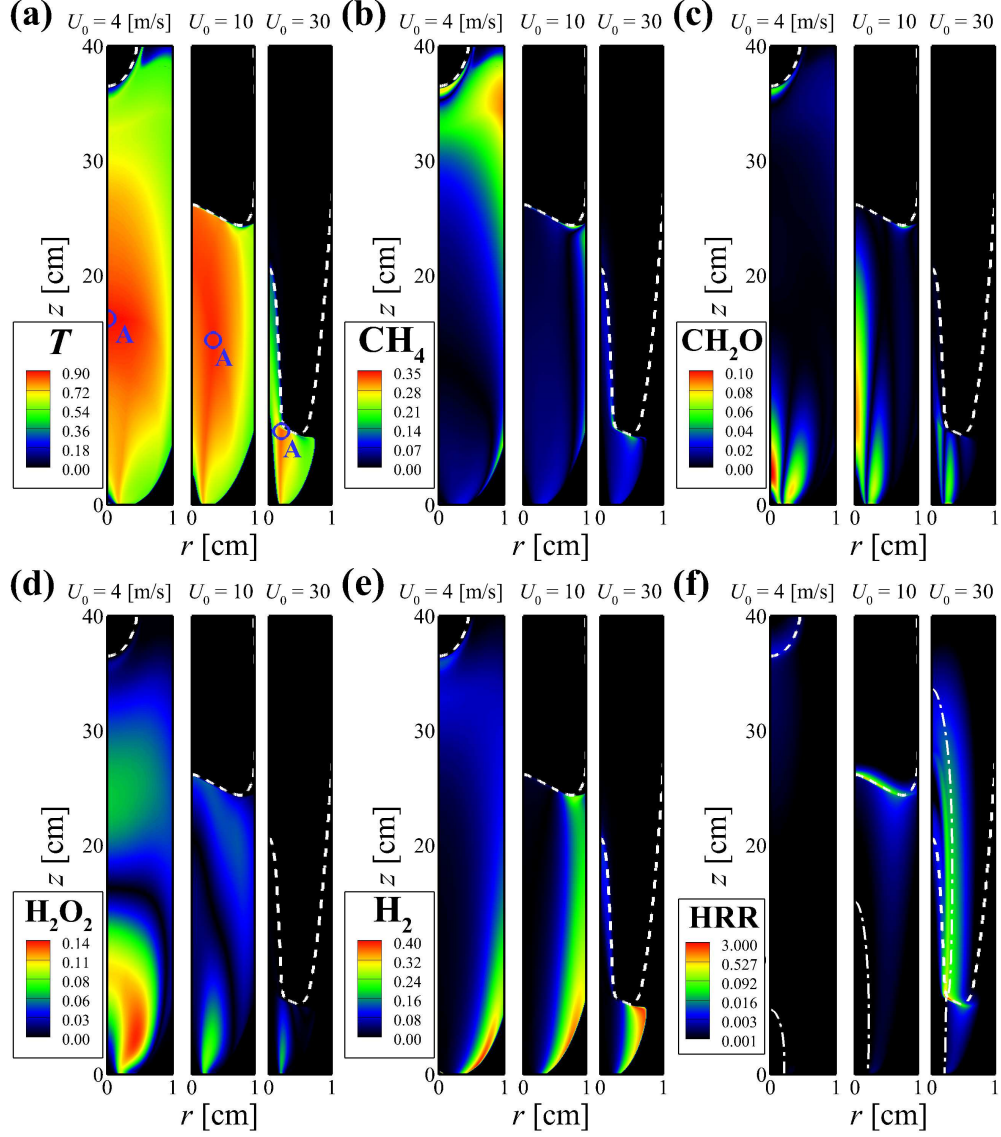


Figure 3.17: Isocontours of EI of (a)  $T$ , (b)  $\text{CH}_4$ , (c)  $\text{CH}_2\text{O}$ , (d)  $\text{H}_2\text{O}_2$ , and (e)  $\text{H}_2$ , and (f) heat release rate ( $\text{J}/\text{mm}^3\text{s}$ ) for autoignited laminar lifted methane/hydrogen jet flames with  $U_0 = 4, 10, \text{ and } 30$  m/s under the LTHH condition. The dashed line represents an isoline of  $\text{Re}(\lambda_e) = 0$  and the dash-dotted in (f) denotes the stoichiometric mixture fraction isoline,  $\xi_{\text{st}}$ .

affects the CEM through the PI analysis. For the MILD combustion regime ( $U_0 = 4$  m/s), we can readily observe a general sequence of autoignition of methane/air mixture upstream of the flamebase [70]: after the H abstraction from  $\text{CH}_4$  near the fuel nozzle (not shown), the conversion of  $\text{CH}_3$  to  $\text{CH}_3\text{O}/\text{CH}_2\text{O}$  to  $\text{HCO}$  occurs in sequence through  $\text{CH}_3 + (\text{O}, \text{O}_2, \text{HO}_2, \text{O}_2) \rightarrow (\text{CH}_2\text{O} + \text{H}, \text{CH}_2\text{O} + \text{OH}, \text{CH}_3\text{O} + \text{OH}, \text{CH}_3\text{O} + \text{O})$  (R49, R51–53),  $\text{CH}_3\text{O} + (\text{O}_2, \text{M}) \rightarrow \text{CH}_2\text{O} + (\text{HO}_2, \text{H} + \text{M})$  (R78, R79), and  $\text{CH}_2\text{O} + (\text{H}, \text{O}, \text{OH}, \text{HO}_2) \rightarrow \text{HCO} + (\text{H}_2, \text{OH}, \text{H}_2\text{O}, \text{H}_2\text{O}_2)$  (R36–38, R40) as shown in Figs. 3.18a and b. In addition,  $\text{H}_2\text{O}_2 + \text{M} \rightarrow \text{OH} + \text{OH} + \text{M}$  (–R16) occurs more actively as a part of radical growth for the methane oxidation (see Fig. 3.18c). The final CO conversion to  $\text{CO}_2$  occurs as the main heat release step right after the conversion of  $\text{HCO}$  to  $\text{CO}$  occurring just upstream of the flame (not shown).

For the tribrachial edge flame regime ( $U_0 = 30$  m/s), however, we can identify from Figs. 3.18d–f that the contribution of hydrogen oxidation reactions to the CEM becomes significant upstream of the flamebase: the recombination reaction of  $\text{H} + \text{O}_2 + \text{M} \rightarrow \text{HO}_2 + \text{M}$  (R9) competes with the chain branching reaction of  $\text{H} + \text{O}_2 \rightarrow \text{O} + \text{OH}$  (R1) far upstream of the flamebase; however, the latter becomes more important than the former as it comes to the flamebase; especially, the contribution of the chain branching reaction (R1) and the hydrogen heat release reaction of  $\text{H}_2 + \text{OH} \rightarrow \text{H} + \text{H}_2\text{O}$  (R3) become dominant right upstream of the flamebase. In summary, the PI analysis identifies the occurrence of distinct methane and hydrogen oxidation processes upstream of the flamebases for different regimes, which clearly shows that the hydrogen effect on the unusual decreasing  $H_L$  behavior with increasing  $U_0$  is due to the hydrogen chemistry, which is originally from the fast diffusion of hydrogen molecules from the fuel jet.

To quantitatively identify the ignition characteristics of the lifted flames, PI values of important reactions at Point A, delineated in Fig. 3.17a, are shown in Fig. 3.19. Point A indicates a location where thermal ignition process attains its peak (i.e. the maximum  $\text{EI}(T)$  point in the domain). By comparing PI values of important reactions at this point, we identify the relative contribution of methane and hydrogen oxidation to the CEM in the different regimes. It is readily observed from PI values at Point A that the contribution of the methane oxidation to the CEM represented by the conversion of

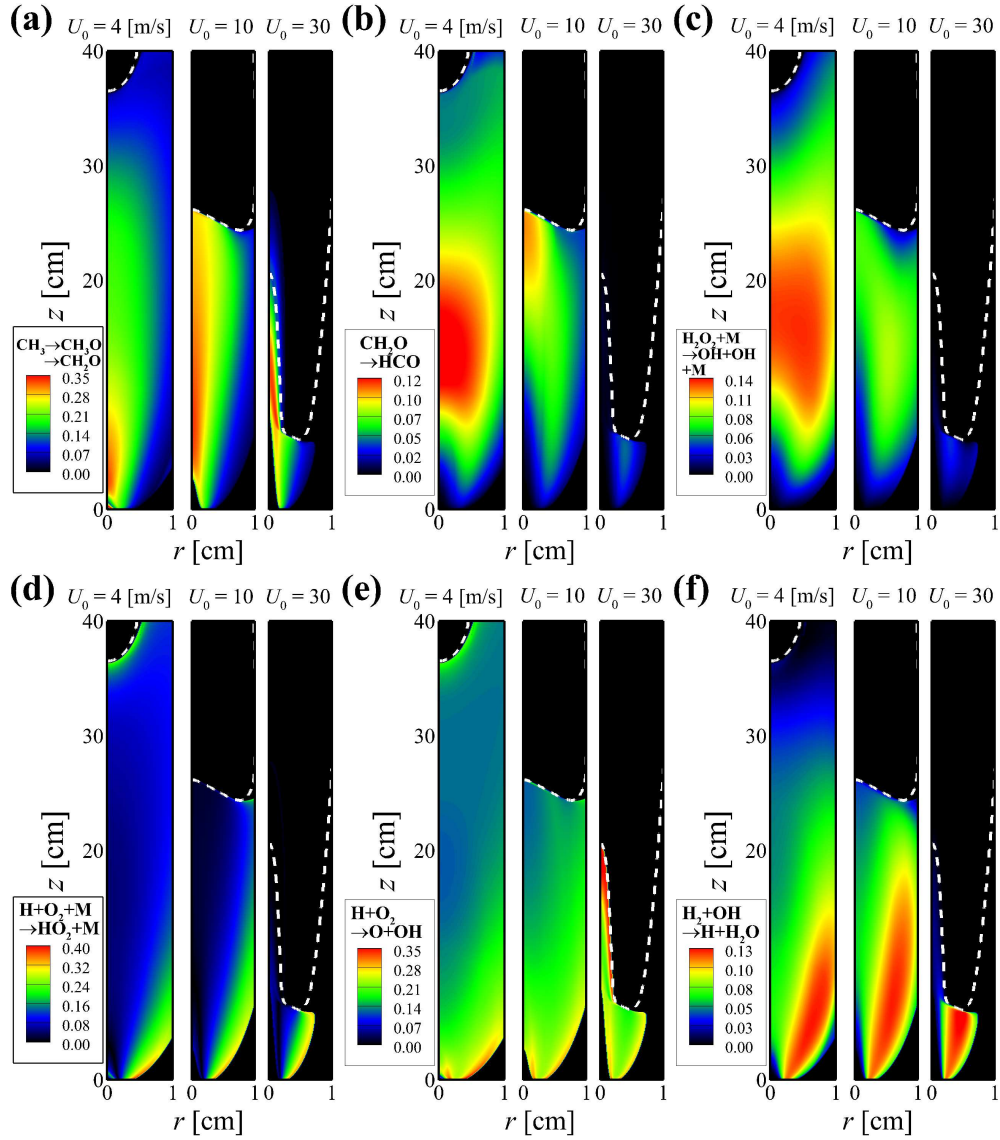


Figure 3.18: Isocontours of PI of (a) reactions of  $\text{CH}_3$  conversion to  $\text{CH}_2\text{O}$  and  $\text{CH}_3\text{O}$ , (b)  $\text{CH}_2\text{O}$  conversion to  $\text{HCO}$ , (c)  $\text{H}_2\text{O}_2 + \text{M} \rightarrow \text{OH} + \text{OH} + \text{M}$  ( $-\text{R16}$ ), (d)  $\text{H} + \text{O}_2 + \text{M} \rightarrow \text{HO}_2 + \text{M}$  (R9), (e)  $\text{H} + \text{O}_2 \rightarrow \text{O} + \text{OH}$  (R1), and (f)  $\text{H}_2 + \text{OH} \rightarrow \text{H} + \text{H}_2\text{O}$  (R3) for autoignited laminar lifted methane/hydrogen jet flames for cases with  $U_0 = 4, 10,$  and  $30$  m/s. The dashed line represents an isoline of  $\text{Re}(\lambda_e) = 0$ .

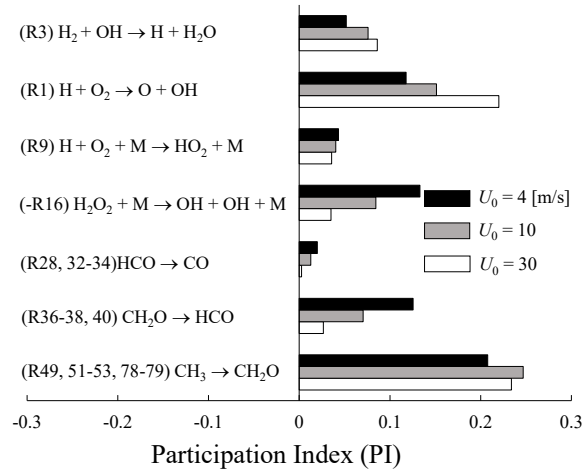


Figure 3.19: PIs of selected reactions at the sampled point, Point A. Location of Point A is specified in Fig. 3.17a

$\text{CH}_2\text{O}$  to  $\text{HCO}$  (R36–38 and R40) or radical growth (–R16) becomes large for the MILD combustion regime ( $U_0 = 4$  m/s).

However, the overall contribution of the hydrogen oxidation to the CEM increases with increasing  $U_0$ ; the chain branching reaction of hydrogen oxidation (R1) dominates over the recombination reactions (R9) for all  $U_0$  cases and the difference between R1 and R9 becomes more significant for cases with large  $U_0$ . A similar trend is also observed for the heat release reaction of hydrogen (R3) at Point A. These results imply that the hydrogen oxidation chemistry is more enhanced upstream of the lifted jet flames with increasing  $U_0$  due to higher  $\text{H}_2$  concentration caused by its fast diffusion, which leads to advancing the oxidation of the methane/hydrogen jet. In summary, the contribution of the hydrogen oxidation reactions to the CEM for the tribrachial edge flame regime is relatively larger than that for the MILD combustion regime, and as such, the oxidation of the fuel jet for the tribrachial edge flame regime occurs faster than that for the MILD combustion regime.

### 3.11 Conclusions

The characteristics of autoignited laminar lifted methane/hydrogen jet flames in heated coflow air were numerically investigated using laminarSMOKE code with a 57-species detailed chemical kinetic mechanism of methane oxidation. The detailed numerical simulations were performed for various fuel jet velocities under the HTLH and LTHH conditions. The numerical simulations captured qualitatively different lifted flame behaviors under the HTLH and LTHH conditions, in agreement with those in experiments. To identify the effect of differential diffusion on the unusual  $H_L$  behavior under the LTHH condition, additional numerical simulations with modified  $D_{H_2}$  were also carried out. The following results were obtained from the simulations together with the transport budget, autoignition index, displacement speed, and chemical explosive mode analyses.

1. Considering the flame structure and  $(T_{\max} - T_0)/T_{\text{ig}}$ , we categorized the autoignited laminar lifted methane/hydrogen jet flames under the LTHH condition into three different combustion regimes: the MILD combustion, transition, and tribrachial edge flame regimes.
2. From the simulations with normal and modified  $D_{H_2}$ , it was verified that the high diffusive nature of hydrogen molecules or the differential diffusion between methane and hydrogen is primarily attributed to the unusual decreasing  $H_L$  behavior with increasing  $U_0$  under the LTHH condition.
3. In the MILD combustion regime under the LTHH condition, local hydrogen ratio,  $R_H$ , along the  $\xi_{\text{fb}}$  isoline decreases because hydrogen molecules in the fuel jet have enough time to diffuse out from the center, and hence, local temperature increase by autoignition is relatively reduced compared to that in the tribrachial edge flame regime. On the other hand, in the tribrachial edge flame regime, the flamebase locates radially outside and more hydrogen molecules can diffuse into the flamebase. Therefore,  $R_H$  along the  $\xi_{\text{fb}}$  isoline increases and local temperature increase by autoignition is relatively enhanced. Such  $R_H$  characteristics lead to the decrease of  $H_L$  with increasing  $U_0$ .

4. The species transport budget, autoignition index, and displacement speed analyses revealed that the stabilization of the autoignited lifted methane/hydrogen jet flames is affected by both autoignition and flame propagation. The role of flame propagation on their stabilization increases with increasing  $U_0$  due to the  $R_H$  characteristics depending on  $U_0$  and the flamebase locations: a lifted flame in the MILD combustion regime is primarily stabilized by autoignition while it in the tribrachial edge flame regime is stabilized by autoignition-assisted flame propagation.
5. The chemical explosive mode analysis identified the ignition process upstream of the flamebase and the difference between the tribrachial edge flame and MILD combustion regimes. In the tribrachial edge flame regime, the overall contribution of hydrogen-related reactions to the CEM becomes greater than that in the MILD combustion regime. Therefore, local temperature increase is relatively enhanced upstream of the flamebase in the tribrachial edge flame regime, leading to the decrease of  $H_L$ .

## Chapter IV

# Autoignited Laminar Lifted *n*-Heptane Jet Flames in Heated Coflow Air

### 4.1 Introduction

In previous experiments [24], a sudden jumping behavior of  $H_L$  with increasing  $U_0$  was observed under autoignitive condition (e.g.  $T_0 = 980$  K), at which a lifted flame is formed from an ignition kernel without any external ignition sources. To figure out the reason why such liftoff height behavior occurs, we carry out numerical simulations of autoignited laminar lifted *n*-heptane jet flames by varying  $T_0$ , and the liftoff height jumping behavior is captured at  $T_0 = 1020 \sim 1030$  K. Note that  $T_0$  in the simulations are slight larger than that in experiments (i.e. 980 K) and the liftoff height jumping behavior is captured with several  $T_0$  conditions from 1020 K to 1030 K. The characteristics of flame liftoff and flame structure are nearly identical to each other except for different  $H_L$  for each  $T_0$  case.

The following sections will show (1) the liftoff characteristics of laminar lifted *n*-heptane jet flames, especially the reason of the occurrence of the sudden jumping behavior of  $H_L$ , and (2) their flame stabilization and structure characteristics.

## 4.2 Numerical Methods

Numerical simulations of laminar lifted *n*-heptane nonpremixed jet flames in heated coflow air are performed in an axisymmetric coflow burner configuration, which has been adopted in previous numerical study [122]. The steady compressible Navier-Stokes, species continuity, and energy equations are solved using laminarSMOKE [89, 90]. For the detailed description of laminarSMOKE, readers are referred to [89, 90].

Computational domain is similar to that of the previous numerical study [122]. The domain size is 4.25 cm  $\times$  50 cm in the radial *r*- and the axial *z*-directions. The inner diameter and thickness of the fuel nozzle are 3.76 mm and 0.5 mm, respectively. To take into account the effect of the finite thickness of the fuel jet nozzle on the flow, 7 cm long fuel nozzle is added to the main computational domain, which protrudes 1 cm above the coflow air inlet as shown in Fig. 4.1. Note that the configuration of the computational domain is identical to those of previous experiments and simulations [23, 24].

The boundary conditions for autoignited laminar lifted *n*-heptane jet flames are identical to those for the previous autoignited laminar lifted methane/hydrogen jet flames [122]. The fuel inlet velocity is specified as that of a fully-developed pipe flow for which the mean velocity is  $U_0$ , and the coflow air velocity,  $U_C$ , is set to be 1.0 m/s. For both fuel and air inlets, constant inlet temperature,  $T_0$ , is specified. For the outlet, zero-gradient outflow boundary conditions are used. For all simulations, the pressure is atmospheric and the *n*-heptane fuel jet is diluted with nitrogen such that the fuel mole fraction at the inlet,  $X_{F,0}$ , is 0.02. In the *r*-direction, a uniform grid space of 50  $\mu\text{m}$  is used for  $0 \leq r \leq 1.5$  cm to resolve the flame structure and a stretched grid is applied to the remaining domain. In the *z*-direction, the same uniform grid of 100  $\mu\text{m}$  is used. Thus, the current grid space of 100  $\mu\text{m}$  can resolve the flame thickness with approximately 20 grids, which is enough to resolve the flame structure and liftoff characteristics of autoignited laminar lifted *n*-heptane flames. No-slip and adiabatic boundary conditions are used for all the solid boundaries and symmetric boundary conditions are applied for  $r = 0$ . Note that the skeletal mechanism of *n*-heptane with 68 species [62] was used for the chemical reactions.



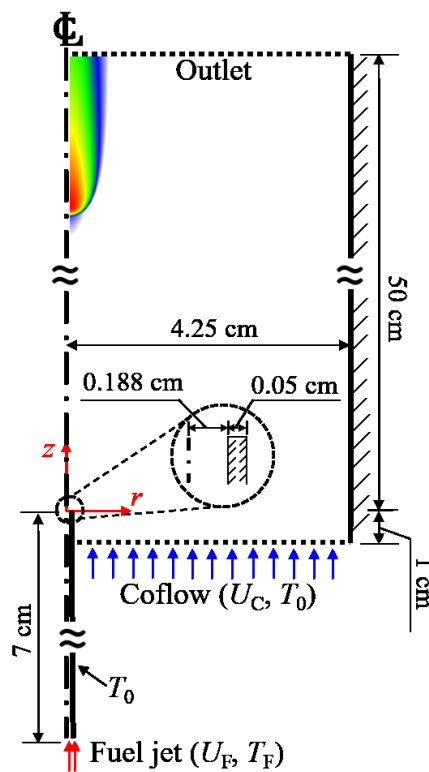


Figure 4.1: Schematic of the computational domain for simulations of autoignited laminar lifted *n*-heptane jet flames in heated coflow air.

### 4.3 Lifted Jet Flame Combustion Characteristics

Figure 4.3 shows  $H_L$  as a function of the jet velocity,  $U_0$ . The liftoff height jumping occurs between  $U_0 = 6.5$  and  $6.7$  m/s, which was captured at  $U_0 = 5$  m/s in the previous experiment [24]. Figure 4.2 shows the isocontours of temperature,  $Y_{OH}$ ,  $Y_{CH_2O}$ , and heat release rate (HRR) of laminar lifted *n*-heptane jet flames for several  $U_0$ . The dash dot lines represent the mixture fraction isoline passing through the stoichiometric mixture fraction isoline,  $\xi_{st}$  ( $= 0.494$ ), and the dashed line indicates flamebase mixture fraction for jumped condition (i.e.  $U_0 > 6.7$  m/s). In the present study,  $\xi$  is calculated based on the Bilger's mixture fraction formula [94]. The flamebase is defined as the most upstream point of  $Y_{OH} = 8.0 \times 10^{-4}$  isoline. The lifted flames can be categorized into three different regimes such as low  $U_0$  ( $< 6.0$  m/s), high  $U_0$  ( $> 6.7$  m/s), and transition regime ( $U_0 \sim 6.0$  m/s) inbetween based on the location of their flamebases and flame shapes. In the low  $U_0$  regime, the flamebase lies at the  $\xi_{st}$  isoline and the flame shape looks like a normal edge flame. In the transition regime, the flamebase is located at the end of the closed tip of the  $\xi_{st}$  isoline and its shape is relatively flat compared to those in the low  $U_0$  regime. In the high  $U_0$  regime, the flamebase is located far downstream of the  $\xi_{st}$  isoline closed tip and the flamebase shape is concave toward the fuel jet direction, which seems like MILD combustion.

From flame temperature point of view, the low  $U_0$  and transition regimes are not included in MILD combustion while the high  $U_0$  regime is categorized as MILD combustion. For instance, the maximum flame temperature of  $U_0 = 8$  m/s case is 1843 K, and hence,  $(T_{max} - T_0)/T_{ig} < 1$ , which indicates that the lifted flame with  $U_0 = 8$  m/s exhibits a MILD combustion structure and its stabilization mechanism is considered as autoignition. For the high  $U_0$  regime, important intermediate species including  $CH_2O$ ,  $HO_2$ , and  $H_2O_2$  are predominant in the upstream of the flamebase, which indicates that autoignition affects the stabilization of the lifted flames. In the low  $U_0$  regime, the flamebase lies at the  $\xi_{st}$  line which is different from the previous result that flamebase lies at a fuel-lean mixture. The flame shape looks like a non-premixed normal edge flame, while temperature condition is autoignitable. The details of stabilization mechanisms of each

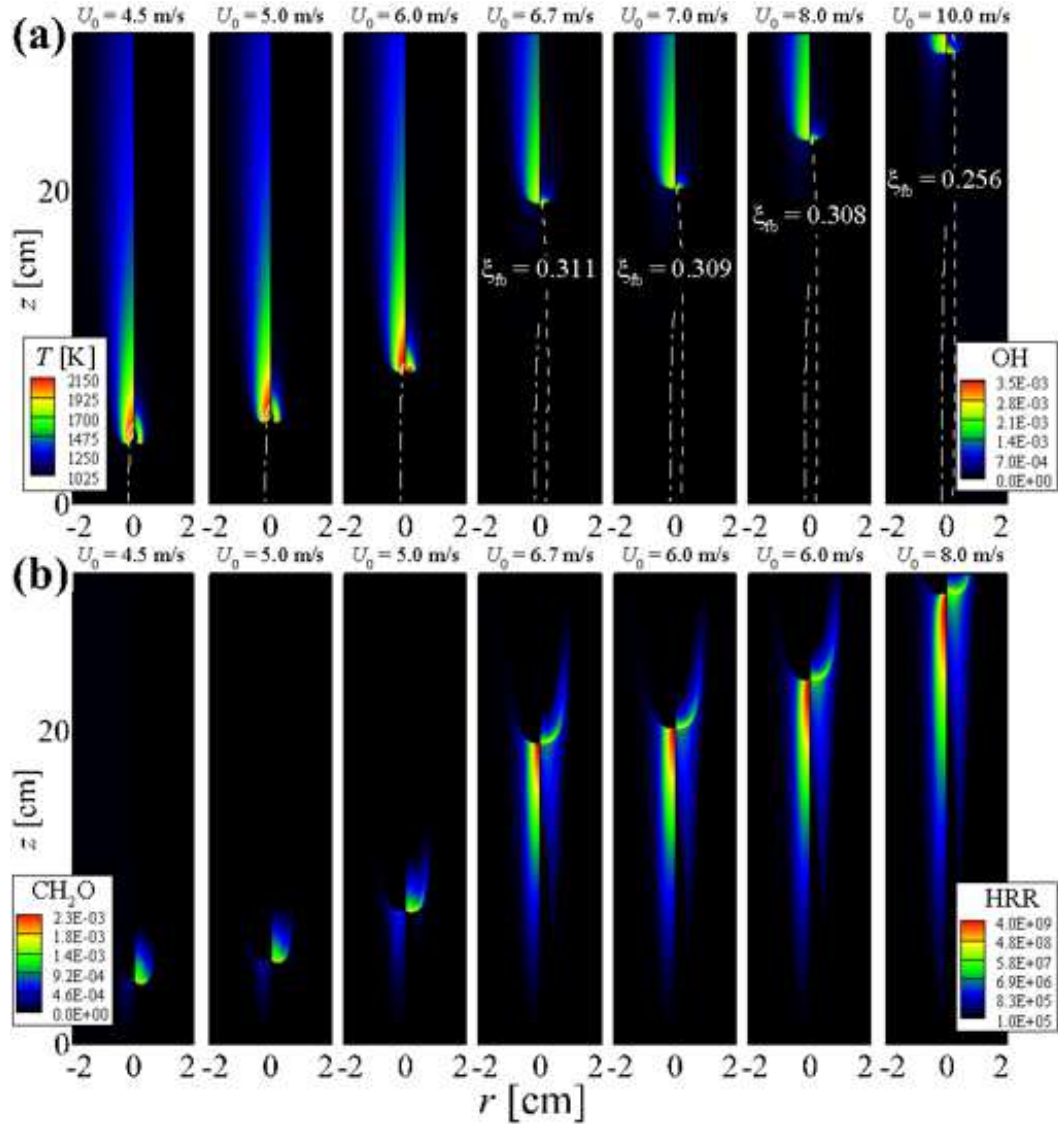


Figure 4.2: Isocontours of (a)  $T$  (left half) and  $Y_{OH}$  (right half) and (b)  $Y_{CH_2O}$  (left half) and heat release rate (HRR) (right half) for autoignited laminar lifted *n*-heptane jet flames for various fuel jet velocities  $U_0$  ( $T_0 = 1025$  K). The dashed and dash-dotted lines in (a) represent the mixture fraction isoline passing through the flamebase,  $\xi_{fb}$ , and the stoichiometric mixture fraction isoline,  $\xi_{st}$  ( $= 0.494$ ), respectively.

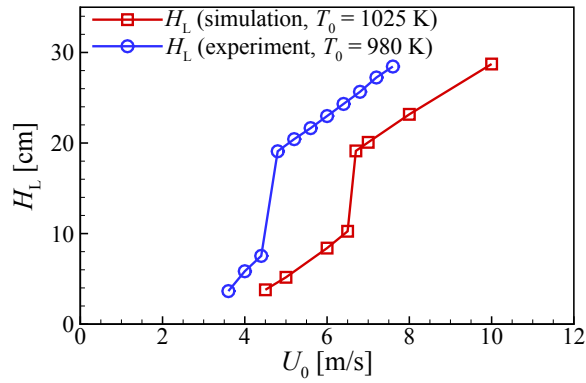


Figure 4.3: Experimental and simulation results of autoignited *n*-heptane fuel liftoff height in relation to jet velocity

case will be discussed in the following sections.

## 4.4 Effect of Schmidt Number on the Liftoff Characteristics

In this section, the sudden jumping of  $H_L$  behavior is discussed from the Schmidt number of the fuel jet,  $Sc$ , point of view.  $Sc$  is a non-dimensional number which is the ratio of momentum diffusivity,  $\nu$ , to mass diffusivity,  $D$ . A non-autoignited laminar lifted flame can exist only when  $Sc$  is greater than unity [70,123]. A laminar lifted *n*-heptane jet flame exhibits an increasing  $H_L$  behavior with increasing  $U_0$  in non-autoignitive condition [23]. Since  $Sc$  of the *n*-heptane jet is greater than unity, the laminar lifted flames in present simulations can be stable until they are blown out. Dilution of *n*-heptane fuel with  $N_2$  affects the length of stabilized flame section where edge flame could be stabilized in  $\xi_{st}$  condition. Figure. 4.4 shows a schematic of highly diluted *n*-heptane jet flames stabilized lifted flame. Dilution of fuel makes isoline of  $\xi_{st}$  to a closed curve. At sufficiently low  $U_0$ , diluted *n*-heptane flamebase located in  $\xi_{st}$  in the closed-curve area (the middle of Fig. 4.4). However, lifted flame blows out after certain  $U_0$ , which moves flamebase to outside of  $\xi_{st}$  closed curve (the right of Fig. 4.4; in the present simulation, blowing out starts  $U_0 = 6.5$  m/s).

For non-autoignited non-premixed lifted jet flames, once blowing out occurs, flames

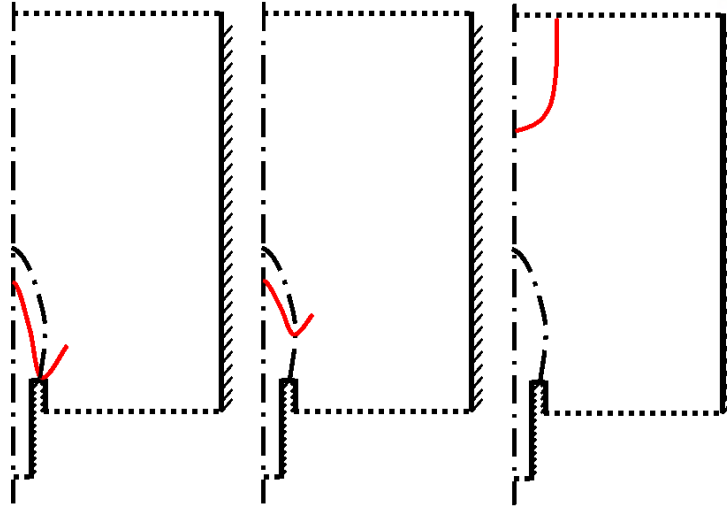


Figure 4.4: Simplified flame shape of highly diluted  $n$ -heptane laminar lifted flame in autoignition condition; red solid and black dashed lines indicate a flamebase and stoichiometric mixture fraction line respectively. The jet velocity goes up from the left to the right

are not stabilized downstream anymore. In the present simulation, the fuel and coflow temperatures are high enough to induce autoignition of the fuel jet, and as such, the flame comes to be stabilized by autoignition. In transient simulations of autoignited laminar lifted  $n$ -heptane jet flames, it is found that an ignition kernel develops far downstream of the flamebase for high  $U_0$  cases. For low  $U_0$  cases, however, an ignition kernel develops at the early stage of simulations far downstream of the simulation domain. The existence of the ignition kernel in high  $U_0$  case may explain the sudden jumping behavior of  $H_L$ . When  $U_0$  is greater than 6.5 m/s in which the flamebase location is downstream of the tip of  $\xi_{st}$  closed curve, the lifted flame is not able to sustain stoichiometric condition and move to the place where the ignition kernel exists. The detail stabilization mechanisms of  $\xi_{st}$  flamebase and MILD combustion like flame will be discussed in the next section.

## 4.5 Stabilization Mechanisms

In this section, stabilization mechanisms of autoignited laminar lifted  $n$ -heptane jet flames are further analyzed by examining their flame structures and flame propagation speeds.

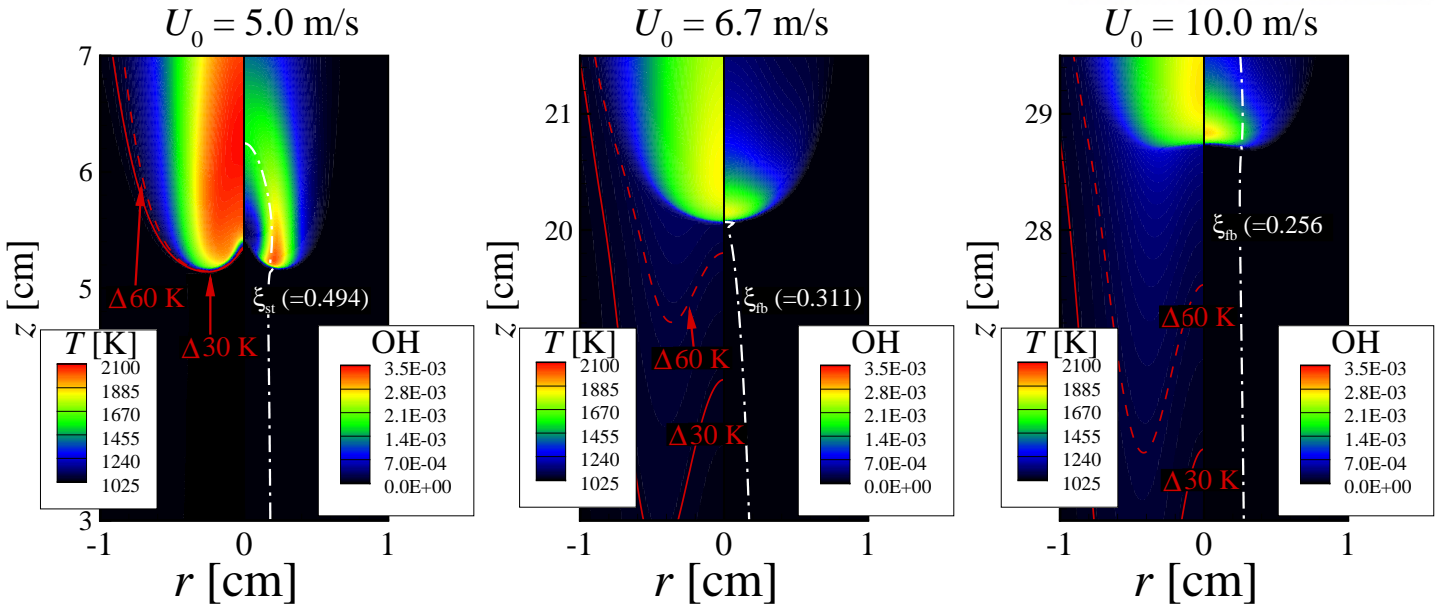


Figure 4.5: Isocontours of temperature and  $Y_{OH}$  for selective  $U_0$

Figure 4.5 shows isocontours of temperature and  $Y_{OH}$ . Red lines indicate isolines of certain temperature values. For low  $U_0$  ( $= 5.0$  m/s), there exists large temperature gradient near the flamebase while for  $U_0 = 6.7$  and  $10$  m/s cases, temperature rises gradually along the  $z$ -direction, exhibiting a broad thermal cooking region upstream of the flamebase. There are two kinds of flame shapes for jumped condition. For  $U_0 = 6.7$  m/s, the flamebase is convex toward the upstream while it is concave toward the upstream for  $U_0 = 10$  m/s case, which was already reported in previous experiments [24]. Isocontours of  $Y_{OH}$  and temperature for different  $U_0$  imply that the flame shape and temperature gradient of low  $U_0$  case is normal propagating edge flame with high temperature gradient along the streamwise direction. In case of jumped condition, flames with MILD combustion with two different convex and concave modes depending on  $U_0$  are observed and broad thermal cooking region occurs upstream of flamebase.

To better understand the effects of ignition on the stabilization mechanisms of autoignited laminar lifted  $n$ -heptane jet flames, the propagation speed of their leading edge,  $S_e$ , is calculated through the density-weight displacement speed,  $S_d^*$ , which has been used to calculate the propagation speed of reaction fronts in previous sections:

$$S_d^* = \frac{1}{\rho_u |\nabla Y_k|} (\omega_k - \frac{\partial}{\partial x_j} (\rho Y_k V_{j,k})), \quad (4.1)$$

where  $Y_k$  is the mass fraction,  $V_{j,k}$  the diffusion velocity in the  $j$ -direction,  $\omega_k$  the net production rate of species  $k$ , and  $\rho_u$  is the density of the unburnt mixture.  $S_d^*$  is evaluated at the most upstream point of  $Y_{OH} = 8.0 \times 10^{-4}$  isoline defined as the flamebase. In this study,  $S_L$  upstream of the flamebase is calculated from transient 1-D reactive simulations as in the previous sections.

The initial mixture conditions for the 1-D simulations were obtained from those at several locations upstream of the flamebase along the  $\xi_{fb}$  isoline. Details of obtaining  $S_L$  are in previous chapter. The propagation speed of the combustion wave,  $S_d^*$ , can be considered as the laminar burning velocity,  $S_L$ . It is not straightforward to precisely determine  $S_L$  values for high  $U_0$  regimes because heat and radicals are still generated within the thermal cooking region. To reasonably estimate  $S_L$ , therefore, we evaluate it based on the local mixture components and temperature upstream of the flamebase, for which species components are converted to the original reactants at the inlets (i.e.  $n$ -heptane,  $H_2$ ,  $O_2$ , and  $N_2$ ). Then, we evaluate  $S_L$  of the unburned mixture at the local temperature.

Figure 4.6 shows  $S_e/S_L$  for several  $U_0$ .  $S_e/S_L$  at the flamebase is found to be  $O(1)$  for low  $U_0$  (normal edge flame) denoted as Regime I. It indicates that in low  $U_0$  regime, the flame propagation speed is comparable to the corresponding laminar flame speed. In Regime II ( $U_0 = 6.7 \sim 8$  m/s),  $S_e/S_L$  becomes larger than those in Regime I. The ignition process undergoing upstream of the flamebase increases the propagation speed significantly, which is four times larger than the laminar flame speed. For  $U_0 = 10$  m/s case,  $S_e/S_L$  is much greater than those in Regime I and II. Considering flame structures and  $S_e/S_L$  value, we can obtain the following results: 1) lifted flames in Regime I have normal edge flame shape and their propagation speeds are comparable to the laminar flame speed; 2) lifted flames in Regime II are categorized as MILD combustion with convex toward downstream flame structure and their propagation speed is larger than

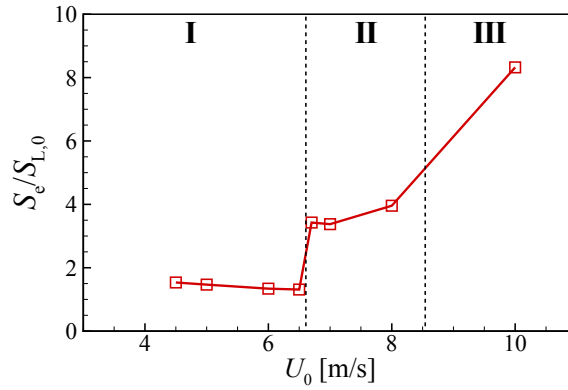


Figure 4.6:  $S_e/S_L$  in relation to jet velocity

laminar flame speed; 3) the characteristics of lifted flames in Regime III are similar to those in Regime II except for the shape of flamebase which is concave toward to upstream of its flamebase. These results imply that the ignition process is not important to flame stabilization in Regime I, while thermal ignition process upstream of the flamebase plays an important role in stabilizing the lifted flames in Regime II and III.

## 4.6 Liftoff Height Jump

In this section, the abnormal liftoff height behavior of autoignited laminar lifted *n*-heptane jet flames is analyzed with momentum and species diffusion characteristics.  $Sc$  effect of  $H_L$  jumping was mentioned in the previous section. Figure 4.7 shows the radial distributions of  $\xi$  and  $U_z$  at several flow time,  $\tau_{\text{flow}}$ .  $U_z$  is streamwise flow velocity and  $\tau_{\text{flow}}$  is defined as  $z/U_0$ .  $U_z$  is normalized by the maximum fuel jet velocity  $2U_0$  which occurs at the center of the fuel jet. Note that  $\xi$  and normalized  $U_z$  are similar among different  $U_0$  for every  $\tau_{\text{flow}}$ . Decreasing rate of  $\xi$  along  $\tau_{\text{flow}}$  is higher than  $U_z$  because the momentum diffusion is larger than species mass diffusion ( $Sc > 1$ ) and fully developed velocity profile is already achieved at the fuel nozzle exit while mixture fraction profile exhibits an uniform profile.

Figure 4.8 shows the radial profiles of  $U_z$  and  $\xi$  at several  $\tau_{\text{flow}}$  of  $U_0 = 6.7$  m/s at which  $H_L$  jumping occurs. Figure 4.9 shows isocontours of  $Y_{\text{OH}}$  for  $U_0 = 6.7$  m/s case. Note that the flow passes through  $\xi_{\text{st}} = \xi_c$  point between  $\tau_{\text{flow}} = 10$  and 20 ms.  $\xi_c$  is the mixture



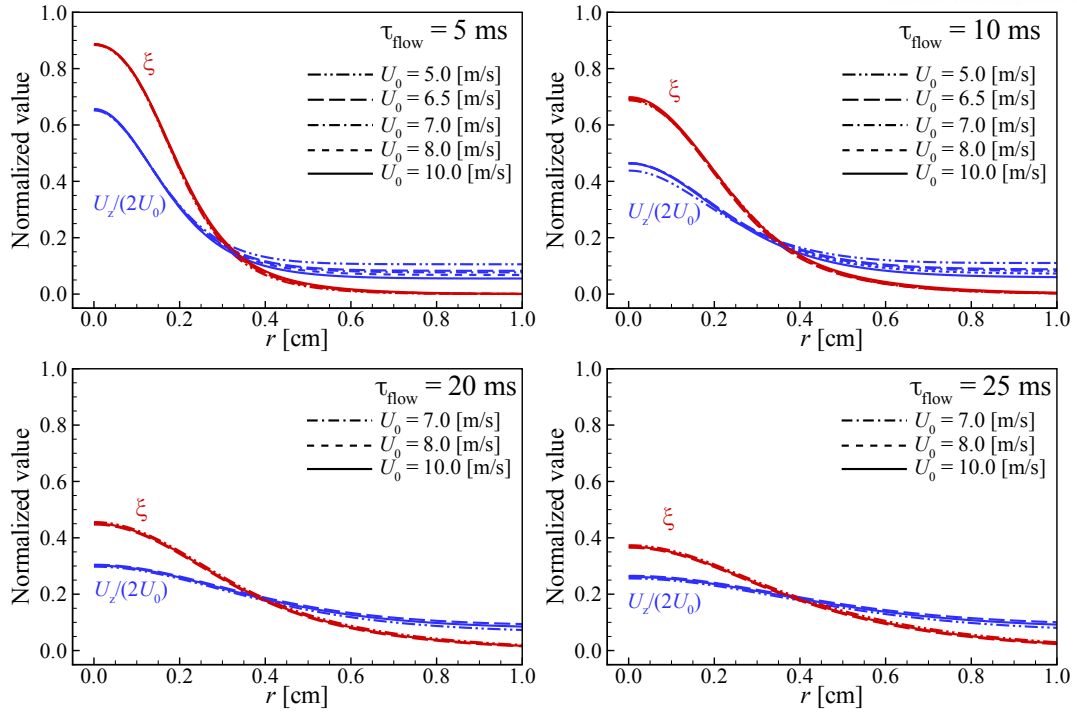


Figure 4.7: Radial distribution of  $U_z$  and  $\xi$  at selective  $\tau_{\text{flow}}$  for all  $U_0$

fraction at  $r = 0$ . Temperature rise is less than 20 K in this region. Such small increment of temperature leads to negligible increment of  $S_e$ . The amount of reduced mixture fraction, however, is more critical to the change of  $S_e$ .  $S_L$  upstream of the flamebase is calculated from transient 1-D reactive simulations. The initial mixture conditions for the 1-D simulations were obtained from those at several locations upstream of the flamebase along the center line ( $r = 0$ ). The temperature,  $\xi$  and  $S_L$  calculated along the center line are shown in Fig. 4.10. Note that  $S_L$  profile is similar to that of  $\xi$  relatively far upstream of the flamebase ( $\tau_{\text{flow}} < 20$  ms). It implies that the lifted flame cannot be stabilized at this interval. Schematics of  $U_z$  and  $S_e$  are shown in Fig. 4.11. Stable solution cannot be obtained. If the flamebase is located upstream of the intersection point ( $U_z = S_e$ ), large  $S_e$  makes the flamebase move downstream. On the contrary, large  $U_z$  makes the flame blown out when the flamebase is located downstream of the intersection point.

Figure 4.12 shows  $S_e$  and  $U_z$  along the centerline upstream of the flamebase for high  $U_0$  cases. Near the flamebase, the amount of temperature increment is relatively large compared to the 20 K in region where  $\tau_{\text{flow}} = 10$  to 20 ms. Temperature rising plays an important role in increasing  $S_e$ . The change in  $S_e$  can be attributed to the increase of

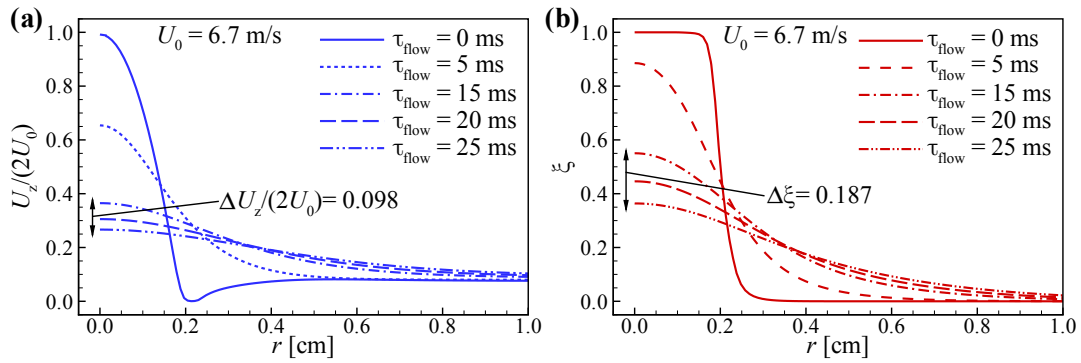


Figure 4.8: Radial distribution of  $U_z$  and  $\xi$  at selective  $\tau_{\text{flow}}$  for  $U_0 = 6.7$  m/s

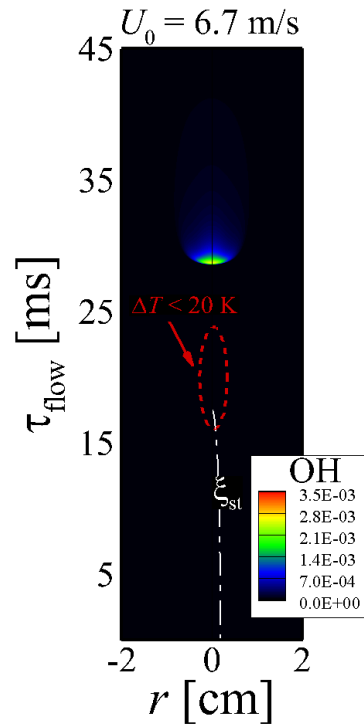


Figure 4.9: Isocontours of  $Y_{\text{OH}}$  with  $\tau_{\text{flow}}$  for  $U_0 = 6.7$  m/s, dash dot line indicates stoichiometric mixture fraction isoline

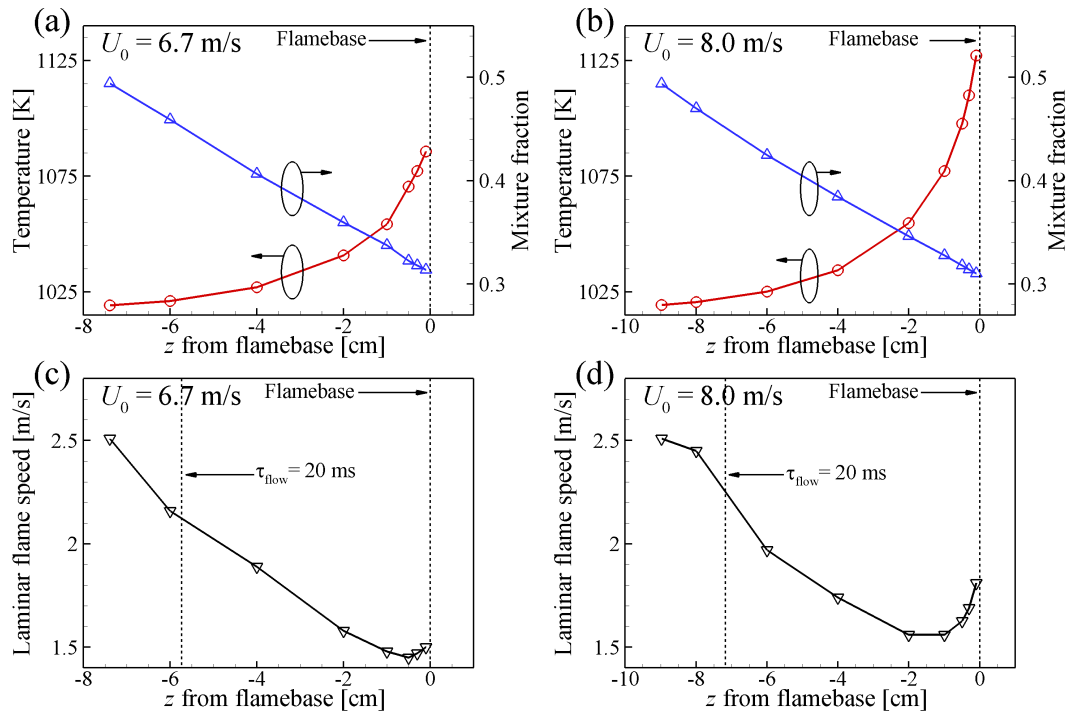


Figure 4.10: Variation of temperature and  $\xi$  along center of  $z$  axis and  $S_L$  along center of  $z$  axis for case  $U_0 = 6.7$  m/s (a),(c) and 8.0 m/s (b), (d).

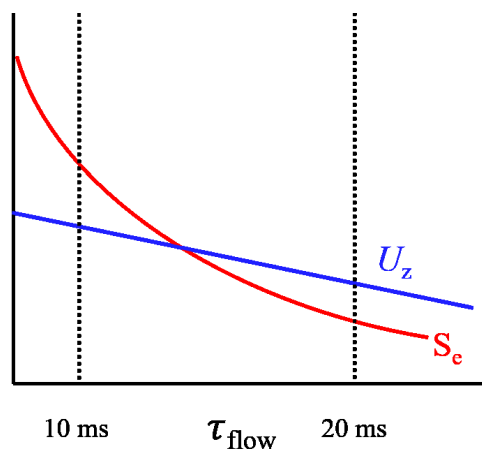


Figure 4.11: Schematic of  $U_z$  and  $S_e$  along  $\tau_{\text{flow}}$  far upstream of the flamebase

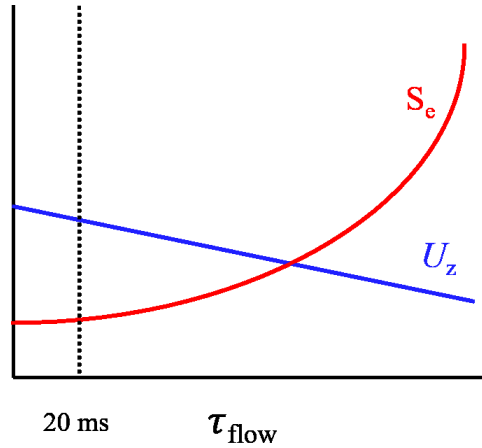


Figure 4.12: Simplified schematics of  $U_z$  and  $S_e$  along  $\tau_{\text{flow}}$  at near the upstream of flamebase

temperature upstream of the flamebase. After  $\tau_{\text{flow}} = 20$  ms,  $\xi_c$  gradient is small (see Fig. 4.7; The amount of  $\xi_c$  reduction in  $20 \text{ ms} < \tau_{\text{flow}} < 25$  ms is smaller than that in  $5 \text{ ms} < \tau_{\text{flow}} < 10$  ms) and it has small effect on changing  $S_e$ . The large amount of temperature increment leads to an increasing trend of  $S_e$  in the streamwise direction.  $S_e$  follows the rising trend of temperature near the flamebase as shown in Figs. 4.10(c) and (d). In this condition, stable solution can be obtained. The flamebase is formed near the point where the intersection of  $S_e$  and  $U_z$  curves. If the flamebase is located upstream of the intersection point, larger  $U_z$  makes the flame move downstream while it moves upstream if the flamebase is located downstream of the intersection point. Figure 4.12 shows a schematic of  $S_e$  and  $U_z$  near the flamebase.

Autoignitive condition with  $Sc > 1$  condition makes flames stabilized farther downstream of the closed tip of  $\xi_{\text{st}}$  isoline. The extended flame stabilization in Regimes II and III leads to the sudden jump of  $H_L$ . Stabilization mode of the lifted flames in Regime I is the normal edge flame propagation. A normal edge flame is blown out when  $U_0 > 6.5$  m/s. However, autoignitive temperature can stabilize the flame at the point where  $S_e = U_z$ . Because of  $Sc > 1$ , there exists a distance where unstable flame solution exist for Regime II and III.

## 4.7 Conclusions

The characteristics of autoignited laminar lifted  $n$ -heptane jet flames in heated coflow air were numerically investigated using laminarSMOKE code with a 68-species skeletal chemical kinetic mechanism of  $n$ -heptane oxidation. The detailed numerical simulations were performed for various fuel jet velocities under the autoignition temperature condition. The numerical simulations captured qualitatively abnormal lifted flame behaviors such that sudden jump of liftoff height, in agreement with those in experiments. The following results were obtained from the simulations together with the  $Sc$  and displacement speed analyses.

1. Considering the flame structure and  $(T_{\max} - T_0)/T_{\text{ig}}$ , we categorized the autoignited laminar lifted  $n$ -heptane jet flames into three different combustion regimes: Regime I - tribrachial edge flame, Regime II - transition, and Regime III - the MILD combustion regimes.
2. From the displacement analysis, it was identified that the propagation speed of Regime I lifted flame is comparable to the laminar burning velocity while  $S_e$  at the flamebase for Regimes II and III is much larger than that of  $S_L$ .
3. In the tribrachial edge flame regime (regime 1), flamebase located in  $\xi_{\text{st}}$  line and its flame speed is comparable to laminar burning velocity. These results lead that the stabilization mechanism of regime 1 is normal flame propagation. MILD combustion regime (regime 2 and 3), however, the broad thermal cooking region and relatively high  $S_e/S_L$  suggest that ignition affects the overall flame stabilization at the upstream of flamebase.
4. The  $Sc$  analysis identify that sudden jump of  $H_L$  at the transition regime. Normal edge flame blows out after  $U_0 = 6.5$  m/s where flamebase is located in the tip of  $\xi_{\text{st}}$  closed curve.  $Sc > 1$  condition generates the interval where lifted flames are unstable. The sudden jump  $H_L$  is the result of the unstable interval. After the unstable interval region, lifted flames stabilized by ignition which occurs far

downstream of the MILD combustion flamebase. These regimes 2 and 3 are the extended lifted flame regimes caused by autoignition temperature condition.

## Chapter V

# Turbulent Lifted Hydrogen Jet Flames in Heated Coflow Air

### 5.1 Introduction

The configuration of a turbulent lifted jet flame is generally adopted in many modern combustion systems such as gas turbine combustors, diesel engines, and commercial boilers because it can effectively generate heat from a compact size combustor while protecting the fuel nozzle from hot product gas. Since the flame is essentially lifted from the fuel nozzle, it is inevitably vulnerable to blowout by high speed fuel jet. As such, the stabilization of turbulent lifted jet flames is one of the key design parameters for development of such combustors and its fundamental stabilization mechanisms have been a long-term research topic in the combustion community [8, 19, 70, 124, 125]. However, the stabilization mechanisms of turbulent lifted jet flames are quite complicated especially under various coflow temperature conditions such that it still remains challenging to develop a predictive model for accurate description of their characteristics in many different situations [71, 73–75, 107].

Numerous experimental and numerical studies of stabilization mechanisms of turbulent lifted jet flames at room temperatures have been conducted and various theories on the mechanisms have been proposed thus far [124, 125]. In many practical applications, however, the ambient oxidizer around a fuel jet is hot enough to initiate auto-ignition of

the fuel/air mixture upstream of the lifted flamebase. As such, auto-ignition has been found as one of the primary stabilization mechanisms of turbulent lifted flames in hot vitiated coflows [8, 71, 73, 95, 107, 126–129].

Previous 3-D direct numerical simulations (DNSs) of hydrogen [71] and ethylene [73] jet flames in highly-heated coflows revealed that turbulent lifted jet flames are stabilized primarily by the auto-ignition of fuel-lean mixtures supported by the hot coflows for which temperatures exceed the auto-ignition limit. Therefore, the lift-off heights are determined by the balance between the local axial velocity and consecutive auto-ignition events occurring in hot fuel-lean mixtures. Kerkemeier et al. [128] also conducted 3-D DNSs of a laboratory-scale hydrogen plume in turbulent hot coflow and investigated the role of auto-ignition spots to stabilize lifted flames at different coflow temperatures. More recently, Minamoto and Chen [129] investigated the effects of two-stage ignition on the stabilization of a turbulent lifted DME jet flame. However, the stabilization characteristics of turbulent lifted jet flames in mildly-heated coflows, whose temperatures are near the auto-ignition limit, have not been systematically investigated, even though their overall features were reported from experimental studies [123, 130]. From the experiments, the lift-off height is found to correlate well with the inlet jet velocity based both on the premixed flame theory and the large eddy theory regardless of the inlet temperatures. Also in previous numerical simulations [131] revealed that how ignition affect the overall combustion process in premixed flame propagation. The combustion mode indicator was introduced to identify that how much ignition get involved in the entire combustion process.

Therefore in this chapter, 3-D DNSs of turbulent lifted hydrogen jet flames with different coflow temperatures near the auto-ignition limit are performed to elucidate their stabilization mechanisms and structure characteristics by examining instantaneous and time-averaged flame/flow characteristics near the flamebase. The role of important species and reactions on the stabilization of turbulent lifted flames is investigated by adopting chemical explosive mode analysis (CEMA) [30–32] and the combustion mode indicator [131].



## 5.2 Numerical Method and Initial Conditions

DNSs of turbulent lifted hydrogen jet flames were performed in a three-dimensional slot-burner configuration, which has been adopted for previous studies [71, 73, 129]. Diluted hydrogen fuel (65 % hydrogen + 35 % nitrogen by volume) issues from a central jet at an inlet temperature,  $T_j = 400$  K, and atmospheric pressure. Surrounding the central jet on either side, co-flowing heated air streams issue at  $T_c = 750$  K (Case L), 850 K (Case M), 950 K (Case H) and 1100 K (Case Ig). Case Ig (Ig is abbreviation of ignition) is reference case that was simulated in previous study and the details of this lifted flame, readers are referred to Ref. [71]. Comparison between the present case and reference case will be shown in Table V.1. The following configurations are related to Cases L, M and H. The coflow temperatures are high enough to stabilize the flames but not enough to ignite the mixtures within the computational domain. As such, the mixtures are ignited by a hot ignition source as in [71]. The mixture composition was selected such that the stoichiometric mixture fraction,  $\xi_{st} = 0.199$ , resides in a region of high shear in the spatially developing jet. The mean inlet axial velocity,  $U_{in}$ , is given by:

$$U_{in} = U_c + \frac{U_j - U_c}{2} \left( \tanh\left(\frac{y+H/2}{2\delta}\right) - \tanh\left(\frac{y-H/2}{2\delta}\right) \right), \quad (5.1)$$

where  $U_c$  and  $U_j$  denote the mean coflow and mean inlet jet velocities, respectively.  $H$  ( $= 2.0$  mm) is the jet width at the inlet. The computational domain is  $15H \times 20H \times 3H$  in the streamwise,  $x$ , transverse,  $y$ , and spanwise,  $z$ , directions for Case L to Case H. A uniform grid spacing of  $15 \mu\text{m}$  is used in the  $x$ - and  $z$ -directions. The  $y$ -directional mesh is algebraically stretched outside of the flame and shear zones as in [71, 73]. The compressible Navier–Stokes, species continuity, and total energy equations were solved using the Sandia DNS code, S3D [53], with a detailed hydrogen-air chemical mechanism by Li et al. [132]. Improved non-reflecting boundary conditions by Yoo et al. [63, 64] were used in the  $x$ - and  $y$ -directions. Periodic boundary conditions were applied in the  $z$ -direction. Based on  $U_j$  and the streamwise domain length, a flow-through time,  $\tau_j$

( $= L_x/U_j$ ), is 0.125 ms and the jet Reynolds number,  $Re_j$ , is approximately 8,000.

Table V.1: Physical parameters of the case L, M, H and Ig.

Case	$U_c$ (m/s)	$U_j$ (m/s)	$T_j$ (K)	$Re_j$	$H$ (mm)
L, M and H	2	240	400	8000	2.0
Ig	4	347	400	10000	1.92

Following the procedure adopted to improve computational expediency in [73], the solution on a coarse grid resolution of 40  $\mu\text{m}$  was initially advanced until the flame attained statistical stationarity. The solutions were then mapped onto a finer grid of 15  $\mu\text{m}$  and were advanced at a constant time step of 5 ns through  $4\tau_j$ . The simulations were performed on the Cray XT5/XK7 at Oak Ridge National Laboratory and each simulation required 2.5 million CPU-hours running for 6.5 days on 16,000 processors. After the ignition by the hot source, lifted jet flamebases approached statistical stationarity and fluctuated about their steady stabilization lift-off heights,  $\bar{h}$ , of approximately  $\bar{h}_L/H = 5.3$ ,  $\bar{h}_M/H = 4.0$ , and  $\bar{h}_H/H = 2.4$ , where subscripts L, M, and H denote Cases L, M, and H, respectively. The reference case of  $\bar{h}_{Ig}/H = 2.6$ . Note that the homogeneous explosion limit of the stoichiometric hydrogen/air mixture is approximately 810 K [70].

### 5.3 Flame Structure and Dynamics

Figure 5.1 shows 3-D volume rendering of the mass fractions of OH and  $\text{HO}_2$  at  $t/\tau_j = 2.0$  for the three cases. OH is often used as a marker for a lifted flamebase or high temperature reaction region and  $\text{HO}_2$  is known as a precursor in initiating auto-ignition upstream of the flamebase [8, 71, 73, 107]. It is readily observed that as  $T_c$  increases from Case L to Case H, the lift-off height decreases and  $\text{HO}_2$  appears further upstream of the occurrence of OH, which indicates that auto-ignition becomes stronger and has a greater effect on the the stabilization of the lifted flame with increasing  $T_c$ . Note that in the present study, the flamebase is defined as the most upstream point of  $Y_{\text{OH}} = 0.001$  isoline

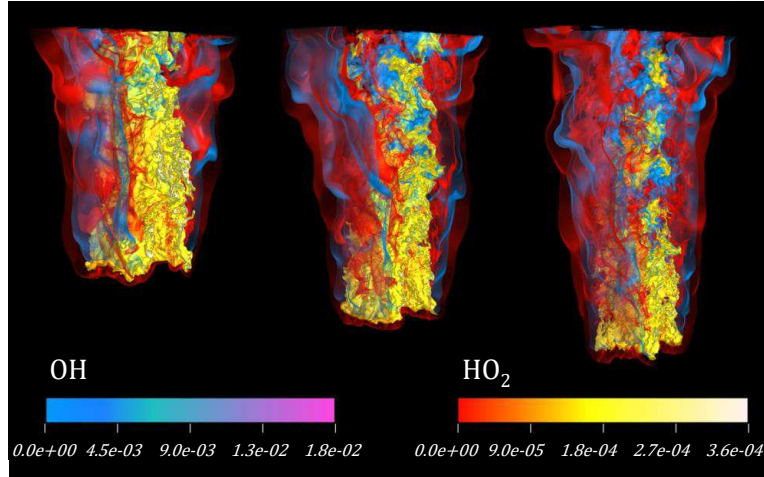


Figure 5.1: 3-D volume rendering of the mass fraction of OH and HO<sub>2</sub> for Cases L, M, and H (from left to right).

which represents approximately 5% of its maximum in the domain as in [71].

To further identify the characteristics of the lifted flames, the cross-stream conditional Favre mean,  $\langle \phi | \eta \rangle$  of a variable,  $\phi$ , is examined, where  $\eta$  is the sample space of the mixture fraction,  $\xi$  [71, 73]. Figure 5.2 shows conditional Favre mean of heat release rate,  $\langle \dot{q} | \eta \rangle$ . Several points are noted. First, in Case L  $\langle \dot{q} | \eta \rangle$  vanishes in fuel-rich mixtures ( $\eta > 0.7$ ) even far downstream of the flamebase. In Case H, however, significant  $\langle \dot{q} | \eta \rangle$  occurs even in fuel-rich mixtures downstream of the flamebase. Since  $h_H$  is smaller than  $h_L$ , the shear layer where most reactions occur in Case H is narrower than that in Case L. Therefore, turbulence can effectively transport heat from the flame to cold fuel-rich mixtures, leading to relatively large heat generation even in fuel-rich mixtures with  $\eta > 0.7$  for Case H. Second, in Cases M and H relatively large  $\langle \dot{q} | \eta \rangle$  occurs even in fuel-lean mixtures ( $\eta < 0.2$ ) near the flamebase compared to Case L, suggesting that ignition process at fuel-lean mixtures may affect the flamebase dynamics. Moreover, the maximum  $\langle \dot{q} | \eta \rangle$  occurs within a jet width downstream of the lift-off height for each of the cases. It is also observed that the peak  $\langle \dot{q} | \eta \rangle$  occurs at stoichiometric to slightly rich conditions within a jet width downstream of the flamebase and rapidly decreases further downstream. This result implies that for all cases, vigorous reaction occurs within a jet width downstream of the flamebase, similar to previous studies [71, 73]. Third, two peaks in  $\langle \dot{q} | \eta \rangle$  form

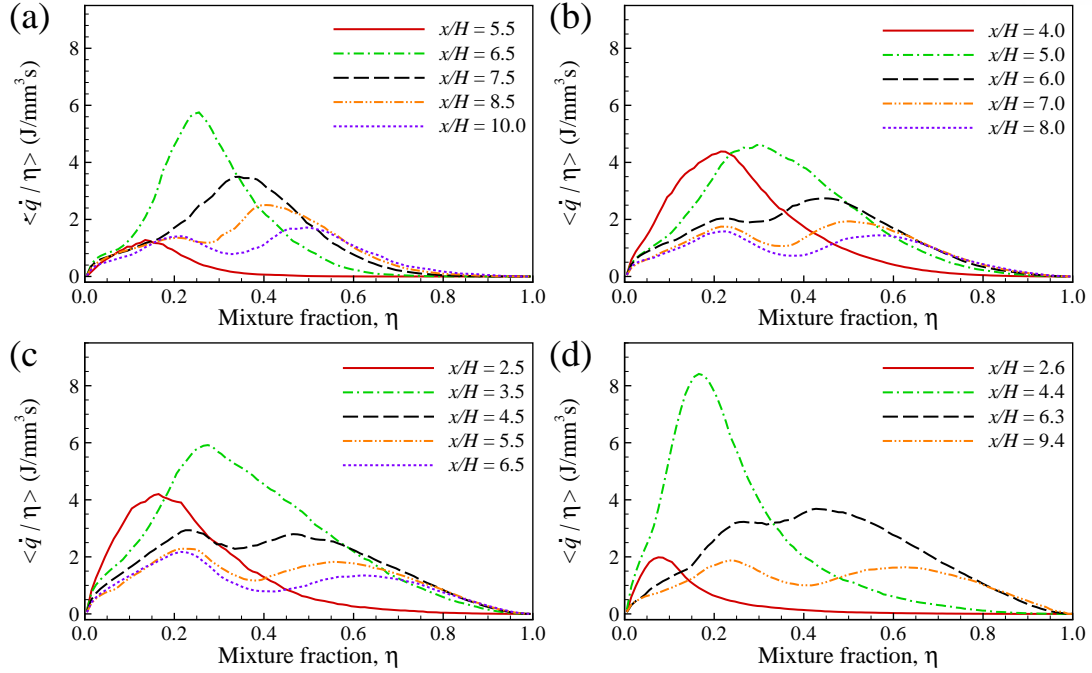


Figure 5.2: Axial variation of conditional Favre mean of  $\dot{q}$  (a) Case L, (b) Case M, (c) Case H and (d) Case Ig.

further downstream of the flamebase, one centered near the stoichiometric and the other centered in fuel-rich conditions, similar to the characteristics of laminar/turbulent lifted jet flames [71, 73, 123].

To elucidate the the stabilization mechanism of lifted flames, the axial variation of conditional Favre mean of Damköhler number,  $\langle Da|\eta \rangle$ , is examined as shown in Fig. 5.3. Here,  $Da$  is defined as the ratio of reaction rate to diffusion term of the  $H_2O$  species transport equation. As such, a large value of  $Da$  ( $\gg O(1)$ ) indicates auto-ignition while  $Da \sim O(1)$  denotes flame propagation. It is readily observed that  $\langle Da|\eta \rangle$  exhibits significantly different behavior near the flamebase for different cases. For Case H,  $\langle Da|\eta \rangle$  exhibits large value ( $\gg 1$ ) at fuel-lean mixtures near and upstream of the flamebase. Though, the maximum  $\langle Da|\eta \rangle$  of Case H is almost half of Case Ig at the location of flamebase [71]. For Case L,  $\langle Da|\eta \rangle$  is nearly zero upstream of the flamebase and exhibits  $O(\sim 1)$  values near the flamebase. In addition, the variance of  $Da$  is relatively small compared to Case H, suggesting that flame propagation rather than auto-ignition is the main source of flame stabilization. For Case M,  $\langle Da|\eta \rangle$  exhibits the features of both

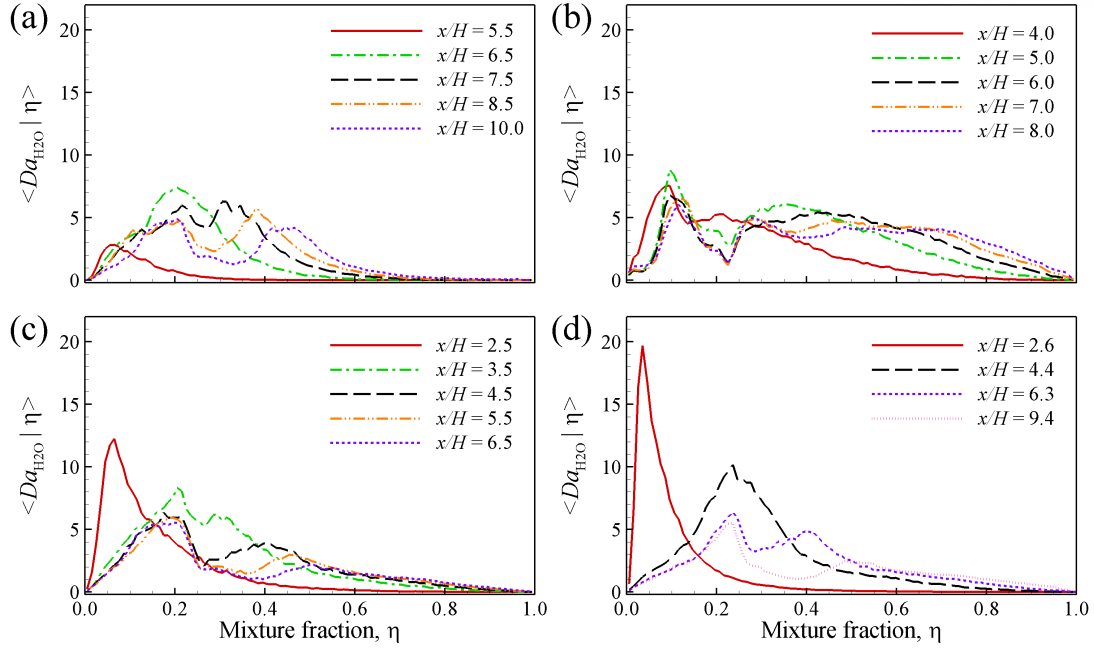


Figure 5.3: Axial variation of conditional Favre mean of  $Da$  (a) Case L, (b) Case M, (c) Case H and (d) Case Ig.

Cases H and L, implying that the flame stabilization of Case M may be affected not only by the auto-ignition of fuel-lean mixture but also by the flame propagation.

To further clarify the flame stabilization mechanism for the cases, the displacement speed,  $S_d$ , representing the speed of the flamebase is examined.  $S_d$  is defined as [71, 73]:

$$S_d = S_d^R + S_d^D = \frac{1}{\rho |\nabla Y_k|} \left( \dot{\omega}_k - \frac{\partial}{\partial x_j} (\rho Y_k V_{j,k}) \right), \quad (5.2)$$

where  $S_d^R$  and  $S_d^D$  represent the reaction and diffusion components of  $S_d$ , respectively. As such, by comparing their values, we can identify the origin of the flamebase speed and consequently, elucidate the dynamics of flame stabilization. In the present study, OH is chosen for the  $S_d$  analysis.

Figure 5.4 shows the temporal evolution of  $S_d^R$  and  $S_d^D$  of the flamebase at  $z = 1$  plane for each case. For Case L,  $S_d^R$  and  $S_d^D$  balance each other most of the time, implying that flame propagation is responsible for stabilizing the lifted flame. Therefore, the variation of  $S_d$  is marginal and the mean value of  $S_d$ ,  $\bar{S}_d$ , is approximately 2.3 m/s, similar to the 1-D laminar flame speed,  $S_L$ , under the same condition. For Case H,  $S_d^R$  of  $z = 1$  becomes

larger in magnitude than  $S_d^D$  over certain time intervals (e.g.,  $t/\tau_j = 1.2 \sim 1.9$ ). In the  $z$ -plane average value of  $S_d$ , however, shows different aspect compared to  $z = 1$  temporal  $S_d$  value.

Figure 5.5 shows the temporal evolution of  $z$ -plane average  $S_d$  at the flamebase.  $S_{d,z-avg}$  almost similar to Case L to Case H.  $S_{d,z-avg}$  varies almost  $\sim O(1)$ . In case of Ig,  $z = 1$  plane temporal evolution of  $S_d$  is more dynamic compared to Case L to H.  $z$ -plane average  $S_d$  of Case Ig has a large value around  $\sim O(10)$  or more. Figure 5.6 shows ignition kernel generated in upstream of flamebase in Case Ig. Other cases also show a growing spot that looks like an ignition kernel found on the upstream of flamebase is proved in a part of the flame spreading in the  $z$  direction. This kind of spot affects sudden decrease of  $h$ .

These results indicate that auto-ignition plays a critical role in stabilizing the flame for Case Ig. For Case H, however, the stabilization mechanism is more difficult to discern. The coflow temperature for Case H corresponds to the explosive condition for  $H_2/O_2$  mixture. Locally large coflow temperature affects increasing displacement speed which overcomes the laminar flame speed. However,  $z$ -plane average  $S_d$  is of  $O(1)$ .  $S_d$  values of Case M and L are nearly comparable to their corresponding laminar flame speed.

### 5.3.1 Chemical Explosive Mode Analysis

The ignition and flame stabilization characteristics are further identified using CEMA which has been successfully used to systematically identify key species and reactions for various types of laminar/turbulent flames [30–32,49,51,74,75,83,102,118,131,133]. Details of CEMA are explained in Chapter 2. The chemical features of a chemically reacting flow are associated with the Jacobian of the chemical source term in its discretized governing equations. To identify the chemical features from CEMA, a chemical mode is defined as an eigenmode of the Jacobian  $\mathbf{J}_\omega$ , which is associated with an eigenvalue,  $\lambda_e$ , and a corresponding pair of the left and right eigenvectors,  $\mathbf{a}_e$  and  $\mathbf{b}_e$ . Chemical explosive mode (CEM) is a chemical mode for which the real part of the eigenvalue is positive,  $\text{Re}(\lambda_e) > 0$ . To elucidate the ignition characteristics at the flamebase, a Damköhler

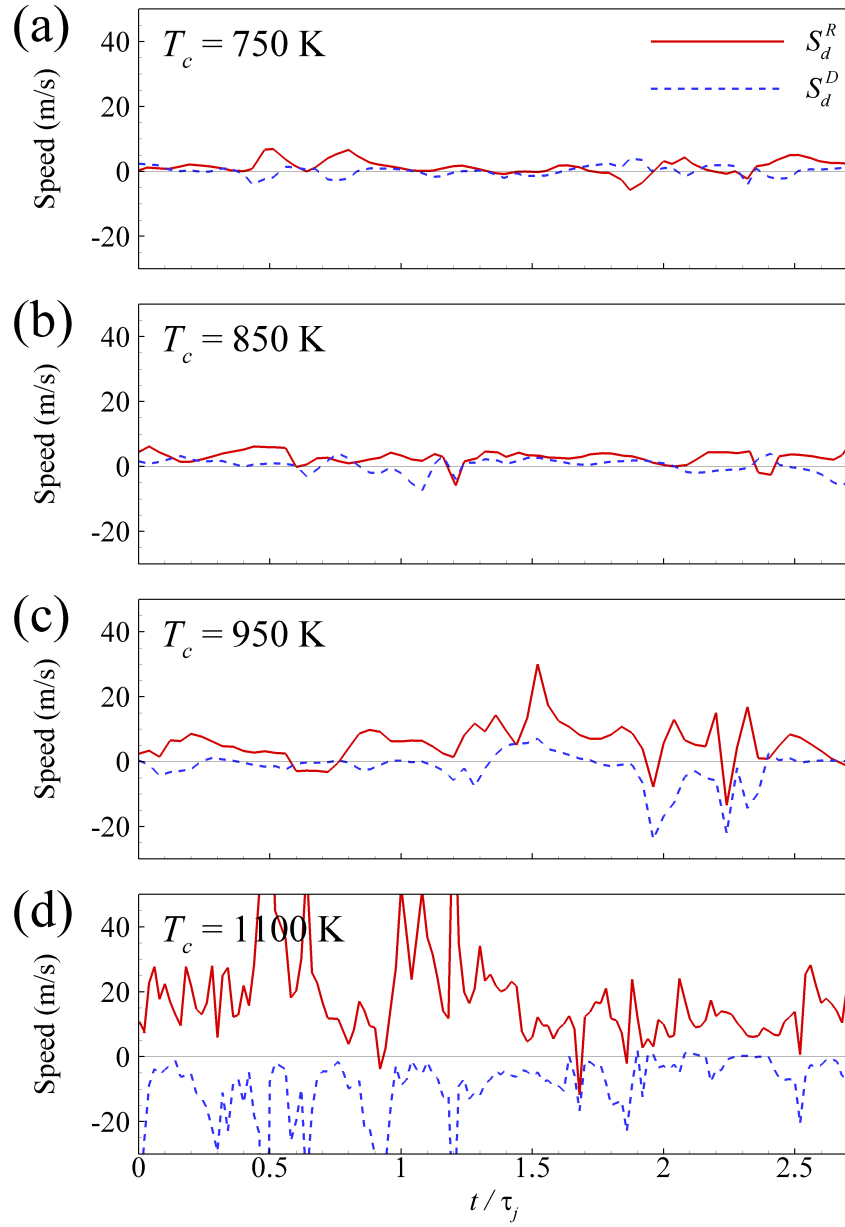


Figure 5.4: Temporal evolution of  $S_d^R$  and  $S_d^D$  at the flamebase in  $z = 0$  plane (a) Case L, (b) Case M, (c) Case H and (d) Case Ig.

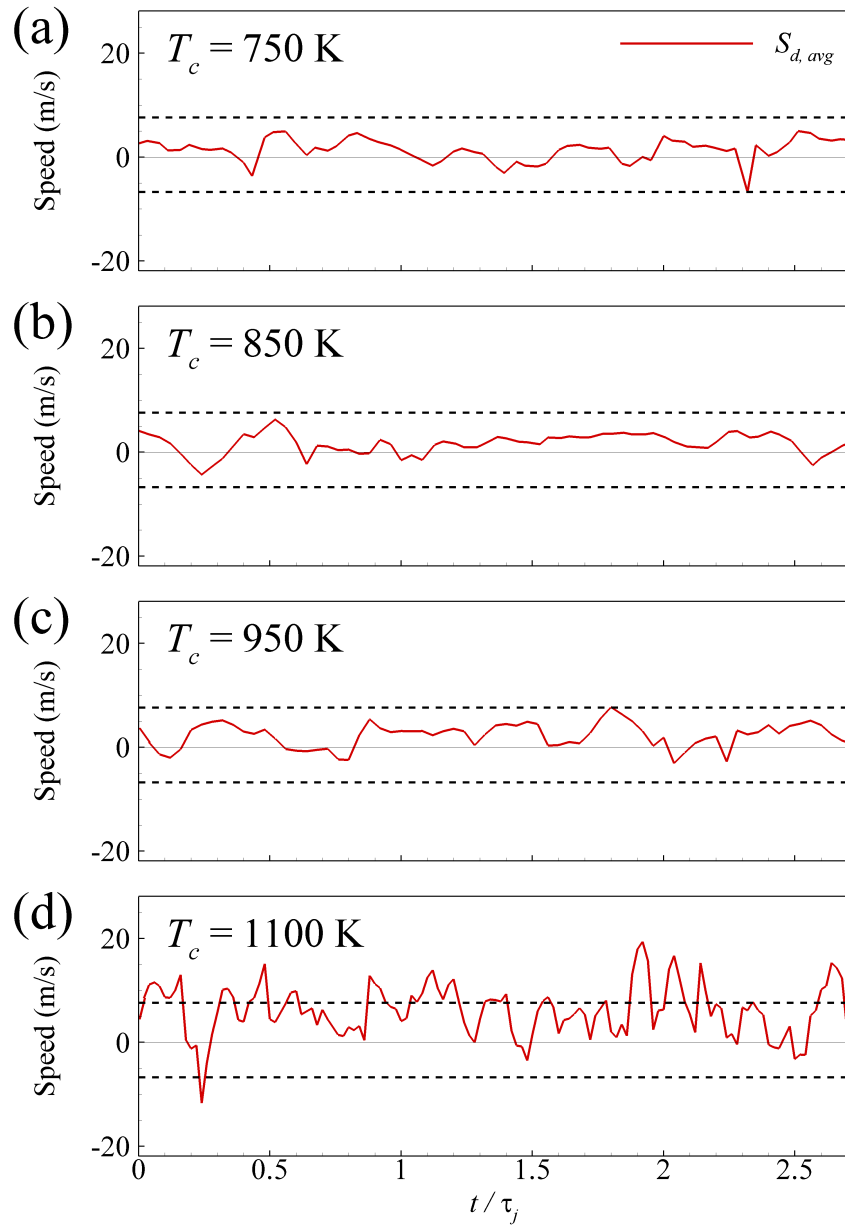


Figure 5.5: Temporal evolution of  $S_{d,avg}$  at the flamebase (a) Case L, (b) Case M, (c) Case H and (d) Case Ig.



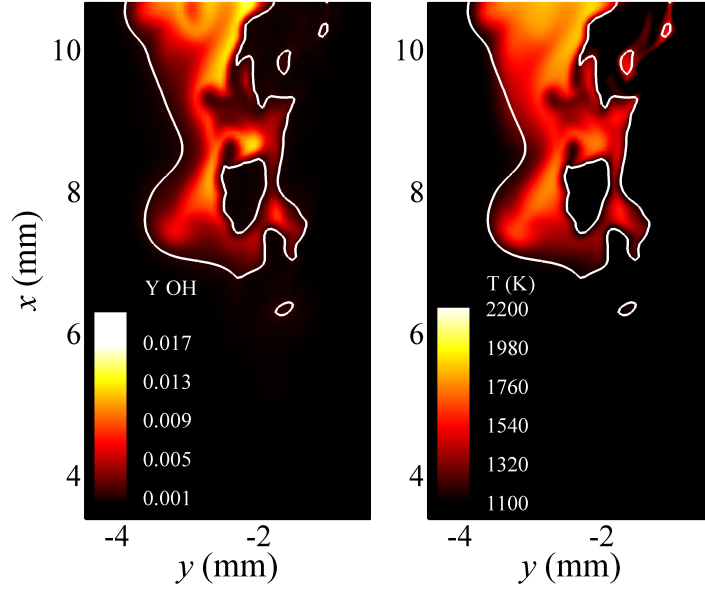


Figure 5.6: Ignition kernel at the upstream of flamebase in Case Ig white solid line indicates  $Y_{OH} = 0.001$ .

number,  $Da_c = \lambda_e \cdot \chi^{-1}$ , is adopted as in [71, 73, 118], where  $\chi (= 2D|\nabla\xi|^2)$  is the scalar dissipation rate.  $\lambda_e$  and  $\chi$  represent reciprocal timescales of the chemical reaction and transport [30–32, 51, 73]. Therefore, if  $Da_c \gg O(1)$ , the CEM is much faster than diffusion or turbulent mixing, leading to ignition. Additionally, projected chemical source term ( $\phi_\omega$ ) and non-chemical source (diffusion) term ( $\phi_s$ ) are shown in following equations [131]:

$$\phi_\omega = \mathbf{b}_e \cdot \boldsymbol{\omega}, \phi_s = \mathbf{b}_e \cdot \mathbf{s} \quad (5.3)$$

The ratio of  $\phi_s$  to  $\phi_\omega$  is defined as local combustion mode indicator  $\alpha$ :

$$\alpha = \phi_s / \phi_\omega \quad (5.4)$$

$\alpha$  describes three different local combustion mode: (1)  $\alpha > 1$  - the assisted-ignition mode where diffusion affects significantly; (2)  $|\alpha| < 1$  - the auto-ignition mode where reaction term is dominant; (3)  $\alpha < -1$  - the local extinction mode where the ignition process depressed by large amount of dissipation.

Figure 5.7 show the spatial distribution of  $Da_c$  for the cases and the black solid lines denote the  $Da_c = 1$  isoline. Note that the isoline of  $Da_c = 1$  is nearly identical to that of  $Y_{OH} = 0.001$  at the flamebase, and hence, the ignition characteristics near the flamebase can be elucidated. It is readily observed that, unlike the other cases,  $Da_c$  for Case Ig and H exhibit very large values in the two shear layers upstream of the flamebase, indicate that ignitable mixture condition generated by the enough hot coflow temperature. However, the absolute value of the maximum  $Da_c$  upstream of the flamebase for Case Ig is ten times larger than that of Case H.  $Da_c$  values of Case Ig and H imply that both cases have ignitable mixture condition upstream of the flamebase and hence, the fuel jet of Case Ig may be more apt to autoignite than that in Case H. For Cases L and M, however, only a narrow tip of large  $Da_c$  exists immediately upstream of the flamebase (see Figs. 5.7a and b). Since  $Da_c$  can also exhibit large values in the preheat zones of premixed flames [30–32], the narrow tips of large  $Da_c$  upstream of the flamebase demarcate the flame propagation characteristics of the flamebase rather than auto-ignition.

Analyzing  $\alpha$  is needed to understand ignition and propagation characteristics for Case H, Fig. 5.8 shows the spatial distribution of  $\alpha$  for the cases. The green area in color contour of  $\alpha$  indicates that  $\alpha$  is almost 0 because of the large quantity of  $\phi_\omega$  greater than  $\phi_s$ . A partly green area is observed at the shear layer located in upstream of flamebase in the Case of Ig. In the case of H, however, the red color area for  $\alpha$  contour is dominant at the upstream of flamebase. On the green color contour for the Case H at the tip of fuel nozzle where both  $\phi_s$  and  $\phi_\omega$  are almost 0 (i.e.  $O(-12)$  and  $O(-11)$  respectively), the 0 value of  $\alpha$  does not indicate ignition of mixture. Combustion mode indicator  $\alpha$  and the existence of the ignition kernel in both case Ig and H clearly show that the Case Ig has the ignition process at the upstream of flamebase, however, the ignition process is not found in the Case H despite having a relatively large  $Da_c$  at the flamebase.

Finally, important variables and reactions aligned with a CEM upstream of the flamebase were identified through the chemical explosive mode analysis (CEMA). From CEMA, the critical chemical kinetic processes occurring in the lifted jet flames can be elucidated by evaluating explosive index (**EI**) and participation index (**PI**) of local mixtures. **EI** and **PI** are defined as [31, 32, 102]:

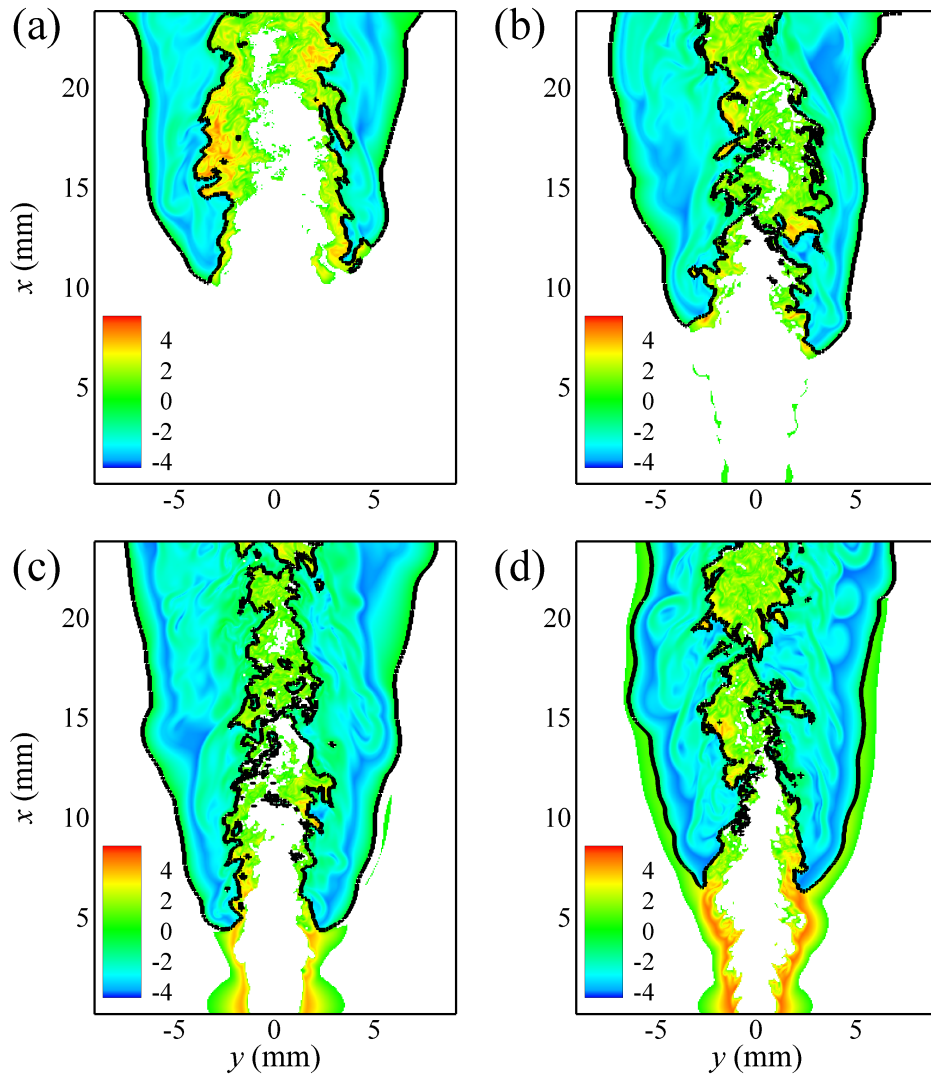


Figure 5.7:  $\text{sign}(\lambda_e) \times \log_{10}(\max(1, |Da_c|))$  of each case (a) Case L, (b) Case M, (c) Case H and (d) Case Ig.

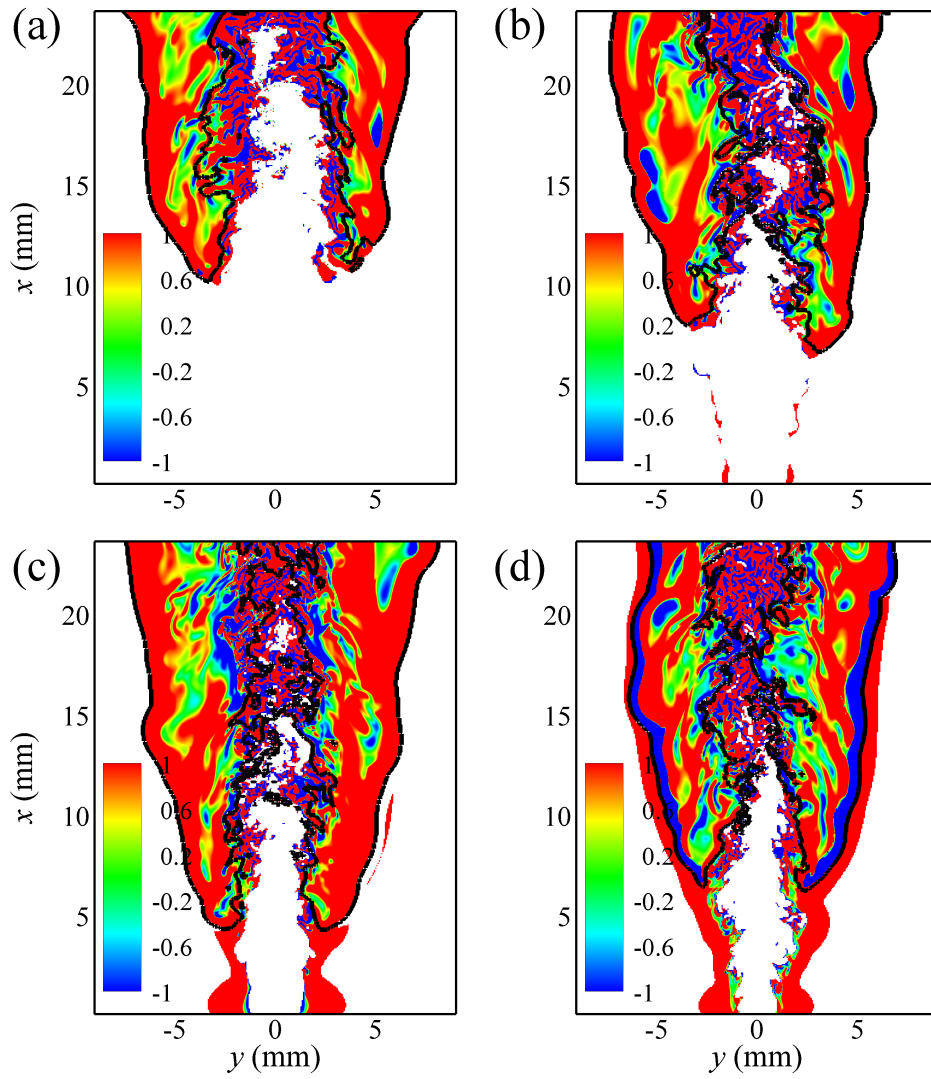


Figure 5.8: Combustion mode indicator  $\alpha$  of each case (a) Case L, (b) Case M, (c) Case H and (d) Case Ig.

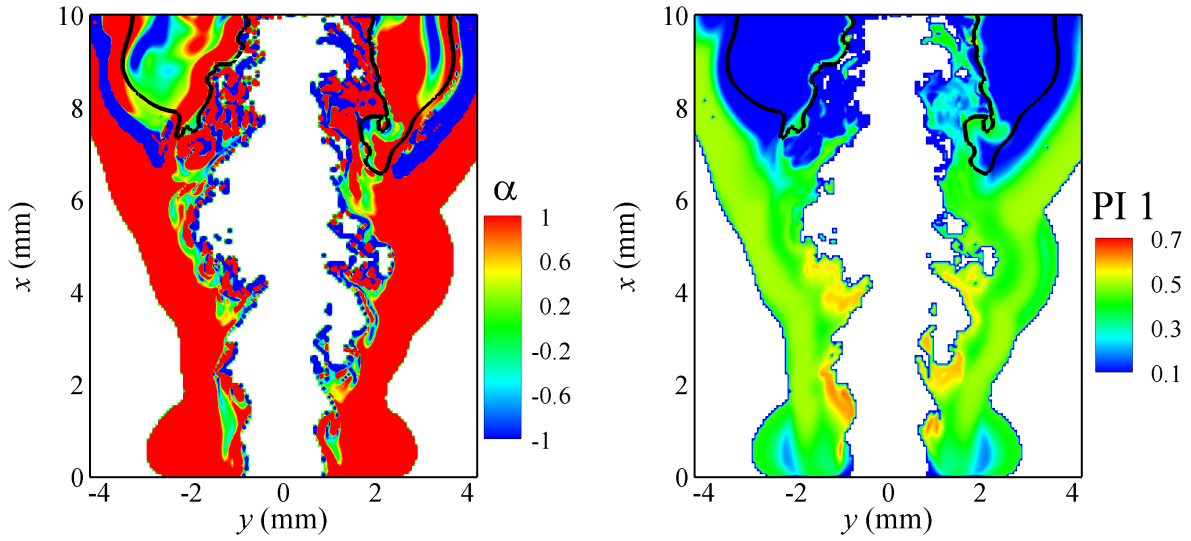


Figure 5.9: Combustion mode indicator  $\alpha$  and PI 1 of Case Ig black solid line indicates  $Y_{\text{OH}} = 0.001$

$$\mathbf{EI} = \frac{|\mathbf{a}_e \otimes \mathbf{b}_e^T|}{\sum |\mathbf{a}_e \otimes \mathbf{b}_e^T|}, \quad (5.5)$$

$$\mathbf{PI} = \frac{|(\mathbf{b}_e \cdot \mathbf{S}) \otimes \mathbf{R}|}{\sum |(\mathbf{b}_e \cdot \mathbf{S}) \otimes \mathbf{R}|}, \quad (5.6)$$

where  $\mathbf{S}$  and  $\mathbf{R}$  represent the stoichiometric coefficient matrix and the vector of the net rates for reactions, respectively. The symbol  $\otimes$  denotes the element-wise multiplication of two vectors.  $\mathbf{EI}$  and  $\mathbf{PI}$  indicate the normalized contribution of each variable and reaction to a CEM, respectively, and as such, key species and reactions to ignition near the flamebase can be elucidated by evaluating EI and PI values.

Figure 5.9 shows the PI isocontours of important reaction and  $\alpha$  for the lifted flame in Case Ig. PI of R1 which is one of the keychain branching reactions  $\text{O}_2 + \text{H} \rightarrow \text{O} + \text{OH}$ , which initiates the  $\text{H}_2/\text{O}_2$  mixture combustion process by generating radical pool, is a large portion of the CEM in the overall reactions. R1 is the endothermic reaction and is not favored at low temperatures.

Figure 5.10 shows the EI H isocontours of Case Ig and H. EI of H for Case Ig has large value compared to the Case H. The areas where PI of R1 is a large and greenish region

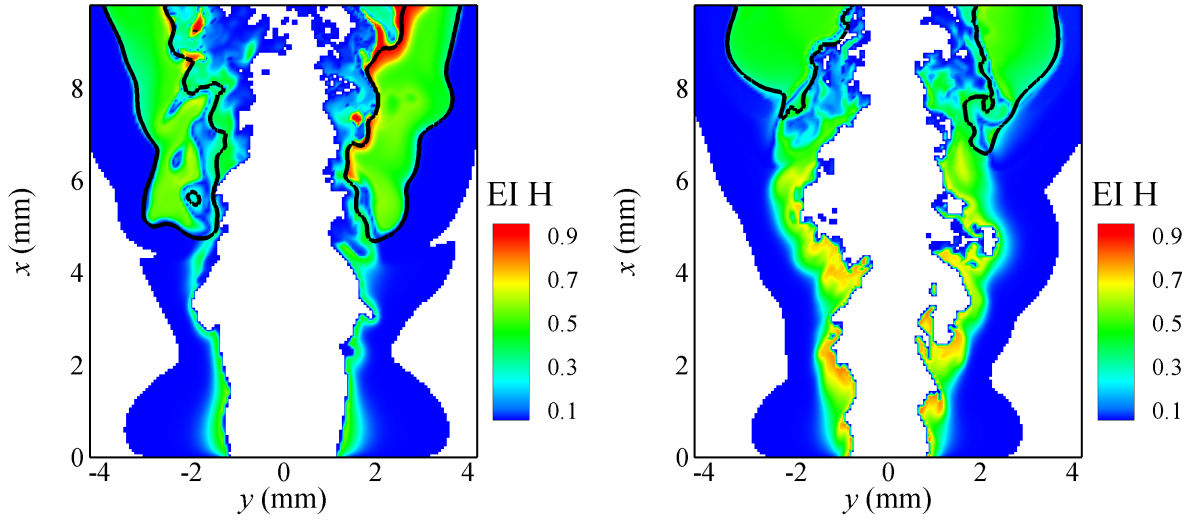


Figure 5.10: EI of H for Case H (left) and Ig (right) at the upstream of flamebase, black solid line indicates  $Y_{OH} = 0.001$

of the color contour  $\alpha$  overlap each other. This result indicates that ignitable mixtures of Case Ig at the upstream of flamebase has the sufficiently large temperature for initiating overall combustion process and this condition activates chain branching reaction R1 which has a large portion in CEM. It is in line with the aforementioned  $Da_c$  and  $\alpha$  analysis and the existence of ignition kernel in the Case Ig. In Case H, however, the PI of R1 has small value compared to the value of the Case Ig and  $\alpha$  of this area is greater than 1. This implies that the 950 K coflow temperature generates explosive condition ( $Da_c > 1$ ) and the chain branching reaction can be initiated by its coflow temperature but the ignition can not be sustained and ignition kernels does not be generated.

Figure 5.11 shows the  $S_d^R$  for Case Ig and H at the upstream of flamebase. In Case of Ig,  $S_d^R$  has a meaningful value at the upstream of flamebase compared to the Case H. Reaction part of displacement color contour indicates that chemical kinetics related to initiating overall combustion process activated in Case Ig at the upstream of flamebase.

## 5.4 Conclusions

The flame structure characteristics and stabilization mechanisms of turbulent lifted hydrogen jet flames with four different coflow temperatures of  $T_c = 750, 850, 950$  K and

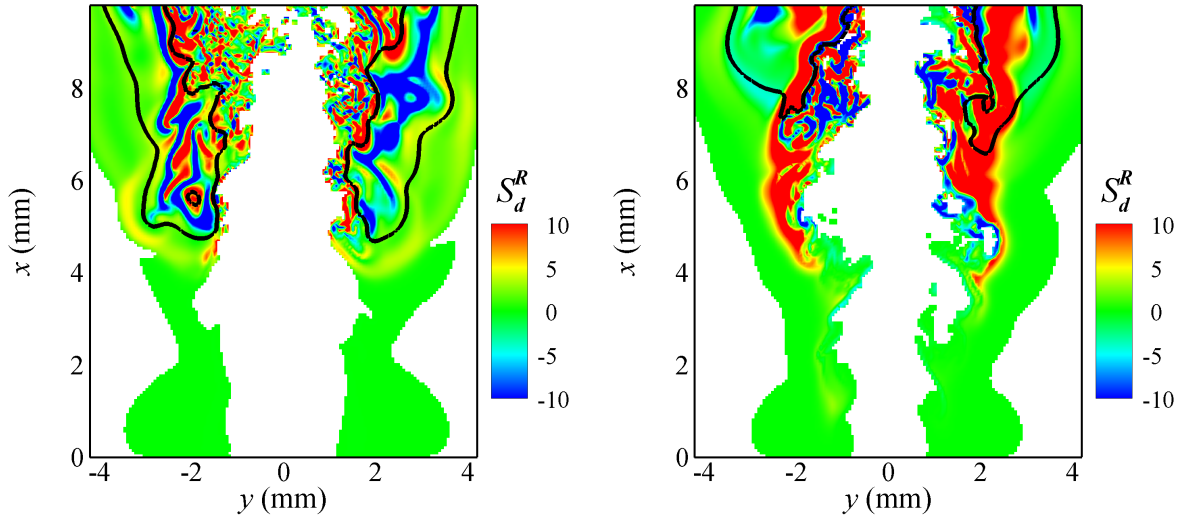


Figure 5.11:  $S_d^R$  for Case H (left) and Ig (right) at the upstream of flamebase, black solid line indicates  $Y_{OH} = 0.001$

1100 K were investigated using 3-D DNSs with a detailed hydrogen/air kinetic mechanism. The DNSs were performed at a jet Reynolds number of 8,000 (Case L, M and H) and 10,000 (Case Ig) based on the fuel jet with over 1 billion grid points. The results show that the lift-off height decreases with increasing  $T_c$  in same  $Re_j$ , consistent with previous experiments [107,127,130]. For Cases L, M, and H, it was found from the axial variations of  $\langle \dot{q}|\eta \rangle$  that high  $T_c$  enhances combustion even in fuel-rich mixtures by reducing the lift-off height. Moreover, vigorous heat is released within a jet width downstream of the flamebase and  $\langle \dot{q}|\eta \rangle$  exhibits two peaks located at stoichiometric and fuel-rich mixtures further downstream of the flamebase, similar to the Case of Ig. It was also found that at the flamebase,  $\langle \dot{D}a|\eta \rangle$  exhibits  $O(\gg 1)$  values for Case H with  $T_c = 950$  K and  $\sim O(1)$  for Case L with  $T_c = 750$  K, which implies that the stabilization mechanism of the turbulent lifted jet flames may be affected by auto-ignition with high  $T_c$ . It was revealed from the displacement speed analysis that the turbulent lifted flames with coflow temperature of  $T_c = 750$  K, 850 K and 950 K have similar temporal evolution of  $z$ -plane averaged  $S_d$ , although 950 K has relatively large value of  $S_d$  in  $z = 1$  plane. In Case of Ig,  $z$ -plane averaged  $S_d$  values are higher than other cases in all time and extremely large value of  $S_d$  was captured in temporal evolution of  $z = 1$   $S_d$  graph at certain time when ignition kernel occurs at the upstream of flamebase. Finally, important variables and reactions

aligned with a CEM upstream of the flamebase were identified through the chemical explosive mode analysis (CEMA).  $Da_c$  and combustion mode indicator  $\alpha$  were introduced to identify stabilization mechanisms of each case. Case L and M have narrow tip of large  $Da_c$  at the flamebases and  $\alpha$  shows their combustion mode at the upstream of flamebase is governed by diffusion source not the auto-ignition. Case H and Ig have long stripe line of  $Da_c$  pattern at the upstream of flamebase which implies that ignitable mixture condition may affect overall combustion process at the upstream of the flamebase. In Case Ig, auto-ignition combustion mode was captured at the upstream of the flamebase where chain branching reaction and key radicals participating in this reaction are a large part of the CEM (large EI of H and PI of R1). In Case of H, however, relatively high  $Da_c$  does not lead to actual ignition process at the upstream of flamebase. This argument is supported by analysis of  $S_d^R$  at the flamebase.  $S_d^R$  of Case Ig has a meaningfully large value at the upstream of flamebase but not in Case H. In summary, lifted flame with low coflow temperature stabilized by propagation. Relatively high coflow temperature generates ignitable mixture condition and chain branching reaction can be activated but stabilization mechanism is similar to the low coflow temperature. Sufficiently large coflow temperature makes actual ignition at the upstream of flamebase and it affects the stabilization mechanism of lifted flame (Case Ig).



# Chapter VI

## Conclusion

This thesis focuses on the combustion characteristics on LTC condition in HCCI engines, laminar and turbulent lifted flames. HCCI combustion with thermal stratification is systematically investigated using direct numerical simulations (DNS). The laminar and turbulent lifted jet flames also investigated with DNSs. These simulations allow better understandings of the ignition process (i.e. combustion modes, flame speed, turbulence-chemistry interactions) of different fuels and configurations under the LTC condition.

The key findings of the thesis on the combustion characteristics of LTC are summarized as follows

- In HCCI engine DNSs, the temperature stratification reduces excessive HRR and advances the overall combustion. The fuel composition differences of the ignition characteristics of PRF/air mixtures vanish with increasing thermal inhomogeneities. The nearly identical propagation characteristics of deflagrations of different PRF/air mixtures is the cause of vanishing of the fuel effect under the high degree of thermal inhomogeneities.
- The ignition Damköhler number,  $Da_{ig}$ , was introduced to evaluate the effects of turbulence on the early evolution of deflagrations from ignition kernels. For cases with  $Da_{ig} \lesssim O(1)$ , the overall combustion is retarded and more apt to occur by spontaneous ignition. For cases with  $Da_{ig} \gg O(1)$ , however, turbulence with large  $u'$  can advance the overall combustion by increasing turbulent flame area.

- In methane/hydrogen jet laminar lifted jet flames, the flame structure and  $(T_{\max} - T_0)/T_{\text{ig}}$ , we can categorized the autoignited into three different combustion regimes under LTHH condition: the MILD combustion, transition, and tribrachial edge flame regimes.
- The high diffusive nature of hydrogen molecules is primarily attributed to the unusual decreasing  $H_L$  behavior with increasing  $U_0$  under the LTHH condition.
- In the MILD combustion regime under the LTHH condition, hydrogen molecules in the fuel jet have enough time to diffuse out from the center, and hence, local temperature increase by autoignition is relatively reduced compared to that in the tribrachial edge flame regime. In the tribrachial edge flame regime, however, the flamebase locates radially outside and more hydrogen molecules can diffuse into the flamebase. The local temperature increase by autoignition is relatively enhanced. These difference of temperature field characteristics lead to the decrease of  $H_L$  with increasing  $U_0$ .
- The stabilization of the autoignited lifted methane/hydrogen jet flames is affected by both autoignition and flame propagation. The role of flame propagation on their stabilization increases with increasing  $U_0$ : a lifted flame in the MILD combustion regime is primarily stabilized by autoignition while it in the tribrachial edge flame regime is stabilized by autoignition-assisted flame propagation.
- In *n*-heptane jet flames, it was identified that the propagation speed of tribrachial edge flame is almost similar to the laminar burning velocity and  $S_e$  at the flamebase for MILD combustion is larger than that of  $S_L$ .
- The stabilization mechanism of tribrachial edge flame is normal flame propagation. MILD combustion regime, however, the broad thermal cooking region and relatively high  $S_e/S_L$  suggest that ignition affects the overall flame stabilization at the upstream of flamebase.
- In the turbulent lifted hydrogen jet flames with 4 different coflow temperatures, the lift-off height decreases with increasing  $T_c$  in same  $Re_j$ . The high  $T_c$  enhances

combustion even in fuel-rich mixtures by reducing the lift-off height for the case  $T_c = 750$  K to 950 K.

- The stabilization mechanism of the turbulent lifted jet flames may be affected by auto-ignition with high  $T_c$ .  $Da_c$  of case H has a large value at the upstream of flamebase, however, the displacement speed of  $T_c = 750$  K, 850 K and 950 K have similar for  $z$ -plane averaged value, although 950 K has relatively large value of  $S_d$  in  $z = 1$  plane. In Case of  $T_c = 1100$  K, the ignition kernel occurs at the upstream of flamebase and overall  $S_d$  is larger than the other cases.
- $Da_c$  and combustion mode index  $\alpha$  were introduced to identify stabilization mechanisms of each case. Stabilization mechanisms of Case  $T_c = 750$  and 850 K are governed by diffusion source. Case  $T_c = 1100$  K auto-ignition combustion mode was captured at the upstream of the flamebase. In Case of  $T_c = 950$  K relatively high  $Da_c$  does not lead to actual ignition process at the upstream of flamebase.

## 6.1 Future Work

Although fundamental studies on LTC has been conducted, which has shown stabilization mechanisms and combustion characteristics in several combustion configurations, additional research and development are needed so that these LTC concepts can become viable. The present study focuses simple combustion geometry such as the square domain of HCCI condition combustion and lifted jet flames. However, for applying LTC to practical engineering problems, the real size engine simulations are conducted under various conditions. LTC has explored new combustion regimes, which have not previously been considered in model development or validation. Particularly, these advanced combustion engines are operated under ultra-lean, highly-diluted, partially premixed, and elevated pressure, low-temperature conditions. The real size LTC simulations can help to reduce the number of experiments by providing efficient way of controlling parameters. The details of experimental data are often not sufficient for understanding results of LTC experiments. Therefore, the demand for accurate real size LTC simulations is higher than

ever. the present study could be extended to the following research directions.

- OpenFOAM will be used in large scale combustion simulations of LTC combustion system. large scale LTC engine simulations will be performed with a moving mesh. Time dependent transient solver will be chosen to reproduce the compression and expansion procedure in LTC engines.
- A modification of chemical reaction mechanisms will be conducted. In large scale engine simulations, computational cost will be reduced by adopting small size of chemical reactions which is accurate at LTC condition. Global pathway selection (GPS) [134] is one of the options of mechanism reduction.
- By performing OpenFOAM-based LTC engine simulations with a realistic geometry, we can elucidate realistic combustion procedures. Optimization of fuel composition, amount of fuel to be injected, injection timing and ignition time can be achieved.
- Finally, the available DNS dataset of LTC can be used for the development of LTC system using OpenFOAM.

## References

- [1] A. McIlroy, G. McRae, V. Sick, D. L. Siebers, C. K. Westbrook, P. J. Smith, C. Taatjes, A. Trouve, A. F. Wagner, E. Rohlfing, D. Manley, F. Tully, R. Hilderbrandt, W. Green, D. Marceau, J. O’Neal, M. Lyday, F. Cebulski, T. R. Garcia, and D. Strong, “Basic research needs for clean and efficient combustion of 21st century transportation fuels,” *US Department of Energy Report*, p. <https://www.osti.gov/scitech/servlets/purl/935428>, 2006.
- [2] B. C. Choi and S. H. Chung, “Autoignited laminar lifted flames of methane/hydrogen mixtures in heated coflow air,” *Combust. Flame*, vol. 159, pp. 1481–1488, 2012.
- [3] G. P. Smith, D. M. Golden, M. Frenklach, N. W. Moriarty, B. Eiteneer, M. Goldenberg, C. T. Bowman, R. K. Hanson, S. Song, W. C. Gardiner, V. V. Lissianski, and Z. Qin, “GRI-Mech 3.0,” <http://combustion.berkeley.edu/gri-mech>.
- [4] San Diego Mechanism web page, Mechanical and Aerospace Engineering (Combustion Research), University of California at San Diego, “Chemical-kinetic mechanisms for combustion applications,” <http://combustion.ucsd.edu>.
- [5] H. Wang, X. You, A. V. Joshi, S. G. Davis, A. Laskin, F. Egolfopoulos, and C. K. Law, “USC Mech Version II. High-Temperature Combustion Reaction Model of H<sub>2</sub>/CO/C1-C4 Compounds,” [http://ignis.usc.edu/USC\\\_Mech\\\_II.htm](http://ignis.usc.edu/USC\_Mech\_II.htm).
- [6] E. L. Petersen, D. M. Kalitan, S. Simmons, G. Bourque, H. J. Curran, and J. M. Simmie, “Methane/Propane oxidation at high pressures: experimental and detailed chemical kinetic modelling,” *Proc. Combust. Inst.*, vol. 31, pp. 447–454, 2007.

- [7] A. A. Konnov, “Implementation of the NCN pathway of prompt-NO formation in the detailed reaction mechanism,” *Combust. Flame*, vol. 156, pp. 2093–2105, 2009.
- [8] J. E. Dec, “A conceptual model of di diesel combustion based on laser-sheet imaging\*,” vol. 106, pp. 1319–1348, 02 1997. [Online]. Available: <https://doi.org/10.4271/970873>
- [9] T. Kitamura, T. Ito, J. Senda, and H. Fujimoto, “Mechanism of smokeless diesel combustion with oxygenated fuels based on the dependence of the equivalence ration and temperature on soot particle formation,” *Int. J. Engine Res.*, vol. 3, pp. 223–248, 2002.
- [10] S. Kook, C. Bae, P. C. Miles, D. Choi, and L. M. Pickett, “The influence of charge dilution and injection timing on low-temperature diesel combustion and emissions,” *SAE paper*, pp. 2005–01–3837, 2005.
- [11] J. E. Dec, “Advanced compression-ignition engines—understanding the in-cylinder processes,” *Proc. Combust. Inst.*, vol. 32, pp. 2727–2742, 2009.
- [12] F. Zhao, T. W. Asmus, D. N. Assanis, J. E. Dec, J. A. Eng, and P. M. Najt, *Homogeneous Charge Compression Ignition (HCCI) Engines: Key Research and Development Issues*, illustrated edition ed. SAE International, 2003.
- [13] H. Zhao, Ed., *HCCI and CAI Engines for the Automotive Industry*, 1st ed. Elsevier, 2007.
- [14] M. Yao, Z. Zheng, and H. Liu, *Prog. Energy Combust. Sci.*, vol. 35, pp. 398–437, 2009.
- [15] X. Lü, D. Han, and Z. Huang, *Prog. Energy Combust. Sci.*, vol. 37, pp. 741–783, 2011.
- [16] S. Saxena and I. D. Bedoya, “Fundamental phenomena affecting low temperature combustion and HCCI engines, high load limits and strategies for extending these limits,” *Prog. Energy Combust. Sci.*, vol. 39, pp. 457–488, 2013.

- [17] B. Johansson, “Fuels and combustion,” in *Biofuels from Lignocellulosic Biomass: Innovations beyond Bioethanol*, M. Boot, Ed. Wiley-VCH Verlag GmbH & Co. KGaA, 2016, pp. 1–27.
- [18] A. K. Agarwal, A. P. Singh, and R. K. Maurya, “Evolution, challenges and path forward for low temperature combustion engines,” *Prog. Energy Combust. Sci.*, vol. 61, pp. 1–56, 2017.
- [19] N. Peters, *Turbulent combustion*. Cambridge University Press, 2000.
- [20] L. M. Pickett, “Low flame temperature limits for mixing-controlled Diesel combustion,” *Proc. Combust. Inst.*, vol. 30, pp. 2727–2735, 2005.
- [21] N. Peters, “Laminar diffusion flamelet models in non-premixed turbulent combustion,” *Progress in Energy and Combustion Science*, vol. 10, no. 3, pp. 319 – 339, 1984. [Online]. Available: <http://www.sciencedirect.com/science/article/pii/036012858490114X>
- [22] A. Cavaliere and M. de Joannon, “Mild combustion,” *Prog. Energy Combust. Sci.*, vol. 30, pp. 329–366, 2004.
- [23] S. K. Choi and S. H. Chung, “Autoignited and non-autoignited lifted flames of pre-vaporized n-heptane in coflow jets at elevated temperatures,” *Combust. Flame*, vol. 160, pp. 1717–1724, 2013.
- [24] S. M. Al-Noman, S. K. Choi, and S. H. Chung, “Autoignition characteristics of laminar lifted jet flames of pre-vaporized iso-octane in heated coflow air,” *Fuel*, vol. 162, pp. 171–178, 2015.
- [25] B. C. Choi and S. H. Chung, “Autoignited laminar lifted flames of methane, ethylene, ethane, and n-butane jets in coflow air with elevated temperature,” *Combust. Flame*, vol. 157, pp. 2348–2356, 2010.
- [26] S. M. Al-Noman, B. C. Choi, and S. H. Chung, “Autoignited lifted flames of dimethyl ether in heated coflow air,” *Combust. Flame*, vol. 195, pp. 75–83, 2018.

- [27] J. E. Dec, W. Hwang, and M. Sjöberg, *SAE Trans.*, pp. 2006-01-1518, 2006.
- [28] M. B. Luong, T. Lu, S. H. Chung, and C. S. Yoo, *Combust. Flame*, vol. 161, pp. 2878–2889, 2014.
- [29] M. de Joannon, A. Saponaro, and A. Cavaliere, “Zero-dimensional analysis of methane diluted oxidation in rich conditions,” *Proc. Combust. Inst.*, vol. 28, pp. 1639—1646, 2000.
- [30] T. F. LU, C. S. YOO, J. H. CHEN, and C. K. LAW, “Three-dimensional direct numerical simulation of a turbulent lifted hydrogen jet flame in heated coflow: a chemical explosive mode analysis,” *Journal of Fluid Mechanics*, vol. 652, p. 45–64, 2010.
- [31] Z. Luo, C. S. Yoo, E. S. Richardson, J. H. Chen, C. K. Law, and T. Lu, “Chemical explosive mode analysis for a turbulent lifted ethylene jet flame in highly-heated coflow,” *Combustion and Flame*, vol. 159, no. 1, pp. 265 – 274, 2012. [Online]. Available: <http://www.sciencedirect.com/science/article/pii/S0010218011001696>
- [32] R. Shan, C. S. Yoo, J. H. Chen, and T. Lu, “Computational diagnostics for n-heptane flames with chemical explosive mode analysis,” *Combustion and Flame*, vol. 159, no. 10, pp. 3119 – 3127, 2012. [Online]. Available: <http://www.sciencedirect.com/science/article/pii/S0010218012001770>
- [33] R. Reitz, *Combust. Flame*, vol. 160, pp. 1–8, 2013.
- [34] A. Hultqvist, M. Christenson, B. Johansson, M. Richter, J. Nygren, J. Hult, and M. Alden, *SAE paper*, pp. 2002-01-0424, 2002.
- [35] J. A. Eng, *SAE paper*, pp. 2002-01-2859, 2002.
- [36] A. Babajimopoulos, G. A. Lavoie, and D. N. Assanis, *SAE paper*, pp. 2003-01-3220, 2003.
- [37] M. Sjöberg and J. E. Dec, *SAE Trans. paper*, vol. 115, pp. 318–334, 2006.



- [38] J. E. Dec and W. Hwang, *SAE Trans. paper*, pp. 2009–01–0650, 2009.
- [39] Y. Yang, J. E. Dec, N. Dronniou, and M. Sjöberg, *Proc. Combust. Inst.*, vol. 33, pp. 3047–3055, 2011.
- [40] Y. Yang, J. Dec, N. Dronniou, M. Sjöberg, and W. Cannella, *SAE paper*, pp. 2011–01–1359, 2011.
- [41] A. Krisman, E. R. Hawkes, S. Kook, M. Sjöberg, and J. E. Dec, *Fuel*, vol. 99, pp. 45–54, 2012.
- [42] R. Sankaran, H. G. Im, E. R. Hawkes, and J. H. Chen, *Proc. Combust. Inst.*, vol. 30, pp. 875–882, 2005.
- [43] J. H. Chen, E. R. Hawkes, R. Sankaran, S. D. Mason, and H. G. Im, “Direct numerical simulation of ignition front propagation in a constant volume with temperature inhomogeneities I. Fundamental analysis and diagnostics,” *Combust. Flame.*, vol. 145, pp. 128–144, 2006.
- [44] E. R. Hawkes, R. Sankaran, P. Pébay, and J. H. Chen, *Combust. Flame*, vol. 145, pp. 145–159, 2006.
- [45] G. Bansal and H. G. Im, *Combust. Flame*, vol. 158, pp. 2105–2112, 2011.
- [46] R. Yu and X.-S. Bai, *Combust. Flame*, vol. 160, pp. 1706–1716, 2013.
- [47] H. A. El-Asrag and Y. Ju, *Combust. Theory Modelling*, vol. 17, pp. 316–334, 2013.
- [48] —, *Combust. Flame*, vol. 161, pp. 256–269, 2014.
- [49] C. S. Yoo, T. Lu, J. H. Chen, and C. K. Law, “Direct numerical simulations of ignition of a lean n-heptane/air mixture with temperature inhomogeneities at constant volume: Parametric study,” *Combustion and Flame*, vol. 158, no. 9, pp. 1727 – 1741, 2011. [Online]. Available: <http://www.sciencedirect.com/science/article/pii/S001021801100040X>

- [50] C. S. Yoo, Z. Luo, T. Lu, H. Kim, and J. H. Chen, “A dns study of ignition characteristics of a lean iso-octane/air mixture under hcci and saci conditions,” *Proceedings of the Combustion Institute*, vol. 34, no. 2, pp. 2985 – 2993, 2013. [Online]. Available: <http://www.sciencedirect.com/science/article/pii/S154074891200020X>
- [51] M. B. Luong, Z. Luo, T. Lu, S. H. Chung, and C. S. Yoo, *Combust. Flame*, vol. 160, pp. 2038–2047, 2013.
- [52] A. Bhagatwala, T. Lu, and J. H. Chen, *Combust. Flame*, vol. 161, pp. 1826–1841, 2014.
- [53] J. H. Chen, A. Choudhary, B. de Supinski, M. DeVries, E. R. Hawkes, S. Klasky, W. K. Liao, K. L. Ma, J. Mellor-Crummey, N. Podhorszki, R. Sankaran, S. Shende, and C. S. Yoo, “Terascale direct numerical simulations of turbulent combustion using s3d,” *Computational Science & Discovery*, vol. 2, no. 1, p. 015001, jan 2009. [Online]. Available: <https://doi.org/10.1088%2F1749-4699%2F2%2F1%2F015001>
- [54] J. H. Chen, *Proc. Combust. Inst.*, vol. 33, pp. 99–123, 2011.
- [55] C. A. Kennedy, M. H. Carpenter, and R. M. Lewis, *Appl. Num. Math.*, vol. 35, pp. 117–219, 2000.
- [56] C. A. Kennedy and M. H. Carpenter, *Appl. Num. Math.*, vol. 14, pp. 397–433, 1994.
- [57] H. J. Curran, P. Gaffuri, W. J. Pitz, and C. K. Westbrook, *Combust. Flame*, vol. 129, pp. 253–280, 2002.
- [58] —, *Combust. Flame*, vol. 114, pp. 149–177, 1998.
- [59] T. Lu and C. K. Law, *Proc. Combust. Inst.*, vol. 31, pp. 1333–1341, 2005.
- [60] —, *Combust. Flame*, vol. 148, pp. 117–126, 2007.
- [61] —, *Combust. Flame*, vol. 154, pp. 153–163, 2008.

- [62] T. Lu, C. K. Law, C. S. Yoo, and J. H. Chen, *Combust. Flame*, vol. 156, pp. 1542–1551, 2009.
- [63] C. S. Yoo, Y. Wang, A. Trouvé, and H. G. Im, “Characteristic boundary conditions for direct simulations of turbulent counterflow flames,” *Combustion Theory and Modelling*, vol. 9, no. 4, pp. 617–646, 2005. [Online]. Available: <https://doi.org/10.1080/13647830500307378>
- [64] C. S. Yoo and H. G. Im, “Characteristic boundary conditions for simulations of compressible reacting flows with multi-dimensional, viscous and reaction effects,” *Combustion Theory and Modelling*, vol. 11, no. 2, pp. 259–286, 2007. [Online]. Available: <https://doi.org/10.1080/13647830600898995>
- [65] —, “Transient soot dynamics in turbulent nonpremixed ethylene–air counterflow flames,” *Proceedings of the Combustion Institute*, vol. 31, no. 1, pp. 701 – 708, 2007. [Online]. Available: <http://www.sciencedirect.com/science/article/pii/S1540748906003531>
- [66] W. Hwang, J. E. Dec, and M. Sjöberg, *SAE Trans. paper*, vol. 116, pp. 2007–01–4130, 2007.
- [67] S. L. Kokjohn, R. M. Hanson, D. A. Splitter, and R. D. Reitz, *Int. J. Engine Res.*, pp. 209–226, 2011.
- [68] S. B. Pope, *Turbulent flows*. Cambridge University Press, 2000.
- [69] S. Tanaka, F. Ayala, J. C. Keck, and J. B. Heywood, *Combust. Flame*, vol. 132, pp. 219–239, 2003.
- [70] C. K. Law, *Combustion Physics*. Cambridge University Press, 2006.
- [71] C. S. YOO, R. SANKARAN, and J. H. CHEN, “Three-dimensional direct numerical simulation of a turbulent lifted hydrogen jet flame in heated coflow: flame stabilization and structure,” *Journal of Fluid Mechanics*, vol. 640, p. 453–481, 2009.

- [72] T. Lu, C. S. Yoo, J. H. Chen, and C. K. Law, *J. Fluid Mech.*, vol. 652, pp. 45–64, 2010.
- [73] C. S. Yoo, E. S. Richardson, R. Sankaran, and J. H. Chen, “A dns study on the stabilization mechanism of a turbulent lifted ethylene jet flame in highly-heated coflow,” *Proceedings of the Combustion Institute*, vol. 33, no. 1, pp. 1619 – 1627, 2011. [Online]. Available: <http://www.sciencedirect.com/science/article/pii/S154074891000310X>
- [74] R. Grout, A. Gruber, C. Yoo, and J. Chen, “Direct numerical simulation of flame stabilization downstream of a transverse fuel jet in cross-flow,” *Proceedings of the Combustion Institute*, vol. 33, no. 1, pp. 1629 – 1637, 2011. [Online]. Available: <http://www.sciencedirect.com/science/article/pii/S1540748910000192>
- [75] H. Kolla, R. W. Grout, A. Gruber, and J. H. Chen, “Mechanisms of flame stabilization and blowout in a reacting turbulent hydrogen jet in cross-flow,” *Combustion and Flame*, vol. 159, no. 8, pp. 2755 – 2766, 2012, special Issue on Turbulent Combustion. [Online]. Available: <http://www.sciencedirect.com/science/article/pii/S0010218012000260>
- [76] R. Borghi, *Prog. Energy Combust. Sci.*, vol. 14, pp. 245–292, 1988.
- [77] C. S. Yoo and H. G. Im, *Proc. Combust. Inst.*, vol. 30, pp. 349–356, 2005.
- [78] C. S. Yoo, J. H. Chen, and J. H. Frank, *Combust. Flame*, vol. 156, pp. 140–151, 2009.
- [79] D. J. Cook, H. Pitch, J. H. Chen, and E. R. Hawkes, *Proc. Combust. Inst.*, vol. 31, pp. 2903–2911, 2007.
- [80] F. Bisetti, J.-Y. Chen, J. H. Chen, and E. R. Hawkes, *Combust. Flame*, vol. 155, pp. 571–584, 2008.
- [81] F. Salehi, M. Talei, E. R. Hawkes, C. S. Yoo, T. Lucchini, G. D’Errico, and S. Kook, *Proc. Combust. Inst.*, pp. in press, <http://dx.doi.org/10.1016/j.proci.2014.05.035>, 2014.

- [82] R. D. Reitz and G. Duraisamy, “Review of high efficiency and clean reactivity controlled compression ignition (RCCI) combustion in internal combustion engines,” *Prog. Energy Combust. Sci.*, vol. 46, pp. 12–71, 2015.
- [83] M. B. Luong, T. Lu, S. H. Chung, and C. S. Yoo, “Direct numerical simulations of the ignition of a lean biodiesel/air mixture with temperature and composition inhomogeneities at high pressure and intermediate temperature,” *Combustion and Flame*, vol. 161, no. 11, pp. 2878 – 2889, 2014. [Online]. Available: <http://www.sciencedirect.com/science/article/pii/S0010218014001345>
- [84] M. B. Luong, G. H. Yu, T. Lu, S. H. Chung, and C. S. Yoo, “Direct numerical simulations of ignition of a lean n-heptane/air mixture with temperature and composition inhomogeneities relevant to HCCI and SCCI combustion,” *Combust. Flame*, vol. 162, pp. 4566–4585, 2015.
- [85] M. B. Luong, G. H. Yu, S. H. Chung, and C. S. Yoo, “Ignition of a lean PRF/air mixture under RCCI/SCCI conditions: A comparative DNS study,” *Proc. Combust. Inst.*, vol. 36, pp. 3623–3631, 2017.
- [86] M. B. Luong, R. Sankaran, G. H. Yu, S. H. Chung, and C. S. Yoo, “On the effect of injection timing on the ignition of lean PRF/air/EGR mixtures under direct dual fuel stratification conditions,” *Combust. Flame*, vol. 183, pp. 309–321, 2017.
- [87] B. C. Choi, K. N. Kim, and S. H. Chung, “Autoignited laminar lifted flames of propane in coflow jets with tribrachial edge and mild combustion,” *Combust. Flame*, vol. 156, pp. 396–404, 2009.
- [88] S. M. Al-Noman, S. K. Choi, and S. H. Chung, “Numerical study of laminar non-premixed methane flames in coflow jets: Autoignited lifted flames with tribrachial edges and MILD combustion at elevated temperatures,” *Combust. Flame*, vol. 171, pp. 119–132, 2016.

- [89] A. Cuoci, A. Frassoldati, T. Faravelli, and E. Ranzi, “A computational tool for the detailed kinetic modeling of laminar flames: application to  $C_2H_4/CH_4$  coflow flames,” *Combust. Flame*, vol. 160, pp. 870–886, 2013.
- [90] —, “Numerical modeling of laminar flames with detailed kinetics based on the operator-splitting method,” *Energy Fuels*, vol. 27, pp. 7730–7753, 2013.
- [91] H. G. Weller, G. Tabor, H. Jasak, and C. Fureby, “A tensorial approach to computational continuum mechanics using object-oriented techniques,” *Comput. Phys.*, vol. 12, pp. 620–631, 1998.
- [92] R. J. Kee, F. M. Rupley, E. Meeks, and J. A. Miller, “CHEMKIN-III: a fortran chemical kinetics package for the analysis of gas-phase chemical and plasma kinetics,” *SAND96-8216*, 1996.
- [93] S. K. Choi, S. Al-Noman, and S. H. Chung, “Simulation of non-autoignited and autoignited laminar non-premixed jet flames of syngas in heated coflow air,” *Combust. Sci. Technol.*, vol. 187, pp. 132–147, 2015.
- [94] R. Bilger, “The structure of turbulent nonpremixed flames,” *Symposium (International) on Combustion*, vol. 22, no. 1, pp. 475 – 488, 1989. [Online]. Available: <http://www.sciencedirect.com/science/article/pii/S0082078489800542>
- [95] E. Mastorakos, “Ignition of turbulent non-premixed flames,” *Progress in Energy and Combustion Science*, vol. 35, no. 1, pp. 57 – 97, 2009. [Online]. Available: <http://www.sciencedirect.com/science/article/pii/S0360128508000415>
- [96] Y. C. Chen and R. W. Bilger, “Stabilization mechanisms of lifted laminar flames in axisymmetric jet flows,” *Combust. Flame*, vol. 123, pp. 23–45, 2000.
- [97] Y. Xue and Y. Ju, “Studies on the liftoff properties of dimethyl ether jet diffusion flames,” *Combust. Sci. Technol.*, vol. 178, pp. 2219–2247, 2006.
- [98] K. Gkagkas and R. P. Lindstedt, “Transported PDF modelling with detailed chemistry of pre- and auto-ignition in  $CH_4$ /air mixtures,” *Proc. Combust. Inst.*, vol. 31, pp. 1559–1566, 2007.

- [99] R. L. Gordon, A. R. Masri, and E. Mastorakos, “Heat release rate as represented by  $[\text{OH}] \times [\text{CH}_2\text{O}]$  and its role in autoignition,” *Combust. Theory Model.*, vol. 13, pp. 645–670, 2009.
- [100] Y. Minamoto, N. Swaminathan, R. S. Cant, and T. Leung, “Reaction zones and their structure in MILD combustion,” *Combust. Sci. Technol.*, vol. 186, pp. 1075–1096, 2014.
- [101] Z. Chen, V. M. Reddy, S. Ruan, N. A. K. Doan, W. L. Roberts, and N. Swaminathan, “Simulation of MILD combustion using perfectly stirred reactor model,” *Proc. Combust. Inst.*, vol. 36, pp. 4279–4286, 2017.
- [102] M. B. Luong, G. H. Yu, S. H. Chung, and C. S. Yoo, “Ignition of a lean prf/air mixture under rcci/scici conditions: Chemical aspects,” *Proceedings of the Combustion Institute*, vol. 36, no. 3, pp. 3587 – 3596, 2017. [Online]. Available: <http://www.sciencedirect.com/science/article/pii/S1540748916301341>
- [103] A. Lifshitz, K. Scheller, A. Burcat, and G. B. Skinner, “Shock-tube investigation of ignition in methane-oxygen-argon mixtures,” *Combust. Flame.*, vol. 16, pp. 311–321, 1971.
- [104] Y. Ju and T. Niioka, “Ignition simulation of methane/hydrogen mixtures in a supersonic mixing layer,” *Combust. Flame.*, vol. 102, pp. 462–470, 1995.
- [105] R. L. Gordon, A. R. Masri, S. B. Pope, and G. M. Goldin, “Transport budgets in turbulent lifted flames of methane autoigniting in a vitiated co-flow,” *Combust. Flame.*, vol. 151, pp. 495–511, 2007.
- [106] A. Krisman, E. R. Hawkes, M. Talei, A. Bhagatwala, and J. H. Chen, “Polybrachial structures in dimethyl ether edge-flames at negative temperature coefficient conditions,” *Proc. Combust. Inst.*, vol. 35, pp. 999–1006, 2015.
- [107] R. Cabra, T. Myhrvold, J. Chen, R. Dibble, A. Karpetis, and R. Barlow, “Simultaneous laser raman-rayleigh-lif measurements and numerical modeling

- results of a lifted turbulent  $\text{H}_2/\text{N}_2$  jet flame in a vitiated coflow,” *Proceedings of the Combustion Institute*, vol. 29, no. 2, pp. 1881 – 1888, 2002. [Online]. Available: <http://www.sciencedirect.com/science/article/pii/S1540748902802280>
- [108] S. Deng, P. Zhao, M. E. Mueller, and C. K. Law, “Stabilization of laminar non-premixed DME/air coflow flames at elevated temperatures and pressures,” *Combust. Flame*, vol. 162, pp. 4471–4478, 2015.
- [109] A. Krisman, E. R. Hawkes, and J. H. Chen, “The structure and propagation of laminar flames under autoignitive conditions,” *Combust. Flame.*, vol. 188, pp. 399–411, 2018.
- [110] O. Schulz and N. Noiray, “Autoignition flame dynamics in sequential combustors,” *Combust. Flame.*, vol. 192, pp. 86–100, 2018.
- [111] X. Gao, S. Yang, B. Wu, and W. Sun, “The effects of ozonolysis activated autoignition on non-premixed jet flame dynamics: a numerical and experimental study.” *53<sup>rd</sup> AIAA/SAE/ASEE Joint Propulsion Conference*, 2017.
- [112] O. Schulz, T. Jaravel, T. Poinso, B. Cuenot, and N. Noiray, “A criterion to distinguish autoignition and propagation applied to a lifted methane-air jet flame,” *Proc. Combust. Inst.*, vol. 36, pp. 1–8, 2016.
- [113] R. Sankaran, “Propagation velocity of a deflagration front in a preheated autoigniting mixture,” *9<sup>th</sup> US National Combustion Meeting*, p. paper 2E09, 2015.
- [114] C. H. Gibson, “Find structure of scalar fields mixed by turbulence. I. Zero-gradient points and minimal gradient surfaces,” *Phys. Fluids*, vol. 11, pp. 2305–2315, 1968.
- [115] T. Echekki and J. H. Chen, “Structure and propagation of methanol–air triple flames,” *Combust. Flame*, vol. 114, pp. 231–245, 1998.
- [116] H. G. Im and J. H. Chen, “Structure and propagation of triple flames in partially premixed hydrogen–air mixtures,” *Combust. Flame*, vol. 119, pp. 436–454, 1999.



- [117] H. S. Bak, S. R. Lee, J. H. Chen, and C. S. Yoo, “A numerical study of the diffusive-thermal instability of opposed nonpremixed tubular flames,” *Combust. Flame*, vol. 162, pp. 4612–4621, 2015.
- [118] S. O. Kim, M. B. Luong, J. H. Chen, and C. S. Yoo, “A dns study of the ignition of lean prf/air mixtures with temperature inhomogeneities under high pressure and intermediate temperature,” *Combustion and Flame*, vol. 162, no. 3, pp. 717 – 726, 2015. [Online]. Available: <http://www.sciencedirect.com/science/article/pii/S0010218014002685>
- [119] R. Sankaran, E. R. Hawkes, C. S. Yoo, and J. H. Chen, “Response of flame thickness and propagation speed under intense turbulence in spatially developing lean premixed methane–air jet flames,” *Combustion and Flame*, vol. 162, no. 9, pp. 3294 – 3306, 2015. [Online]. Available: <http://www.sciencedirect.com/science/article/pii/S0010218015001662>
- [120] H. S. Bak and C. S. Yoo, “Flame instabilities and flame cell dynamics in opposed nonpremixed tubular flames with radiative heat loss,” *Combust. Flame*, vol. 194, pp. 322–333, 2018.
- [121] S. Deng, P. Zhao, M. E. Mueller, and C. K. Law, “Autoignition-affected stabilization of laminar nonpremixed DME/air coflow flames,” *Combust. Flame*, vol. 162, pp. 3437–3445, 2015.
- [122] K. S. Jung, S. O. Kim, T. Lu, S. H. Chung, B. J. Lee, and C. S. Yoo, “Differential diffusion effect on the stabilization characteristics of autoignited laminar lifted methane/hydrogen jet flames in heated coflow air,” *Combustion and Flame*, vol. 198, pp. 305 – 319, 2018. [Online]. Available: <http://www.sciencedirect.com/science/article/pii/S0010218018304231>
- [123] S. Chung, “Stabilization, propagation and instability of tribrachial triple flames,” *Proceedings of the Combustion Institute*, vol. 31, no. 1, pp. 877 – 892, 2007. [Online]. Available: <http://www.sciencedirect.com/science/article/pii/S1540748906003804>

- [124] K. M. Lyons, “Toward an understanding of the stabilization mechanisms of lifted turbulent jet flames: Experiments,” *Progress in Energy and Combustion Science*, vol. 33, no. 2, pp. 211 – 231, 2007. [Online]. Available: <http://www.sciencedirect.com/science/article/pii/S0360128506000591>
- [125] C. Lawn, “Lifted flames on fuel jets in co-flowing air,” *Progress in Energy and Combustion Science*, vol. 35, no. 1, pp. 1 – 30, 2009. [Online]. Available: <http://www.sciencedirect.com/science/article/pii/S0360128508000336>
- [126] C. Markides and E. Mastorakos, “An experimental study of hydrogen autoignition in a turbulent co-flow of heated air,” *Proceedings of the Combustion Institute*, vol. 30, no. 1, pp. 883 – 891, 2005. [Online]. Available: <http://www.sciencedirect.com/science/article/pii/S0082078404000840>
- [127] R. L. Gordon, A. R. Masri, and E. Mastorakos, “Simultaneous rayleigh temperature, oh- and ch2o-lif imaging of methane jets in a vitiated coflow,” *Combustion and Flame*, vol. 155, no. 1, pp. 181 – 195, 2008. [Online]. Available: <http://www.sciencedirect.com/science/article/pii/S0010218008002058>
- [128] S. G. Kerkemeier, C. N. Markides, C. E. Frouzakis, and K. Boulouchos, “Direct numerical simulation of the autoignition of a hydrogen plume in a turbulent coflow of hot air,” *Journal of Fluid Mechanics*, vol. 720, p. 424–456, 2013.
- [129] Y. Minamoto and J. H. Chen, “Dns of a turbulent lifted dme jet flame,” *Combustion and Flame*, vol. 169, pp. 38 – 50, 2016. [Online]. Available: <http://www.sciencedirect.com/science/article/pii/S0010218016300542>
- [130] K. Kim, S. Won, and S. Chung, “Characteristics of turbulent lifted flames in coflow jets with initial temperature variation,” *Proceedings of the Combustion Institute*, vol. 31, no. 1, pp. 1591 – 1598, 2007. [Online]. Available: <http://www.sciencedirect.com/science/article/pii/S154074890600246X>
- [131] C. Xu, J.-W. Park, C. S. Yoo, J. H. Chen, and T. Lu, “Identification of premixed flame propagation modes using chemical explosive mode analysis,” *Proceedings of*

- the Combustion Institute*, vol. 37, no. 2, pp. 2407 – 2415, 2019. [Online]. Available: <http://www.sciencedirect.com/science/article/pii/S1540748918304875>
- [132] J. Li, Z. Zhao, A. Kazakov, and F. L. Dryer, “An updated comprehensive kinetic model of hydrogen combustion,” *International Journal of Chemical Kinetics*, vol. 36, no. 10, pp. 566–575, 2004. [Online]. Available: <https://onlinelibrary.wiley.com/doi/abs/10.1002/kin.20026>
- [133] M. B. Luong, Z. Luo, T. Lu, S. H. Chung, and C. S. Yoo, “Direct numerical simulations of the ignition of lean primary reference fuel/air mixtures with temperature inhomogeneities,” *Combustion and Flame*, vol. 160, no. 10, pp. 2038 – 2047, 2013. [Online]. Available: <http://www.sciencedirect.com/science/article/pii/S0010218013001569>
- [134] X. Gao, S. Yang, and W. Sun, “A global pathway selection algorithm for the reduction of detailed chemical kinetic mechanisms,” *Combustion and Flame*, vol. 167, pp. 238 – 247, 2016. [Online]. Available: <http://www.sciencedirect.com/science/article/pii/S0010218016000638>

## Acknowledgements

I would like to express my sincere gratitude to my advisor, Professor Chun Sang Yoo for his valuable guidance and patience during my doctoral study. He always encouraged me and showed a deep passion for discussion. He always advised me to be an honest researcher with patience. I also thank to my doctoral committee members- Professor Sung Youb Kim, Professor Taesung Kim, Professor Jaesung Jang and Professor Pilwon Kim, for their valuable feedback and constructive suggestions on my thesis. I am also thank to all my laboratory members. We shared valuable idea on combustion and had unforgettable memories together. Their support and encouragement have been a great help to my graduate student life. I always thank my family for believing and supporting me. Because of their dedicated support, I was able to complete the graduate program.

